The Realization & Characterization of Transmission Dynodes

Chan, H.W.

DOI
10.4233/uuid:88964974-2833-4cea-8a06-834ec7488d30

Publication date
2024

Document Version
Final published version

Citation (APA)
Chan, H. W. (2024). *The Realization & Characterization of Transmission Dynodes*. [Dissertation (TU Delft), Delft University of Technology]. https://doi.org/10.4233/uuid:88964974-2833-4cea-8a06-834ec7488d30

THE REALIZATION & CHARACTERIZATION OF TRANSMISSION DYNODES

THE REALIZATION & CHARACTERIZATION OF TRANSMISSION DYNODES

Proefschrift

ter verkrijging van de graad van doctor
aan de Technische Universiteit Delft,
op gezag van de Rector Magnificus prof. dr. ir. T. H. J. J. van der Hagen,
voorzitter van het College voor Promoties,
in het openbaar te verdedigen op
woensdag 25 september 2024 om 12:30

door

Hong Wah CHAN

Master of Science in Applied Physics,
Technische Universiteit Delft, Delft, Nederland,
geboren te Utrecht, Nederland.

Dit proefschrift is goedgekeurd door de promotoren:

Prof. dr. ir. H. van der Graaf
Prof. dr. ir. P.M. Sarro
Dr. C.W. Hagen

Samenstelling promotiecommissie:

Rector Magnificus,	voorzitter
Prof. dr. ir. H. van der Graaf	Technische Universiteit Delft, promotor
Prof. dr. ir. P.M. Sarro	Technische Universiteit Delft, promotor
Dr. C.W. Hagen	Technische Universiteit Delft, promotor
Onafhankelijke leden:	
Prof. dr. B. Rieger,	Technische Universiteit Delft
Prof. dr. T.A. du Pree,	Universiteit Twente
Prof. dr. K. Desch,	Universität Bonn, Duitsland
Ir. G. Nutzel,	Exosens/Photonis, Nederland
Prof. dr. P.J. French,	Technische Universiteit Delft, reservelid

Keywords: Secondary electron emission, single photon detector, transmission dynodes, atomic layer deposition, microfabrication
Printed by: Ipskamp printing
Front & Back: A.A. van Rooij

ISBN 978-94-6473-584-0

An electronic version of this dissertation is available at
http://repository.tudelft.nl/.

Pain is inevitable. Suffering is optional.
Say you're running and you think,
'Man, this hurts, I can't take it anymore.
The 'hurt' part is an unavoidable reality,
but whether or not you can stand anymore
is up to the runner himself

Haruki Murakami

CONTENTS

ACRONYMS

AC	alternating current
ALD	Atomic Layer Deposition
APD	Avalanche PhotoDiode
BSE	backscattered electron
BSEY	backscattered electron yield
CMOS	Complementary metal-oxide semiconductor
CPT	Charges Particle Tracing
CW	Cockcroft-Walton
DC	direct current
DFT	Density Functional Theory
DRIE	Deep-Reactive Ion Etching
EA	electron affinity
EBIC	electron-beam induced current
FSE	forward-scattered electron
FSEY	forward-scattered electron yield
HV	High Voltage
LAPPD	Large Area Picosecond PhotoDetector
LPCVD	low-pressure chemical vapor deposition
MCP	Micro-Channel Plate
MCP-PMT	Micro-Channel Plate PhotoMultiplier Tube
MEMS	Micro-ElectroMechanical System
MIP	minimum ionizing particle
NEA	negative electron affinity
PDE	photon detection efficiency
PE	primary electron
PECVD	plasma-enhanced chemical vapor deposition
PET	Positron Emission Tomography
PMT	PhotoMultiplier Tube
PR	photoresist
QE	quantum efficiency
REY	(total) reflection electron yield
RSE	reflection secondary electron
RSEY	reflection secondary electron yield
S/N	signal-to-noise ratio
SE	secondary electron
SEE	secondary electron emission
SEM	scanning electron microscope

SEY	secondary electron yield
SiPM	Silicon Photomultiplier
SOI	silicon-on-oxide
SPAD	Single Photon Avalanche Diode
SPTR	single-photon time resolution
TEY	(total) transmission electron yield
TiPC	Timed Photon Counter
TOF-PET	Time-of-flight Positron Emission Tomography
TSE	transmission secondary electron
TSEY	transmission secondary electron yield
TTS	transit time spread
tynode	transmission dynode
Tytest	tynode test setup
UHV	ultra-high vacuum
UNCD	ultra-nanocrystalline diamond
UV	ultraviolet
WITS$	Wavelength, Intensity, Temporal behavior, Spatial distribution and Costs
XPS	X-ray photoelectron spectroscopy

List of Symbols

A	escape probability
α	correction term for measurement setup
C	material-dependent constant in range-energy relations
c	speed of light
χ	electron affinity
D	diameter of cell
d	(total effective) film thickness
d/R	reduced film thickness
d_1	film thickness of film 1 with material 1
d_1^{eff}	effective film thickness of film 2
dE/dx	energy transfer profile
δ_b	contribution of backward moving (primary) electrons
δ_p	contribution of forward moving primary electrons
δ_R	reflection secondary electron yield/coefficient
δ_T	transmission secondary electron yield/coefficient
$\delta_T/\delta_T^{\max}$	reduced transmission secondary electron yield
$\delta_T^{\max}$	maximum transmission secondary electron yield/coefficient
ΔV	potential difference
$\varnothing$	diameter of a membrane
E	energy
$E_0/E_0^{\max}$	reduced energy
$E_0^{\max}$	PE energy for maximum transmission secondary electron yield
E_0	primary electron energy
E_c	critical energy
E_{se}	secondary electron energy
E_{th}	threshold energy
E_x	primary electron energy at depth x
EF	enhancement factor
ϵ_0	permittivity in vacuum
ϵ_r	dielectric constant
ε_θ	backscattered angle efficiency
$E_R^{\max}$	required PE energy for maximum (total) reflection electron yield
η_R	back-scattered electron yield/coeffcient
η_T	transmitted fraction or forward-scattered electron yield/coeffcient
$E_T^{\max}$	PE energy for maximum (total) transmission electron yield
F_e	electric field
G	gain

γ	opacity (of a grid mesh)
h	Planck's constant
I_0	primary beam current
I_C	collector current
I_{RG}	retarding grid current
I_S	sample current
k	number of membranes
l	distance
λ	wavelength
m	number of multiplication stages
n	constant that depends on the primary electron energy-range
p	transmission parameter
p_{EA}	material-dependent constant (for electron affinity calculation)
q	charge
R	range
ρ	density
σ	total electron yield
σ_R	transmission electron yield/coefficient
$\sigma_R^{\max}$	maximum reflection electron yield/coefficient
σ_T	reflection electron yield/coefficient
$\sigma_T^{\max}$	maximum transmission electron yield/coefficient
U	bias voltage
w	width of rib
x	position or depth
Z	atomic number

CHEMICAL ELEMENTS & COMPOUNDS

Al	aluminum
Al_2O_3	alumina/aluminum oxide
Au	gold
Cr	chromium
Cs	cesium
CsI	cesium iodide
GaAs	gallium arsenide
H	hydrogen
HF	hydrofluoric
KCl	potassium chloride
KOH	potassium hydroxide
LiF	lithium fluoride
MgO	magnesium oxide
NaF	sodium fluoride
Si	silicon
SiN	silicon nitride
SiO2	silicon dioxide
$TiCl_4$	titanium chloride
TiN	titanium nitride
TMA	trimethyl-aluminum

SUMMARY

THE Timed Photon Counter (TiPC) is a novel vacuum electron multiplier that is based on the operating principles of a PhotoMultiplier Tube (PMT), but outperforms it in terms of time and spatial resolution. The core innovation is the transmission dynode (tynode), which emits secondary electrons (SEs) in reflection as well as in transmission. This distinctive property allows tynodes to be closely stacked on top of each other, which results in a compact planar photodetector. The shorter and more uniform electron paths result in a better timing performance compared to PMTs. In addition, spatial information is gained by using a TimePix chip as read-out. A requirement for the tynodes in TiPC is to achieve a (total) transmission electron yield (TEY) of 4 or higher for sub-1-keV primary electrons (PEs).

The goal of this work is to characterize the secondary electron emission (SEE) properties of tynodes that are fabricated using Micro-ElectroMechanical System (MEMS)-based) techniques. The thinness of the membranes, which is in the order of tens of nm, poses challenges in both the fabrication as well as in the characterization of the tynodes. For the latter, a new method has been developed to measure the SEE properties of tynodes within a scanning electron microscope using a (hemispherical) collector assembly mounted to the moving stage. This method allows the tynodes to be inspected before a TEY measurement, so that the electron beam only targets the active surface of the tynode. For the former, different tynode designs have been used to construct mechanically strong, but ultra-thin membranes. In this work, three different types are presented: single-membrane, square-array and corrugated membrane.

The first type is a single-membrane tynode, which is designed to determine the effect of film thickness on the transmission SEE. A tynode is in essence an ultra-thin membrane that consists of a SEE layer and a conductive layer. In this case, Atomic Layer Deposition (ALD) aluminum oxide (Al_2O_3) is the SEE material and titanium nitride (TiN) is the conductive material. Two types of membranes have been fabricated: a bi-layered and a tri-layered. The former consists of an Al_2O_3 membrane on which TiN was sputtered at the end of the fabrication process, while for the latter, the TiN was sputtered in an earlier stage in the fabrication process. By encapsulating the conductive layer, the reliability of the fabrication process improved.

The TEY curves as a function of the PE energy of these membranes have been measured for 0.3 to 10 keV for three different thicknesses. The Al_2O_3/TiN/Al_2O_3 membrane with layer thicknesses of 5/2.5/5 nm, respectively, has the highest maximum TEY of 3.1, which is obtained with PEs with an energy of 1.55 keV. For increasing film thickness, the onset of transmission SEE occurs at higher PE energy and the maximum TEY is lower. The role of film thickness on the SEE properties has been further investigated by separating the fast and slow electrons.

The second type is an ALD TiN/magnesium oxide (MgO) square-array tynode, which is designed to be compatible with a TimePix chip. The tynode consists of ultra-thin circu-

lar membranes within a supporting frame. The pixelated design ensures that the ultra-thin membranes can be released reliably during fabrication. They have a diameter of 30 µm and are arranged in a 64 × 64 array with a square pitch of 55 µm, which matches the pixel pad pitch on a TimePix chip.

The transmission electron emission of these TiN/MgO tynodes have been investigated with a planar collector assembly within a scanning electron microscope (SEM). The collector assembly is modified to investigate the effect of a strong electric field near the emission surface of a tynode. The electric field strength is in the same order of magnitude as in TiPC. A surface scan method has been used to determine the TEY of individual membranes in the array; the TEY map corresponds with the SEM image. PEs with energies of 0.75 to 5 keV were used. The averaged maximum TEY for a TiN/MgO tynode with layer thicknesses 2/5 nm is 4.6 ± 0.2, which is obtained with PEs with an energy of 1.35 keV. The averaged maximum TEY improves from 4.6 ± 0.2 to 5.0 ± 0.3 when the bias voltage increases from −50 V to −100 V. However, the effect levels off when the bias voltage is further increased.

The third type is a corrugated membrane tynode, which is designed to have a larger active surface. These large-area tynodes are fabricated by depositing an ultra-thin continuous film on a silicon wafer with a 3-dimensional pattern. After removing the silicon, a corrugated membrane with enhanced mechanical properties is formed. The ultra-thin film consists of Al_2O_3/TiN/Al_2O_3 deposited by ALD. A corrugated membrane can span a larger surface area in comparison with a flat membrane, while retaining an active surface close to 100%. In addition, the octagonal cups have a focusing effect, which can be used to direct transmission secondary electrons (TSEs) onto the pixel pads of a TimePix chip. Both improve the collection efficiency of TiPC, since reabsorption of TSEs within the tynodes stack will be less likely.

The TEYs of these corrugated metamaterial membranes are measured within a SEM using the hemispherical collector assembly for PEs with energies ranging from 0.3 to 10 keV. The surface scan method is used to construct a yield map, which shows that transmission electron multiplication occurs on the entire surface regardless of the features on the corrugated membrane. The TEY does vary, but remains larger than 1. An average maximum yield of 2.15 has been measured by using PEs with an energy of 3.15 keV. This is slightly lower compared to the flat single-membrane with a similar thickness.

This work shows that the film thickness determines the transmission SEE properties of an ultra-thin membrane. TiN/MgO membranes with a thickness of 2.5/5 nm fulfill the requirements for tynodes that will be used in TiPC detectors. The square-array tynodes can be reliably fabricated due to its pixelated design with the small circular membranes, which are compatible with a TimePix chip. If a larger membrane is preferred, then the surface area can be enlarged by two orders of magnitude by using a corrugated membrane.

SAMENVATTING

De Timed Photon Counter (de getimede fotonenteller of TiPC), is een nieuwe vacuümbuis fotomultiplicator die is gebaseerd op de werking van een fotoversterkerbuis, maar met verbeterde tijds- en beeldresolutie. De kern van de innovatie zijn de transmissie (doorlatende) dynodes, of in het kort tynodes, die secundaire elektronen uitzenden in zowel reflectie als in transmissie. Deze unieke eigenschap staat toe dat tynodes dicht op elkaar gestapeld kunnen worden, wat resulteert in een compacte, platte fotonendetector. De kortere en homogenere banen die de elektronen afleggen resulteert in een betere timing prestatie in vergelijking met de fotobuisversterker. Daarnaast wordt er planaire plaatsresolutie verkregen wanneer een TimePix chip als uitleeschip wordt gebruikt. Een vereiste voor de tynodes in TiPC is om een opbrengst aan transmissie elektronen (transmission electron yield of TEY) van 4 of meer te behalen met primaire elektronen met energieën lager dan 1 keV.

Het doel van dit werk is om de secundaire elektronenemissie (SEE) eigenschappen van tynodes te onderzoeken die gefabriceerd zijn met behulp van fabricatietechnieken die veelvuldig gebruikt worden voor Micro-elektromechanische systemen (MEMS). De dunte van de membranen, welk slechts enkele nanometers bedraagt, zorgt voor uitdagingen in zowel het fabricageproces als ook in het karakteriseren/onderzoeken van de tynodes. De aanpak voor het laatste is de ontwikkeling van een nieuwe methode om de secundaire elektronenemissie van tynodes te meten in een elektronenmicroscoop met behulp van een half-bolvormige collector-setup die gemonteerd is op het bewegende platform van de microscoop. Deze methode staat toe dat de tynodes geïnspecteerd worden voordat de transmissie elektronen opbrengst gemeten wordt, zodat ervoor gezorgd kan worden dat de elektronenbundel enkel de actieve oppervlakte bestraalt. Voor de eerste uitdaging zijn er verschillende tynodes ontworpen die mechanisch sterk en ultradun zijn. In dit werk worden drie verschillende types gepresenteerd: een 'enkel-membraan', een 'vierkant-rooster' en een 'gegolfd membraan'.

Het eerste type is een enkel membraan tynode, ontworpen om het effect van de filmdikte op de transmissie secundaire elektronenemissie te bepalen. Een tynode is in essentie een ultradun membraan dat bestaat uit een secundaire elektronenemissie laag en een geleidende laag. In dit geval is Atomic Layer Deposition (ALD) Al_2O_3 het SEE materiaal en TiN het geleidende materiaal. Twee soorten membranen zijn er gefabriceerd: twee-laags en drie-laags. Het eerste bestaat uit een Al_2O_3 membraan waarop TiN is gesputterd aan het eind van het fabricatieproces, terwijl voor het tweede, de TiN in een eerder stadium is gesputterd. Door de geleidende laag in te kapselen is de betrouwbaarheid van het fabricatieproces verbeterd.

De TEY-curve, als functie van de primaire elektronen energie, is gemeten voor 0.3 tot 10 keV voor drie verschillende filmdiktes. Het $Al_2O_3/TiN/Al_2O_3$ membraan met laagdiktes van 5/2.5/5 nm, respectievelijk, heeft de hoogste maximale opbrengst van 3.1, behaald met primaire elektronen energie van 1.55 keV. Voor toenemende dikte verschuift

het punt waarop transmission SEE meetbaar is naar een hogere PE-energie en neemt de maximale transmissie elektronen opbrengst af. De rol van de filmdikte op de SEE eigenschappen is verder onderzocht door de snelle en langzame elektronen te scheiden.

Het tweede type is een ALD TiN/MgO vierkant-rooster tynode, die zo is ontworpen dat het gecombineerd kan worden met een TimePix chip. De tynode bestaat uit ultradunne, circulaire membranen in een dragend frame. Het gepixeleerde ontwerp zorgt ervoor dat de ultradunne membranen op een betrouwbare manier losgemaakt kunnen worden tijdens fabricatie. Zij hebben een diameter van 30 µm en zijn geordend in een 64×64 grid met een afstand van 55 µm ten opzichte van elkaar, overeenkomend met de afstanden tussen de pixels op een TimePix chip.

De transmissie elektronenemissie van deze TiN/MgO tynodes is onderzocht met behulp van een vlakke collector-setup die gemonteerd is in een elektronenmicroscoop. Er is hier voor een andere elektrode-combinatie gekozen om het effect van een sterk elektrisch veld dicht op de emissie oppervlakte van de tynode te onderzoeken. De elektrische veldsterkte is in dezelfde orde van grootte als het veld aanwezig in TiPC. Een oppervlaktescan methode is gebruikt om de transmissie elektronen opbrengst te bepalen van individuele membranen in het rooster. De TEY kaart correspondeert met de elektronenmicroscoopafbeelding. Primaire elektronen met energieën van 0.75 tot 5 keV zijn hiervoor gebruikt. De gemiddelde maximale TEY voor een TiN/MgO tynode met laagdiktes van 2/5 nm is 4.6 ± 0.2, die behaald is met primaire elektronen met een energie van 1.35 keV. De gemiddelde maximale TEY verbeterde van 4.6 ± 0.2 naar 5.0 ± 0.3 wanneer het potentiaalverschil vergroot werd van -50 V naar -100 V. Het effect vlakt echter af als het potentiaalverschil toeneemt.

Het derde type is een gegolfd membraan tynode die ontworpen is voor een groter actief oppervlak. Deze tynodes zijn gefabriceerd door een ultradunne, continue film aan te brengen op een silicium wafer met een 3-dimensionaal patroon. Na het verwijderen van al het silicium blijft er een gegolfd membraan met versterkte mechanische eigenschappen over. De ultradunne film bestaat uit Al_2O_3/TiN/Al_2O_3, aangebracht met ALD. Een gegolfd membraan kan over een groter oppervlak gespannen worden in vergelijking met een vlak membraan, terwijl het een actief oppervlak van bijna 100% behoudt. Bovendien hebben de achthoekige holtes een focusserende werking, die gebruikt kan worden om de transmissie secundaire elektronen naar de pixels van de TimePix chip te dirigeren. Beide bevorderen de collectie efficiëntie van TiPC, omdat reabsorptie van transmissie secundaire elektronen binnen in de tynodestapel minder vaak zal voorkomen.

De TEY van deze gegolfde metamateriaal membranen is gemeten in een elektronenmicroscoop met behulp van de half-bolvormige collector-setup voor primaire elektronen met een energie die varieert van 0.3 tot 10 keV. De oppervlakte-scan methode is gebruikt om een TEY kaart te reconstrueren, waarop te zien is dat er transmissie elektronenemissie plaats vindt op het gehele oppervlak ongeacht de kenmerkende vormen van het gegolfde membraan. De TEY varieert wel over het oppervlak, maar blijft groter dan 1. Een gemiddelde maximale TEY van 2.15 is gemeten voor primaire elektronen met een energie van 3.15 keV. Dit is iets lager in vergelijking met een vlak enkel-membraan tynode met dezelfde dikte.

Dit werk laat zien dat de filmdikte de transmissie secundaire elektronenemissie eigenschappen van een ultradun membraan bepaalt. TiN/MgO membranen met een dikte

van 2.5/5 nm voldoen aan de vereisten voor tynodes die gebruikt gaan worden in TiPC detectoren. De vierkante grid tynodes kunnen op een betrouwbare manier gefabriceerd worden dankzij het gepixeleerde ontwerp met kleine circulaire membranen, dat ook compatibel is met een TimePix chip. Als een groter membraan nodig is, dan kan het oppervlak twee orden van grootte vergroot worden door gebruik te maken van een gegolfd membraan.

1

INTRODUCTION

1.1. DETECTION OF LIGHT

VISION is one of the five senses that allow humans to perceive the world. The human eye has evolved into a sophisticated camera through millions of years of natural selection and was paramount in the survival of our species [1]. Light, reflected from an object, enters our eyes through the cornea and is projected onto the retina by a crystalline lens (figure 1.1). The retina consists of cones and rods, which generate electrical signals when photons are absorbed. The signal travels via optic nerves to the brain, which processes, interprets and reconstructs the observed object. The rods are very sensitive in low light environment, but can only provide a low resolution black and white image. The cones are sensitive to either red, blue or green and provide a higher resolution image, although only in well-lit surroundings. The human eyes are sensitive to photons with wavelengths of 350 to 760 nm, which is defined as the visible spectrum. Our brains interpret photons with different wavelengths as different colors. This versatility allowed humans to forage and hunt during the day and avoid predators at dusk and in the middle of the night.

While the human eye is a remarkable photon detector, the visible spectrum is only a tiny fraction of the electromagnetic spectrum. In nature and in natural phenomena, different types of radiation are involved that are invisible to the human eye. Outside the visible spectrum, there are infrared, microwave and radio wave on one end, and ultraviolet, x-ray and gamma radiation on the other. Photons are characterized by their wavelengths and/or energy E that they carry: $E = \frac{hc}{\lambda}$, where λ is the wavelength, h is Planck's Constant and c is the velocity of light. The discovery of these types of radiation has led to the invention of photon detectors tailored to specific parts of the electromagnetic spectrum [2]. This advanced the progress of, among others, medical imaging and particle physics.

In medical imaging, x-rays are used to image the body [3]. The attenuation of x-rays depends on the density of the body tissue. As such, bone tissue can be differentiated from muscles and internal organs. A more advanced technique, computed tomography,

1

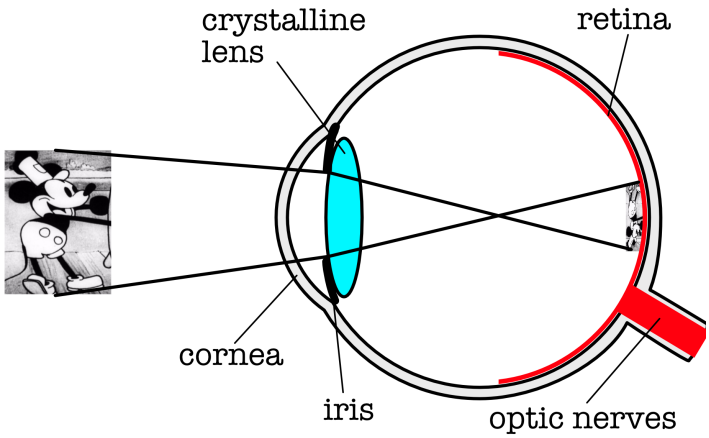

Figure 1.1: The human eye. Light, reflected from an object, enters the eye through the cornea. The amount of light that enters is regulated by the iris, which can change its size to prevent over-saturation. The crystalline lens inside the eye projects the light onto the retina at the back of the eyeball. When photons are absorbed by the cones and rods, an electrical signal is generated and sent to the brain via optic nerves. The brain processes and reconstructs an image of the object.

uses the same principle to reconstruct a 3D image of the body by rotating the source and detector around the patient. In Positron Emission Tomography (PET) scanners, a radioactive isotope is injected in a patient [4]. Fluorine-18 decays into Oxygen-18 by positron emission. The positron will annihilate when it collides with an electron, which will yield two 511-keV gamma photons that are emitted at approximately 180 degrees. When the detector ring surrounding the patient detects both gamma photons, the point of origin of the event can be reconstructed. The better the time resolution of the detector is, the more accurate the point of origin can be determined.

In particle physics, charged particles are accelerated to very high energies and collide in an interaction point. Around this point, detectors are placed, recording position and timing of tracks of particles, created in the collision [5]. There is a trend towards a very high density of tracks, and pattern recognition requires an unprecedented time resolution of the tracking detectors. Charged particles, created in the interaction point, can emit multiple soft Cherenkov photons when passing through a thin Cherenkov radiator, enabling determination of the track passage with excellent time resolution. Another example of a detector that employs Cherenkov radiation are neutrino-detectors [6]. Neutrinos that are emitted from the sun or nuclear reactors will usually pass through the earth without interactions. However, in a large body of (heavy) water, there is a chance that a neutrino will interact and a high energetic lepton will be emitted. The speed of the lepton exceeds the speed of light and will emit Cherenkov radiation to slow down. The weak flash of Cherenkov light is detected by an array of PhotoMultiplier Tube (PMT) surrounding the body of water.

In these applications, a special class of photon detectors is used: *single-photon detectors* [7]. The detectors can detect extremely weak light signals down to single photons. Depending on the application, the detector can be attuned to be sensitive to photons

in a specific part of the ultraviolet (UV), visible and/or infrared spectrum. These photons are referred to as soft photons to distinguish them from the high-energetic x-ray or gamma ray photons. The latter is detected by using a scintillation crystal, which absorbs the high-energetic photon and in the process scintillates soft photons [8]. For instance, the detector in a PET scanner consists of a scintillation crystal and a PMT. When a 511-keV photon is absorbed in the crystal, $\sim 10^4$ soft photons are emitted of which ~ 40 are prompt Cherenkov photons, arriving first in a detector, carrying the best possible timing information.

1.2. SINGLE-PHOTON DETECTORS

THERE are a wide variation of photodetectors that are commercially available: photodiodes, Silicon Photomultiplier (SiPM) with Avalanche PhotoDiodes (APDs) or Single Photon Avalanche Diodes (SPADs) and vacuum electron multipliers, such as Micro-Channel Plate PhotoMultiplier Tubes (MCP-PMTs) and PMTs. Photodetector manufacturers recommend using the 'WITS$' approach for selecting the appropriate photodetector for applications [9]. It stands for Wavelength, Intensity, Temporal behavior, Spatial distribution and Costs. The first selection criteria involves the spectral responsivity and the quantum efficiency (QE) or photon detection efficiency (PDE) of the detector. The second criteria involves the incident light power that is expected in the application, both in minimum detectable power of the detector as well as its upper limit. Here the selection criteria is the best signal-to-noise ratio (S/N) possible for the given light input. The third criteria is the temporal characteristics of incident light, whether it is a DC, AC or pulsed light input. The fourth is the spatial characteristics of incident light. If light is collimated, then an optical system can help to increase the incident light power and improve the S/N. Lastly, the cost of the system can be the tie-breaker.

In this work, the scope is limited to single-photon detection. The intensity of light in applications in particle physics and in medical imaging is often low or involves single photons [7]. PMTs used to be the go-to detector for many applications. However, SiPMs have become an alternative due to recent developments, which improved their performance to be comparable to PMTs or even exceed them. PMTs and SiPMs are the preferred detectors due to their S/N. However, for modern applications, such as Time-of-flight Positron Emission Tomography (TOF-PET) , the time resolution of PMTs is insufficient and SiPMs are likely to replace them [8]. Another alternative is the MCP-PMT, which also has a better time resolution.The operating principles of these three detectors will be discussed here and their strength and weaknesses will be compared. In section 1.3, a novel vacuum electron multiplier will be proposed that is based on PMTs, but outperforms them in terms of time and spatial resolution.

1.2.1. PHOTOMULTIPLIER TUBES

The detection principle of a PMT is the conversion of photons into photoelectrons by the photoelectric effect and subsequent secondary electron (SE) multiplication in vacuum [10]. A PMT consists of a photocathode, guiding electrodes, dynodes and an anode, which are encapsulated within a glass enclosure as shown in figure 1.2. For high-energetic photons, such as x-ray and/or gamma-ray photons, a scintillation crystal can

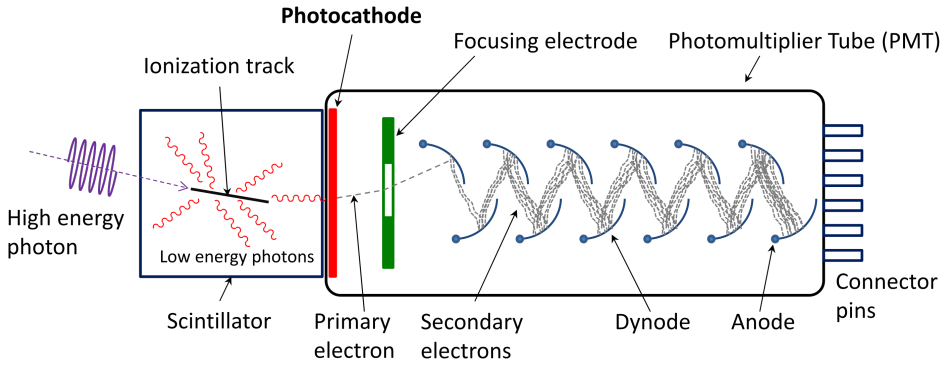

Figure 1.2: A schematic drawing of a PMT [11]. A high energetic photon enters a scintillation crystal and generates soft photons along its track. Some of the photons will be converted into photoelectrons at the photocathode. The photoelectrons are focused and accelerated towards the first dynode. Upon impact, the photoelectrons will generate multiple RSEs from the dynode. The generated RSEs are then directed towards the next dynode. This process repeats and the number of RSEs increases after each dynode. Eventually, the avalanche of electrons is collected by the anode and an analog signal is registered.

be placed in front of a PMT. When a high-energetic photon is absorbed by the crystal, a small flash of light is scintillated. These soft photons enter the PMT through a window and are converted into photoelectrons at the photocathode. The photoelectrons are accelerated and directed towards the first dynode by the guiding electrodes. When the photoelectrons strike the surface of the dynode, multiple reflection secondary electrons (RSEs) are emitted on the same side of the dynode, which are accelerated towards the next dynode. The dynodes are arranged in an intricate manner and the electric potential is step-wisely increased between them, so that the RSEs are directed from dynode to dynode in a cascading order. After m dynodes, an avalanche of RSEs are collected by the anode. The reflection secondary electron yield δ_R is the ratio of RSEs and primary electrons (PEs). The gain G of a PMT is given by $G = \delta_R^m$.

The advantages of PMTs are the wide spectral sensitivity, large sensing area, large gain and low noise. The spectral sensitivity of a PMT depends on the photocathode material, which can be tailored to the application. The sensing area of a PMT can be relatively large and is determined by the shape of the glass bulb on which the photocathode material is evaporated. The photoelectrons are directed towards the dynode stack by the guide electrodes. The disadvantages of a PMT are its time resolution, susceptibility to external electric and magnetic fields, fragility and cost. The dynodes require an intricate reflective geometry for secondary electron multiplication. As a consequence, the electron paths of the PEs and RSEs within the dynode stacks are non-uniform, which lead to a large transit time spread (TTS) or time resolution in the order of a few nanoseconds. In addition, the PEs and RSEs in transit can be disturbed by external fields. PMTs are also relatively large and difficult to fabricate leading to high costs.

1.2.2. MICRO-CHANNEL PLATE

A MCP-PMT has a similar working principle as a PMT, namely photo emission and subsequent secondary electron multiplication in vacuum [12]. A MCP-PMT consists of a photocathode, one or multiple Micro-Channel Plates (MCPs) with slanted micro channels, and an anode or a readout chip, which are enclosed in a planar vacuum package (figure 1.3). A soft photon is converted into a photoelectron at the photocathode. The photoelectron is accelerated towards the micro channels and will impact on the surface of the plate or inside a channel. In the process, multiple RSEs are generated that will enter the channels due to the electric field between the top and bottom of the substrate. The RSEs will travel through the channel and strike the walls of the channels multiple times. Each time this occurs, the number of RSEs increases. The RSEs are collected by either a single anode or by individual pixel pads of a pixel chip.

The advantage of a MCP-PMT is the improvement in time resolution; the electron paths of the newly generated RSEs are much shorter and more regular in comparison, which lead to a smaller TTS. MCP-PMTs have a time resolution of $< 100\,\text{ps}$ [12]. In addition, when a pixelated read-out chip is used, 2D-spatial information is gained, which allows MCPs to track the origin of photoelectrons [13]. The spatial resolution is limited by the channel dimensions and spacings, and/or the pixel spacing on the read-out chip. The disadvantage of a MCP-PMT is the smaller gain in comparison with a PMT, which is $\sim 10^4$ for a MCP-PMT with a single plate. The gain can be improved to $\sim 10^7$ by placing a second plate in a Chevron configuration. However, this will worsen the time resolution, which is a trade-off that needs to be considered.

1.2.3. SILICON PHOTOMULTIPLIERS

SiPMs are based on Avalanche PhotoDiodes (APDs) and/or Single Photon Avalanche Diodes (SPADs) [7, 8]. The operating principle is the creation of electron-hole pairs after the absorption of a photon in a p-n junction (figure 1.4). By applying a reverse bias voltage, the electrons and holes migrate and establish a current. In APD mode, there is a current gain of up to 1000 due to impact ionization within the p-n junction. When operated in SPAD or Geiger mode, the voltage is set above the breakdown voltage of the junction. A self-sustaining avalanche occurs after the creation of a single electron-hole pair by absorbing a photon. After detection of a photon, the SPAD is quenched by lowering the voltage across the junction below the breakdown voltage using a quenching circuit. The time to reset the SPAD is known as the reset time or dead time in which it cannot detect a photon. A SiPM often consists of multiple SPADs, which are arranged in an array allowing SiPMs to be used as a tracking detector.

The advantages of SiPMs are their high gain, quantum efficiency, immunity to external electric and magnetic fields, robustness and compactness. The disadvantages of SiPMs are their dead time, dark count, crosstalk and non-linearity for higher intensities. Also, the sensing area is determined by the pixel and array size. In addition, its spectral responsivity is limited in comparison with photocathodes.

1.2.4. ULTRA-FAST PHOTODETECTORS

In applications with extremely low light levels or that involves single photons, the WITS$ approach would recommend either PMTs or SiPMs due to the low light Intensity. How-

1

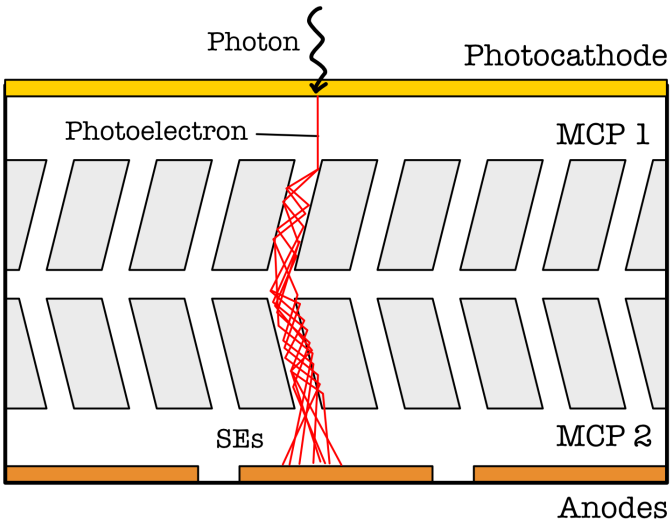

Figure 1.3: A schematic drawing of a MCP Chevron stack. A soft photon is converted into a photoelectron at the photocathode. The photoelectron enters the slanted micro-channels of the first MCP. When an electron strikes the surface of the channel, multiple RSEs are generated. The RSEs will strike the channel wall a few times and generate more RSEs in the process. At some point, they will leave the first plate and enter the channels of the second plate repeating the process. Eventually, an avalanche of RSEs is collected by an anode.

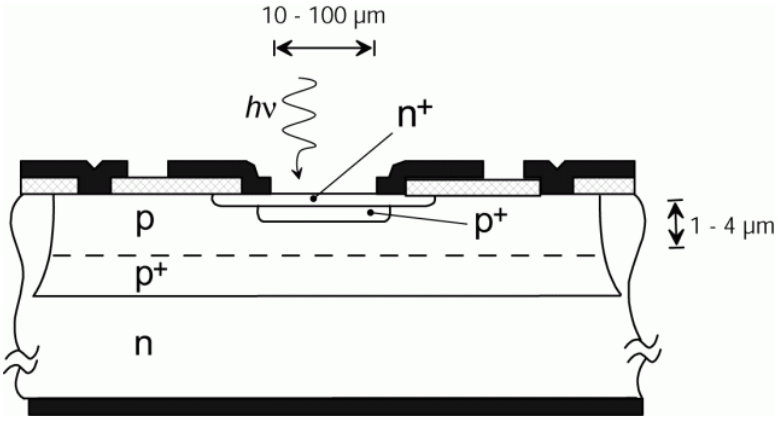

Figure 1.4: A schematic drawing of a SPAD [14]. A photon that enters a p-n junction can generate electron-hole pairs, which will induce a self-sustaining avalanche in Geiger mode. The SPAD needs to be quenched after an avalanche before it is operable again.

ever, modern applications require ultra fast time resolution in the < 100 ps range. The temporal characteristics are one of the key focus point in photodetector development [8, 13]. Ultra-fast photodetectors will benefit applications in medical imaging and high energy particle physics. For instance in medical imaging, the spatial resolution of a TOF-PET scanner depends on the time resolution of its photodetector [8]. When a positron annihilates with an electron, two 511-keV electrons are emitted in opposite direction at approximately 180 degrees in a nearly straight line. By measuring the difference in arrival time of the two photons, the point of origin on the line can be deduced. The smaller the time resolution, the better the spatial resolution will become.

The time resolution of PMTs is defined as the transit time spread (TTS), which is in the order of 0.4 ns to less than 10 ns depending on the dynode type [10]. It is insufficient for applications that require ultra-fast timing. MCP-PMTs perform better in this regard as a TTS of 25 ps was reported [10]. A photodetector that is based on MCP-PMTs is the Large Area Picosecond PhotoDetector (LAPPD) [13]. The LAPPD has a large active surface of about 400 cm^2 and has 8×8 square pads of 1 inch size as readout. The LAPPD was characterized in a test beam exercise at CERN PS testbeam. A time resolution of about 80 ps was reported for single photoelectrons.

The time resolution for SiPMs is expressed as the single-photon time resolution (SPTR). A review paper on the applicability of SiPMs in TOF-PET has shown that a SPTR of 20 – 50 ps is commonly achieved by state-of-the-art SiPMs [8].The PDE of SiPMs are excellent and outperform that of photocathodes. Photocathodes have QEs in the range of 25% – 40%, whereas SiPMs can have a PDE of up to about 60% at 420 nm. However, the disadvantages of SiPMs as listed in subsection 1.2.3 need to be considered when implementing them in TOF-PET scanners.

In the next section, a novel electron multiplier is proposed, which is based on PMTs, but will outperform it in terms of time and spatial resolution.

1.3. THE TIMED PHOTON COUNTER

THE main objective of the MEMBrane project is to develop a novel electron multiplier based on the operating principles of PMTs, i.e. photoemission from a photocathode and subsequent secondary electron multiplication in vacuum, but improved upon in terms of time resolution [15]. First, the working principle of this novel photodetector will be explained, then an overview of the key challenges in its development are given in subsection 1.3.2.

1.3.1. THE WORKING PRINCIPLE

The Timed Photon Counter (TiPC) consists of a photocathode for photoemission, a transmission dynode (tynode) stack for electron multiplication and a Complementary metal-oxide semiconductor (CMOS) pixel chip as readout, which are assembled within a vacuum enclosure (figure 2.1). The core innovation of TiPC is the use of a stack of tynode for electron multiplication. Tynodes are ultra-thin membranes where an impinging PE on the front side will generate multiple transmission secondary electrons (TSEs) on the back side. This distinctive property allows tynodes to be closely stacked on top of each other. The electric fields between the multiplication stages are stronger and more homo-

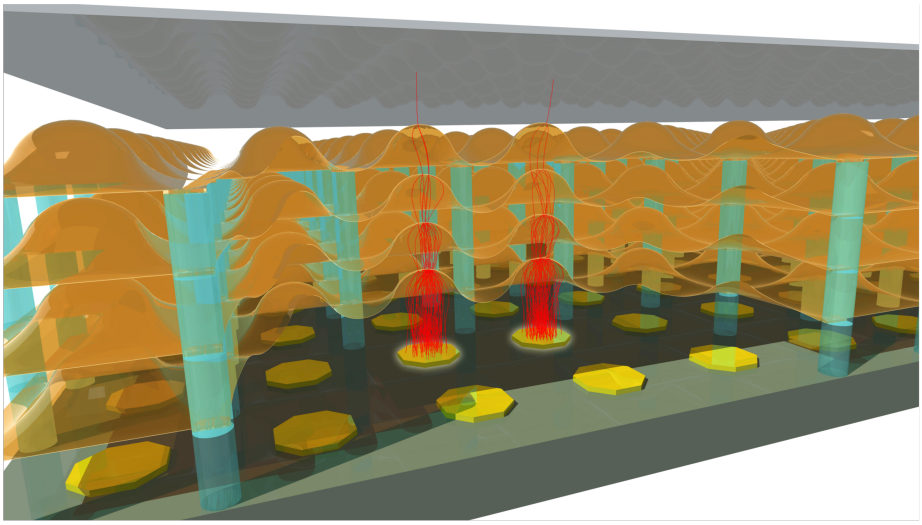

Figure 1.5: The Timed Photon Counter is a novel vacuum electron multiplier that consists of a photocathode, a tynode stack and a TimePix chip in an enclosed vacuum package [15]. The ultra-thin membranes are suspended in a supporting mesh and are spaced to align with the pixel pads of a TimePix chip. A photon that hits the photocathode is converted to a photoelectron. The photocathode is at a negative potential with respect to the first tynode. As a consequence, the photoelectron accelerates towards the first tynode and gains energy equal to $E = q\Delta V$, where q is the charge of the electron and ΔV the potential difference. When the photoelectron impacts the top of the first tynode, multiple SEs are emitted from the bottom. Subsequently, the SEs are accelerated and gain energy before they impact the next tynode. The process repeats until the avalanche of electrons is collected by the pixel pad of the TimePix chip. For a stack with m tynodes, the gain is $G = \sigma_T^m$, where σ_T is the transmission electron yield per tynode.

geneous in comparison to the electric fields in reflective geometries used in PMTs. The electron transit time of the SEs will only be tens of picoseconds with a small spread. The electron TTS is also known as the time jitter or the time resolution of the detector. Additionally, the susceptibility to external magnetic fields is reduced due to the increased electric field strength and compact size, which allows TiPC to be operated in applications where external magnetic fields are present. By combining the tynode stack with a CMOS pixel chip (TimePix), 2D spatial information can be obtained. TiPC is an ultrafast, pixelated, planar photon detector.

Transmission dynodes are in essence ultra-thin films/membranes that consist of 1) a high secondary electron emission (SEE) material and 2) an additional conductive layer (if the SEE layer lacks intrinsic conductivity). In general, the majority of high SEE materials are dielectrics. To sustain an extended period of SEE, in-plane conductivity is needed to replenish the emitted electrons. For TiPC, the goal is to develop a tynode with a (total) transmission electron yield (TEY) of 4 or higher for sub-1-keV PEs. A stack with 5 tynodes will have a gain of 1024, which is above the pixel detection threshold of a TimePix pixel [16], which allows for single-photon detection.

1.3.2. KEY CHALLENGES AND APPROACH

The development of TiPC requires interdisciplinary knowledge and collaboration. The MEMBrane project involves knowledge from different disciplines, such as material science, applied physics and electrical engineering. There are four key challenges in the development of TiPC, which require different approaches to overcome them. In section 1.4, the motivation of this thesis will be elaborated and its role in the development of TiPC.

The key challenges that have been identified in the development of TiPC can be formulated as:

- The theoretical understanding of electron emission of materials.
- The fabrication of ultra-thin transmission dynodes by means of Micro-ElectroMechanical System (MEMS)-based technology.
- The development of a prototype TiPC setup.
- The development of a measurement setup for transmission secondary electron emission.

The SEE properties are material-dependent as was shown in a review paper [17]. In general, dielectrics have been identified as high SEE materials. In literature, there is a variation in the reported secondary electron yield (SEY) of the same material, which can be partly ascribed to the differences in sample preparation and in the experimental conditions. The goal of applying theoretical models to materials that are available for MEMS fabrication is to predict its SEE properties. MEMS fabrication can be costly, since introducing new materials in a MEMS fabrication process would require adaptations and optimizations. As such, a Monte-Carlo simulation developed by Kieft and Bosch [18] was used and improved upon to predict the transmission SEE properties of silicon nitride (SiN), aluminum oxide (Al_2O_3) and magnesium oxide (MgO) [19, 20]. The effect of surface termination with hydrogen and alkali metals on silicon nitride was studied using Density Functional Theory (DFT) calculations [21, 22].

The second challenge is MEMS fabrication of ultra-thin membranes; the challenge lies in the thickness, or rather the thinness of the membranes. Monte-Carlo simulations have shown that the 'optimal' thickness for an Al_2O_3 is about 8 nm and for MgO it is 17 nm [19]. The goal is to investigate the possibility of applying MEMS materials and MEMS techniques to fabricate tynodes. There are two thin film deposition techniques that are used for ultra-thin film deposition: low-pressure chemical vapor deposition (LPCVD) and Atomic Layer Deposition (ALD). Three materials are considered for the SEE layer: LPCVD SiN, ALD Al_2O_3 and ALD MgO. A pixelated design in which an array of ultra-thin circular membranes suspended in a thicker membrane have been fabricated using these materials as SEE layer [23–25]. The ultra-thin membranes have a diameter of 30 µm and a pitch of 55 µm, which matches the pixel pitch of a TimePix chip. In addition, the effects of chemical and thermal treatment on the reflection secondary electron yield (RSEY) have been investigated, since the SEE materials are exposed to different chemicals and thermal conditions during fabrication that are unavoidable [26]. Though, additional chemical and thermal treatments can be incorporated in the fabrication process if it improves the transmission secondary electron yield (TSEY).

The third challenge is to build a prototype TiPC setup in which the separate and combined components of TiPC can be investigated [27]. The setup consists of an electron gun, a sample holder for a transmission dynode and a TimePix chip in a vacuum enclosure. It is used to study the response of a TimePix chip that is exposed to an incident electron beam. In addition, the setup provides an alternative method to determine the TSEY of tynodes.

The fourth challenge is to develop a new method for transmission SEE measurements. The experimental setups for transmission secondary electron emission measurements that have been reported consist of two semi-circular collectors: one side collects the RSE, while the other side collects the TSE [28–30]. The electron source is an electron gun that irradiates a thin self-supported film. This setup would work for films with an active surface that is larger than the electron beam diameter. However, as mentioned before, the diameter of the ultra-thin membranes presented in this work is in the order of tens of μm. An electron beam would irradiate multiple active membranes as well as the inactive supporting frame. This will lead to discrepancy in the measured reflection and transmission SEY and a correction method would be required. Also, it is difficult to identify the exact surface that is being irradiated. In addition, the intensity of the electron beam varies across the beam. This work focuses on the development of a new transmission SEE measurement setup that utilize the imaging capability of a scanning electron microscope (SEM). In the next section, the motivation and goals of this work will be outlined.

1.4. MOTIVATION AND OUTLINE OF THIS THESIS

THIS work focuses on two of the four key challenges as described in the previous section, namely MEMS fabrication and the development of a transmission SEE measurement setup. The goals of this thesis are:

- The development of a measurement method to determine the electron emission properties of ultra-thin tynodes within a SEM.
- To determine the electron emission properties of ultra-thin multi-layered titanium nitride (titanium nitride (TiN))/Al_2O_3 single-membrane tynodes.
- To measure the transmission electron yields of ALD TiN/MgO membranes within a square-array tynode.
- The fabrication of a new type of tynode with a corrugated membrane and to measure its transmission electron yield across the surface.

In this thesis, a collector-based method for determining the TEY of single membranes and tynodes will be presented. A collector-assembly is mounted within a modified SEM. Using the imaging capability of the SEM, the single-membranes and windows can be identified and targeted during transmission SEE measurement. The SEM setup is also used to identify charge-up behavior, which can provide feedback to improve MEMS fabrication parameters. More specifically, if the conductive layer is insufficient, charge-up will occur. Increasing the thickness of the conductive layer would often solve this problem.

In chapter 2, the electron emission properties of multi-layered TiN/Al_2O_3 membranes will be addressed. These single-membranes are relatively large in comparison with the windows in a square-array and are used to investigate the effect of film thickness on electron emission. First, the theory on (transmission) secondary electron emission will be introduced. Then, the method will be demonstrated and used to characterize the electron emission properties of the ultra-thin membranes. For these single-membranes, the fast and slow electrons will be separated.

In chapter 3, the measurements of the (total) reflection electron yield (REY) and TEY of ALD TiN/MgO square-array tynodes will be reported. The tynodes consist of 64×64 windows with a diameter of 30 µm. A modification to the measurement method will be presented that allows the TEY of multiple windows to be determined. By measuring the sample and collector current during image acquisition, a TEY map can be reconstructed that matches the SEM image. In addition, the effect of a strong electric field near the emission surface on the TEY will be investigated.

In chapter 4, a new tynode design will be presented. By depositing an ultra-thin film on a 3D silicon mold, a corrugated membrane can be formed, which can be two orders of magnitude larger in size. They are mechanically stronger in comparison with flat membranes, which allows for a large active surface for SEE without the need for additional support structures. The design and fabrication method will be first presented. Then these corrugated films will be characterized using the method presented in chapter 3.

In chapter 5, the main conclusions will be summarized. In chapter 6, recommendations will be given on how to further improve the tynodes and an outlook will be given on the development of TiPC.

There is some overlap between this chapter and the introductions of chapter 2, 3 and 4, as those chapters were published separately in a journal. The structures of those chapters have not been altered to preserve their readability. Readers can skim over the parts whenever they deem it to be repetitive.

REFERENCES

[1] H. Davson and E. S. Perkins, "Human eye," *Encyclopedia Britannica*, 2023.

[2] I. Fleck, M. Titov, C. Grupen, and I. Buvat, Eds., *Handbook of Particle Detection and Imaging*. Springer International Publishing, 2021.

[3] H. Villarraga-Gómez, E. L. Herazo, and S. T. Smith, "X-ray computed tomography: from medical imaging to dimensional metrology," *Precision Engineering*, vol. 60, pp. 544–569, 11 2019.

[4] J. J. Vaquero and P. Kinahan, "Positron Emission Tomography: Current Challenges and Opportunities for Technological Advances in Clinical and Preclinical Imaging Systems," *Annual Review of Biomedical Engineering*, vol. 17, pp. 385–414, 12 2015.

[5] The ATLAS Collaboration, "The ATLAS Experiment at the CERN Large Hadron Collider," *Journal of Instrumentation*, vol. 3, pp. S08 003–S08 003, 8 2008.

[6] S. Fukuda, Y. Fukuda, T. Hayakawa, E. Ichihara, M. Ishitsuka, Y. Itow *et al.*, "The Super-Kamiokande detector," *Nuclear Instruments and Methods in Physics Re-*

search, Section A: Accelerators, Spectrometers, Detectors and Associated Equipment, vol. 501, pp. 418–462, 4 2003.

[7] M. D. Eisaman, J. Fan, A. Migdall, and S. V. Polyakov, "Invited Review Article: Single-photon sources and detectors," *Review of Scientific Instruments*, vol. 82, 7 2011.

[8] D. R. Schaart, "Physics and technology of time-of-flight PET detectors," *Physics in Medicine & Biology*, vol. 66, p. 09TR01, 5 2021.

[9] E. Hergert and S. Piatek, "The WITS$ guide to selecting a photodetector," 2017.

[10] T. Hakamata, Ed., *Photomultiplier tubes*, 3rd ed. Hamamatsu Photonics K.K., 2007.

[11] "photomultiplier tube," *Wikipedia*.

[12] J. L. Wiza, "MICROCHANNEL PLATE DETECTORS," pp. 587–601, 1979.

[13] D. S. Bhattacharya, A. Bressan, C. Chatterjee, S. D. Torre, M. Gregori, A. Kiselev *et al.*, "Characterization of LAPPD timing at CERN PS testbeam," *Nuclear Instruments and Methods in Physics Research, Section A: Accelerators, Spectrometers, Detectors and Associated Equipment*, vol. 1058, 1 2024.

[14] "Single-photon avalanche diode," *Wikipedia*.

[15] H. van der Graaf, H. Akhtar, N. Budko, H. W. Chan, C. W. Hagen, C. C. Hansson *et al.*, "The Tynode: A new vacuum electron multiplier," *Nuclear Instruments and Methods in Physics Research Section A: Accelerators, Spectrometers, Detectors and Associated Equipment*, vol. 847, pp. 148–161, 3 2017.

[16] X. Llopart, R. Ballabriga, M. Campbell, L. Tlustos, and W. Wong, "Timepix, a 65k programmable pixel readout chip for arrival time, energy and/or photon counting measurements," *Nuclear Instruments and Methods in Physics Research Section A: Accelerators, Spectrometers, Detectors and Associated Equipment*, vol. 581, pp. 485–494, 10 2007.

[17] S. X. Tao, H. W. Chan, and H. van der Graaf, "Secondary Electron Emission Materials for Transmission Dynodes in Novel Photomultipliers: A Review," *Materials*, vol. 9, p. 1017, 12 2016.

[18] E. Kieft and E. Bosch, "Refinement of Monte Carlo simulations of electron–specimen interaction in low-voltage SEM," *Journal of Physics D: Applied Physics*, vol. 41, p. 215310, 11 2008.

[19] A. M. M. G. Theulings, "Optimisation of photon detector tynode membranes using electron-matter scattering simulations," Ph.D. dissertation, Applied Sciences, TU Delft, the Netherlands, 2020.

[20] A. Theulings, S. Tao, C. Hagen, and H. van der Graaf, "Monte Carlo simulation of the secondary electron yield of silicon rich silicon nitride," *Journal of Instrumentation*, vol. 17, p. P03008, 3 2022.

[21] S. X. Tao, A. M. Theulings, J. Smedley, and H. van der Graaf, "DFT study of electron affinity of alkali metal termination on clean and oxygenated β-Si_3N_4," *Diamond and Related Materials*, vol. 58, pp. 214–220, 9 2015.

[22] S. X. Tao, A. Theulings, J. Smedley, and H. van der Graaf, "DFT study of electron affinity of hydrogen terminated β-Si_3N_4," *Diamond and Related Materials*, vol. 53, pp. 52–57, 3 2015.

[23] V. Prodanović, H. W. Chan, A. U. Mane, J. W. Elam, H. van der Graaf, and P. M. Sarro, "Ultra-thin ALD MgO membranes as MEMS transmission dynodes in a timed photon counter." presented at the IEEE 30th Intern. Conf. on Micro Electro Mechanical Systems (MEMS), Las Vegas, US, jan. 2017, pp. 740–743.

[24] V. Prodanović, H. W. Chan, H. van der Graaf, and P. M. Sarro, "Ultra-thin alumina and silicon nitride MEMS fabricated membranes for the electron multiplication," *Nanotechnology*, vol. 29, p. 155703, 4 2018.

[25] V. Prodanović, "Ultra-thin MEMS fabricated tynodes for electron multiplication," Ph.D. dissertation, EEMCS, TU Delft, The Netherlands, 2019.

[26] V. Prodanović, H. W. Chan, A. U. Mane, J. W. Elam, M. M. Minjauw, C. Detavernier *et al.*, "Effect of thermal annealing and chemical treatments on secondary electron emission properties of atomic layer deposited MgO," *Journal of Vacuum Science & Technology A: Vacuum, Surfaces, and Films*, vol. 36, p. 06A102, 11 2018.

[27] T. van der Reep, B. Looman, H. Chan, C. Hagen, and H. van der Graaf, "Measurement of the transmission secondary electron yield of nanometer-thick films in a prototype Timed Photon Counter," *Journal of Instrumentation*, vol. 15, pp. P10 022–P10 022, 10 2020.

[28] J. Hölzl and K. Jacobi, "Sekundärelektronen-ausbeute an dünnen kohlenstoffolien in transmission und reflexion," *Surface Science*, vol. 14, pp. 351–360, 4 1969.

[29] F. O. Arntz and K. M. V. Vliet, "Secondary Emission of Thin Self-Supported Films of MgO," *Journal of Applied Physics*, vol. 33, pp. 1563–1566, 4 1962.

[30] J. Llacer and E. L. Garwin, "Electron-Phonon Interaction in Alkali Halides. II. Transmission Secondary Emission from Alkali Halides," *Journal of Applied Physics*, vol. 40, pp. 2776–2792, 6 1969.

2

MULTI-LAYERED TiN/Al_2O_3 TRANSMISSION DYNODES

The (secondary) electron emission from multilayered aluminum oxide (Al_2O_3)/titanium nitride (TiN) membranes has been investigated with a hemispherical collector system in a scanning electron microscope for electrons with energies between 0.3 and 10 keV. *These ultra-thin membranes are designed to function as transmission dynodes in novel vacuum electron multipliers. Two different types, a bi-layer and a tri-layer, have been manufactured by means of Atomic Layer Deposition (ALD) of aluminum oxide and sputtering of TiN. The reflection and transmission electron yield (σ_R, σ_T) have been measured for both types of membranes. In comparison, the tri-layer membranes outperformed the bi-layer membranes in terms of transmission electron yield for films with the same effective thickness. The highest transmission electron yield was measured on an Al_2O_3/TiN/Al_2O_3 film with layer thicknesses of 5/2.5/5* nm, *which had a maximum transmission electron yield $\sigma_T^{max}(E_0)$ of* 3.1(1.55 keV). *Furthermore, the bi-layer membranes have been investigated more in-depth by performing an additional measurement using a positive sample bias to separate the transmitted fraction η_T and the transmission secondary electron yield δ_T. The transmitted fraction was used to determine the transmission parameter p, which characterizes the interaction of primary electrons (PEs) in thin films. The transmission secondary electron yield was used to compare the energy transfer of PEs in films with different thicknesses.*

This chapter has been published in the Journal of Instrumentation **16**, 7 (2021) [1].

2.1. INTRODUCTION

2.1.1. NOVEL VACUUM ELECTRON MULTIPLIERS

VACUUM electron multipliers, such as PhotoMultiplier Tubes (PMTs), employ secondary electron emission (SEE) for photon detection [2]. The detection principle is the conversion of photons into photoelectrons by the photoelectric effect and subsequent electron multiplication in vacuum. A photoelectron, accelerated from the photocathode towards the first dynode, will generate multiple secondary electrons (SEs) upon impact. The SEs are then guided and accelerated towards the next dynode. As they traverse from dynode to dynode, their number increases, until the SEs are collected by the anode.

PMTs are one of the most sensitive photon detectors and are still widely used for single-photon detection due to its high gain, low noise and large acceptance surface. Though, there are a few disadvantages to the design. First, the time resolution in the order of a nanosecond is poor in comparison with Silicon Photomultipliers (SiPMs) with Single Photon Avalanche Diodes (SPADs) [3]. The time resolution depends on the spread in transit times of the SEs in the dynode section of a PMT. Also, the SEs are susceptible to magnetic fields, which exclude PMTs to be used in applications with strong magnetic fields. And lastly, the dynode stack makes PMTs voluminous, fragile and expensive.

The goal of the MEMBrane project is to develop a vacuum electron multiplier that outperforms PMTs in terms of time and spatial resolution [4]. The device, the Timed Photon Counter (TiPC), has the same detection principle as a PMT, but has transmission dynodes (tynodes) as multiplication stages instead of (reflective) dynodes (Figure 2.1). tynodes are extremely thin membranes where an impinging primary electron (PE) on the frontside releases multiple secondary electrons from the backside. This distinctive property allows tynodes to be closely stacked on top of each other. The distance between neighboring stages, in comparison with dynodes in PMTs, is greatly reduced and the electric field is nearly homogenous. As a result, the time resolution improves: the pulse width and the rise time of the signal will be smaller due to the more uniform and shorter electron paths. In addition, the susceptibility to magnetic fields is reduced due to the increased electric field strength. In terms of spatial resolution, 2D spatial information is gained by combining the planar tynode stack with a CMOS-pixelchip (TimePix) as readout. Lastly, TiPC is a smaller and more compact photodetector in comparison with a PMT.

A tynode is an ultra-thin membrane that (1) consist of a material with a high secondary electron yield (SEY), (2) is mechanically strong and (3) is electrically conductive. The transmission secondary electron yield (TSEY) is defined as the ratio between the number of incoming PE, with an energy of E_0, and the number of outgoing SEs in transmission. For TiPC, the goal[1] is to achieve a TSEY of 4 or higher for PEs with sub-2 keV energy. As such, mechanically strong and thin membranes are required, since the range of PEs is energy dependent. *In-plane conductivity* is required to replenish the emitted electrons in the irradiated region of the membrane by providing an electrical path to the conductive mesh in which the membranes are suspended, otherwise charge-up effects will occur during prolonged electron irradiation.

[1] the updated goal is to achieve a TEY of 4 or higher for PEs with sub-1 keV energy.

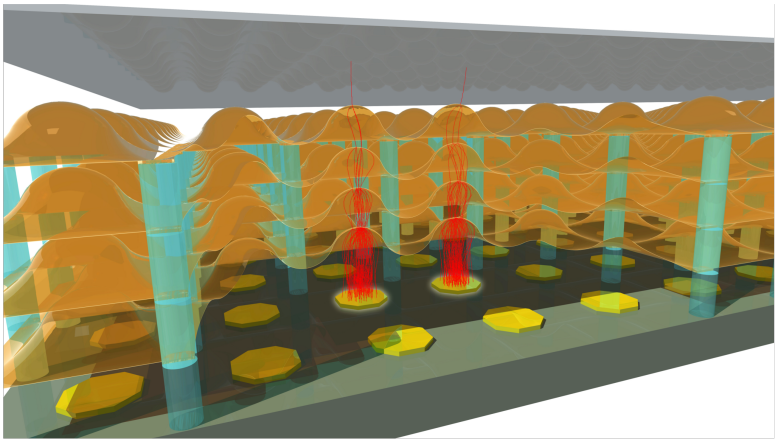

Figure 2.1: The Timed Photon Counter consists of a traditional photocathode, a stack of tynodes and a TimePix chip within a compact vacuum enclosure. The electric potential between each tynode in the stack increases step-wisely from top to bottom. A soft photon can emit a photoelectron from the photocathode, which is then accelerated towards the first tynode due to the electric field. On impact, the incoming electron generates multiple transmission secondary electrons (TSEs) from the ultra-thin tynode, which escape from the backside. The concave surface of the tynode bundles and accelerates the TSEs towards the next tynode. The multiplication process repeats m times for each layer. Eventually a number of ${\sigma_T}^m$ electrons appear above the individual pixel and are detected by the digital circuitry of the TimePix chip.

2.1.2. TRANSMISSION SECONDARY ELECTRON EMISSION

Secondary electron emission is described as a three-step process: *generation*, *transport* and *escape* of internal SEs [5, 6]. This model can be extended to thin membranes by including the exit surface of the membrane in transmission (Figure 2.2). The first step of the model treats PE interaction, energy transfer and SE generation. A PE that interacts within a thin membrane will scatter and lose energy. Some of the energy is used to generate internal SEs. The PE itself can be reflected, absorbed or transmitted by the membrane. Reflected PE are designated as backscattered electron (BSE), while transmitted electrons as forward-scattered electron (FSE). They are distinguished from SEs by their energy, which is $E_{se} > 50$ eV. The second step describes the transport of internal SEs within the material. The band gap model is used to explain the difference in transport in metal, semiconductors and dielectrics [5, 6]. The wide band gap of dielectrics allows SEs that are promoted to the conduction band to travel a relatively large distance with few interactions. This increases the probability of the SEs to reach the surface. The third step models the escape of internal SEs into vacuum at the solid-vacuum boundary. Internal SEs with sufficient energy to overcome the work function or electron affinity can escape into vacuum. Only internal SEs that are generated near the surface have a chance to escape. The escape probability is given as an exponential decay function with λ the mean free path of SEs. The secondary electrons that escape from the entrance are designated as reflection secondary electron (RSE) and from the exit as transmission secondary electrons (TSEs).

The reflection secondary electron yield (RSEY) of a surface depends on its material properties and surface condition. In general, dielectrics have higher yields in compar-

ison with semiconductors and metals [5, 6]. This is attributed to the wide band gap of dielectrics which benefits the transport of internal SEs. Surface treatment, such as caesiation and hydrogen-termination, can lower the electron affinity (EA), which will also increase the escape probability of internal SEs. In some cases, even negative electron affinity (NEA) can be achieved; an internal SE that reaches the surface will encounter no barrier and will be pushed into vacuum. This is beneficial for SEE. The (total) reflection electron yield (REY) of C(100) diamond, for instance, increased from 3 to 60 and 132 by cesium (Cs)- and hydrogen (H)-termination respectively [7].

For transmission SEE, the thickness of the membrane is an additional parameter that affects the TEY. The onset of transmission SEE is expected to occur when PEs are expected to penetrate through the tynode. This characteristic is defined as the critical energy E_c for which 1% of the PEs manages to pass through: $\eta_T(E_c) = 0.01$ [8]. The coefficient η_T is the FSE coefficient or the transmitted fraction. A second characteristic (tied to the thickness) is the energy $E_0^{\max}$ at which the maximum TEY $\sigma_T^{\max}$ is achieved: $\sigma_T^{\max}(E_0^{\max})$. Both are unique defining features of a TEY curve correlated to the thickness of the membrane.

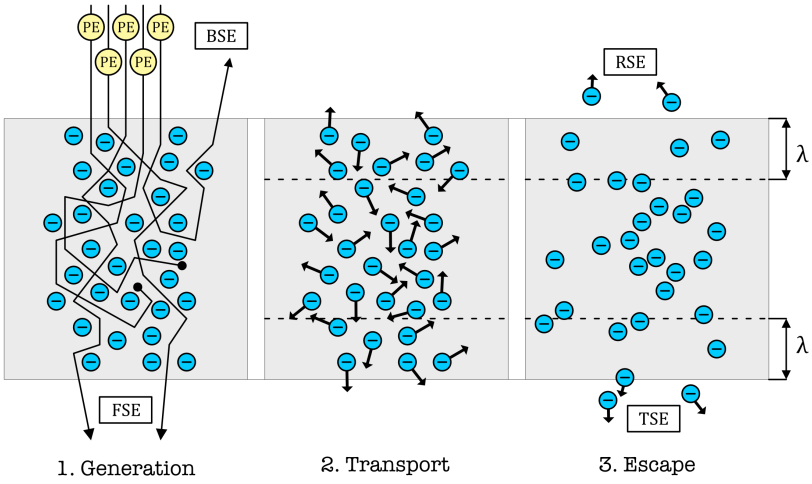

Figure 2.2: Three-step model of SE generation. The three steps are treated independently in the elementary theory of SEE. The first step describe energy transfer of PEs in the film/bulk. The second step models the transport of internal SEs. The third step describe the escape probability of SEs from the material into vacuum.

The distance that a PE with energy E_0 can travel is defined as the range and is given by $R = CE_0{}^n$, where C is a constant that is material dependent and n a constant that depends on the energy-range of the PEs [9]. There are a variety of range-energy relations [10]. The accuracy of these relations depends on the material considered and the energy of the PE. For sub-10 keV electrons and alumina as material, the range-energy relation given by Fitting [8] is the most accurate and is given by

$$R = 90\rho^{-0.8}E_0^{1.3} \tag{2.1}$$

where R is the range in nm, ρ the density given in g/cm^3 and E_0 the primary beam energy in keV. The range R of a PE in different materials will differ, which makes comparison of composite films to single-material films difficult. However, an effective layer method can be applied to films with different materials [11]. The contribution to the stopping power of material 2 can be replaced by material 1 with an effective layer thickness d_1^{eff} given by

$$d_1^{\text{eff}} = \left(\frac{d_1}{R_1}\right)^{p_1/p_2} R_2 \tag{2.2}$$

where $p_{1,2}$ is the transmission parameter and $R_{1,2}$ is the range in the first and second material respectively. The total effective film thickness is then given by: $d = d_1^{\text{eff}} + d_1$.

A basic SEE measurement setup consists of an electron gun, a sample holder and an electron collector, which are placed inside a vacuum chamber. The standard procedure is to measure the SE current from the surface and compare it to the PE current. Depending on the method, the ratio is either the REY or RSEY. In literature, the distinction between RSEs and BSEs is often not made and one can assume that their combined yield is reported. Also, the reported REY of the same material varies widely, which is attributed to the different experimental conditions [5, 6]. For instance, the surface condition plays an important role as was shown on alkali halide single crystals by Whetten [12]. The crystals were cleaved in vacuum and the pristine surface had a higher REY. SEE measurements are often performed in dedicated ultra-high vacuum (UHV) chambers with the option of surface and/or thermal treatments.

SEE measurements on dielectrics are more challenging due to the build-up of charge on the surface [13]. The recommended strategy is to limit the electron dose, which can be achieved by using a pulsed electron gun [12, 13] and/or to neutralize the charge with a flood gun between measurements [14]. A different approach is to determine the REY by measuring the surface charge using the Kelvin probe method [15].

For transmission SEE measurement, a dual collector setup can be used to measure the REY and TEY [8]. The disadvantage of this 'closed' system is the difficulty of targeting the sample surface. If the membrane size is extremely small, a part of the electron beam will irradiate the inactive surface. Therefore, a modified collector method was developed to determine the transmission (secondary) electron yield within a scanning electron microscope (SEM) [16]. The imaging capability of the SEM was used to locate and to direct the electron beam on the ultra-thin membranes. Despite using a continuous beam, charge-up effects were not observed on films/membranes on which a conductive titanium nitride (TiN) layer was sputtered.

A caveat of this method is the lack of UHV in the SEM, which operates at 1×10^{-6} mbar instead of 1×10^{-9} mbar or lower. As a result, surface contamination can form after prolonged surface irradiation [17]. The contamination rate depends on the electron dose per unit surface and can be lowered by scanning the electron beam over the surface. A comparison between this setup and a dedicated UHV system have been made by measuring the RSEY of a silicon nitride (SiN) and an aluminum oxide (Al_2O_3) film [4]. The results were in good agreement and contamination effects were not observed. However, dedicated surface termination studies should be performed in UHV systems.

2.1.3. TRANSMISSION DYNODE

In the past, different groups of materials were considered as tynode material, such as alkali halides, semiconductors and diamond. One of the first working transmission-type photomultipliers has been built by Sternglass & Wachtel. [18, 19]. The tynodes consist of porous potassium chloride (KCl) deposited on top of an aluminum (Al) foil. The high TEY of porous materials is due to the build-up of charge inside the pores of the material, which results in a strong electric field where (secondary) electrons are accelerated internally causing an avalanche type of SEE. The typical inter-stage operating voltage is 5 keV with a maximum TEY $\sigma_T^{\max}$ of 8. Despite the high TEY, the required high voltage for a multi-stage device limits its applicability. Also, the lifetime of the devices was poor and further research in the aging mechanism was needed [20]. The TEY of other alkali halides (CsI, KCl, NaF and LiF) have been measured by Llacer & Garwin [21]. They were deposited onto an Al/Al_2O_3 membrane as support, which increased the overall film thickness. The highest TEY of 8 (8 keV) was measured for CsI. The best performing alkali halide was reported by Hagino et al. on caesium activated CsI. They achieved a TEY of 27 (9 keV) for Al_2O_3/Al/CsI(Cs) films [22]. A second group of materials that was considered were semiconductors, such as silicon (Si) and gallium arsenide (GaAs), that benefitted from NEA. A TEY of 725 (25 keV) for a 4-5 µm thick Si film with NEA was achieved by Martinelli [23]. More recently, various types of diamond have been studied as SEE materials for transmission dynodes [24–27]. The highest TEY of 5 (7 keV) was obtained for nano-crystalline chemical vapor deposition diamond. Although the results are promising, it is unclear whether thinner nano-crystalline diamond can be manufactured with the same quality, since the growth process requires nucleation sites.

The large PE energy that is required to achieve the high TEY makes these tynodes impractical. Ideally for TiPC, the tynodes need to perform optimally for sub-2 keV electrons. The limiting factor is thus the film thickness. After a thorough review, it became clear that the tynode needs to be self-supporting [28]. The choice of materials is therefore limited to materials that are mechanically strong and have a high SEY. Accordingly, we approached the problem from a micro-fabrication/engineering point of view. SiN tynodes were fabricated by low-pressure chemical vapor deposition (LPCVD) and aluminum oxide tynodes by means of Atomic Layer Deposition (ALD) [16, 29]. Monte-Carlo simulation has shown that the optimum thickness for aluminum oxide tynodes is about 10 nm [4]. Therefore, the ultra-thin membranes, with a diameter of 10 – 30 µm, were suspended within a supporting mesh with an array of 64-by-64 small windows [16]. A TEY of 1.57 (2.85 keV) was measured for TiN/SiN films and a TEY of 2.6 (1.45 keV) for TiN/Al_2O_3 films.

TiN was chosen as a conductive layer to provide in-plane conductivity. The added layer does increase the thickness, but has a relatively low stopping power due to the low Z value of TiN. Other conductive materials were considered, such as metals (Al, Cr), but they will most likely oxidize during the fabrication process, whereas TiN is chemically inert in ambient conditions [30]. Charge-up within the alumina layer was not observed, i.e. the emission current is constant during exposure. The mechanism that provides *normal-to-the-plane* conductivity from the conductive layer to the charged region in the dielectric film can be either explained by electron-beam induced current (EBIC) [31] and/or electron tunneling [32].

In this paper we will determine and compare the (transmission) SEE of two types of multilayered membranes: a bi- and a tri-layer. The conductive layer of the bi-layer TiN/Al_2O_3 membrane is deposited after releasing the membrane. Due to the topography of the surface, the sputtered TiN layer is less uniform, which increases the risk of a disconnected layer. The fabrication process of the tri-layer $Al_2O_3/TiN/Al_2O_3$ membrane improves the reliability of the conductive layer by sandwiching it between two Al_2O_3 layers before release. Furthermore, the effect of the film thickness on the transmission (secondary) electron emission will be discussed. The TEY is separated into the transmitted fraction/forward-scattered electron yield (FSEY) and TSEY, which will be used to characterize the PE interaction in the thin films.

2.2. MATERIALS & METHODS

2.2.1. PREPARATION OF SAMPLES

THE fabrication process of the ultra-thin composite membranes is similar to the fabrication process of tynodes presented in ref. [16], but the process is simplified by omitting the support mesh. Instead, a single square membrane with a width of 400 µm is released from the substrate. This basic design is not intended to be used in an actual detector, but is designed with the goal to characterize the transmission (secondary) electron emission of the multi-layer membranes. In figure 2.3, the flowcharts of the fabrication process of two types are given: a TiN/Al_2O_3 bi-layer and a $Al_2O_3/TiN/Al_2O_3$ tri-layer membrane. The conductive layer is applied as a post-process in the former (figure 2.3 A5), while it is integrated in the process flow of the latter (figure 2.3 B2). The additional alumina layer serves as a protection layer against the hydrofluoric (HF) vapor etch (figure 2.3 B2).

For the TiN/Al_2O_3 bi-layer membrane, a 4-inch p-type (5-10 Ω cm) wafer with a thickness of (500 ± 15) µm is used as a substrate. The Si substrate is oxidized in a wet thermal environment at 1000 °C until 300 nm of silicon dioxide (SiO_2) is formed. This layer will act as a stopping layer and as a sacrificial layer in the process. ALD alumina is grown on top in a thermal ALD ASM F-120 reactor using trimethyl-aluminum and water as a precursor and reactant, respectively (figure 2.3 A1), at a temperature of 300 °C. The thickness is varied by choosing different numbers of cycles. Plasma-enhanced chemical vapor deposition (PECVD) SiO2 is then deposited on the front side to protect the alumina layer and on the backside as a masking layer (A2). The Si substrate is removed by Deep-Reactive Ion Etching (DRIE) (A3). After this step, the wafer is cleaved into 15-by-15-mm

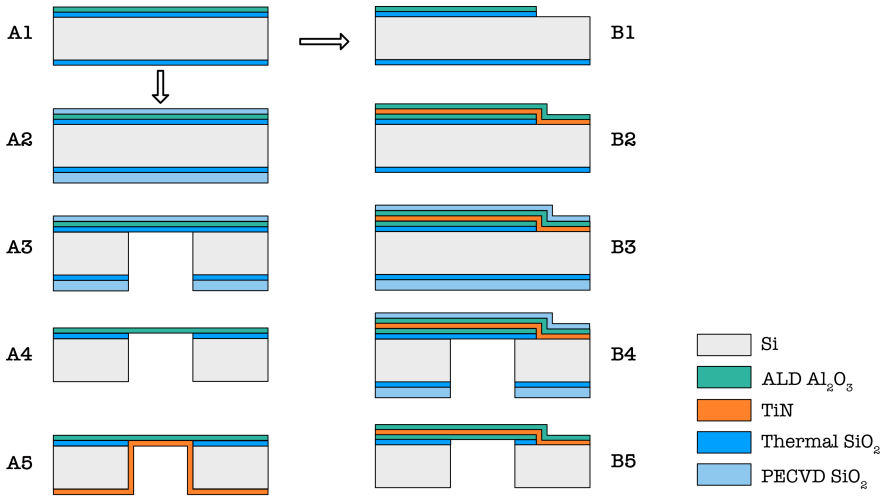

Figure 2.3: (A1-A5) Flow chart of the fabrication process of the TiN/Al_2O_3 Bi-layer membrane. (B1-B5) Flow chart of the Al_2O_3/TiN/Al_2O_3 Tri-layer membrane.

pieces along predefined break lines. For the final release, the SiO2 layers are removed in an HF vapor etch chamber (A4). As a last step, TiN is sputtered as a post-process (A5). This allows the thickness of the conductive layer to be varied and optimized. The membranes have a surface area of 400 µm by 400 µm and film thicknesses [$d_{TiN}/d_{Al_2O_3}$] of 2.5/10 nm, 5.7/25 nm or 5.7/50 nm.

For the Al_2O_3/TiN/Al_2O_3 tri-layer membranes, the process is the same till the first ALD alumina deposition (A1). After this step, a small patch of alumina and SiO2 is removed by plasma etching to expose the Si substrate (B1). TiN is then sputtered onto the wafer forming a continuous layer that is in contact with the Si substrate. Another ALD alumina layer is used to encapsulate this layer (B2). This encapsulation is needed to protect the TiN layer against HF vapor in the last step. The next steps are similar to the previous process. PECVD SiO2 is applied as protection and masking layer (B3). The Si is removed by DRIE (B4) and the wafer is cleaved into 15-by-15-mm dies. The membrane is released by HF vapor etching (B5). The membranes have a surface area of 400 µm by 400 µm and film thicknesses [$d_{Al_2O_3}/d_{TiN}/d_{Al_2O_3}$] of 5/2.5/5 nm or 12.5/5.7/12.5 nm.

2.2.2. EXPERIMENTAL METHOD

The experimental setup is designed to be mounted onto the moving stage of a Thermo Fisher NovaNanoLab 650 Dual Beam SEM. A teflon holder is attached to the stage in which the setup is fixed. Teflon insulates the sample holder electrically from the stage and the chamber. The SEM has an electron source that provides a continuous electron beam with energy ranging from 0.3 keV to 30 keV. The typical beam current for these experiments is in the pA range, but it can be increased to a few nA if necessary. Though, the current is usually kept to a minimum in order to avoid charge-up effects. The opera-

tional vacuum level ranges from 1×10^{-5} down to 1×10^{-6} mbar.

A schematic representation of the experimental setup is given in figure 2.4. It consists of 3 separate electrodes: a collector, retarding grid and sample holder. They are electrically insulated from each other with sheets of kapton foil. Each electrode is connected via a feedthrough to a Keithley 2450 Source meter. This allows each electrode to be biased from −200 V to 200 V, while measuring the currents simultaneously. The sample is clamped inside the copper sample holder. Silver emulsion is applied on the Si substrate of the samples to ensure good electrical contact between the sample and holder. Prior to the measurements, the primary beam current I_0 as a function of the electron beam energy E_0 is measured within a Faraday cup, which is drilled into the sample holder close to the sample. The beam current is stable over the course of a day, so measuring the current once for each beam energy is sufficient.

At the start of the measurement, the electron beam is moved towards the 'active' membrane on the sample. The measurement is performed in image acquisition mode, which has the benefit that only the imaged surface is being irradiated by the beam. Corrections are not needed for any induced currents on the surrounding 'inactive' parts of the sample. Also, charge-up effects are mitigated by distributing the beam over a larger surface. The continuous surface scan has a horizontal field width of 366 µm and a vertical field width of 316 µm with a resolution of 1024 x 884 pixels. This is approximately 0.116 mm^2 over which the current is spread. The dwell time (per pixel) is 1 µs and the frame time is 0.94 s. For each beam energy E_0, the surface is scanned for 20 s, in which multiple frames are taken, before shifting to a higher energy. The background current is measured before and after each reading. By taking multiple frames, charge-up effects can be identified with the SEM: the contrast of the image will change in case of charging. Also, the emission currents will change over time as well. If the in-plane conductivity of the sample is sufficient, the emission currents remain constant. In this case, the average emission current is used to determine the yields.

This method is a combination of a sample-biasing and a classical collector method; the transmission current is measured directly in the collector, while the reflection current is determined indirectly by subtracting the transmission current from the sample current. The method distinguishes fast electrons ($E_{se} > 50$ eV) from true secondary electrons ($E_{se} < 50$ eV) by biasing the electrodes in the measurement setup. This requires two separate measurements where the sample is first negatively biased (−50 V) and then positively biased (50 V). The PE energy E_0 is adjusted by −50 eV for the former and +50 eV for the latter.

For a negative bias, the sample holder, retarding grid and collector are biased to −50 V, 0 V and 0 V, respectively. The negative bias repels fast and slow electrons from the sample on the reflection and transmission side. The transmission coefficient $\sigma_T(E_0)$ is determined by measuring the transmission current with the retarding grid and collector and is given by:

$$\sigma_T(E_0) = \frac{I_{RG-} + I_{C-}}{I_0} \tag{2.3}$$

where E_0 is the electron energy of the PE, I_0 is the primary beam current, I_{RG-} is the retarding grid current and I_{C-} collector current. The minus-subscript indicates that the

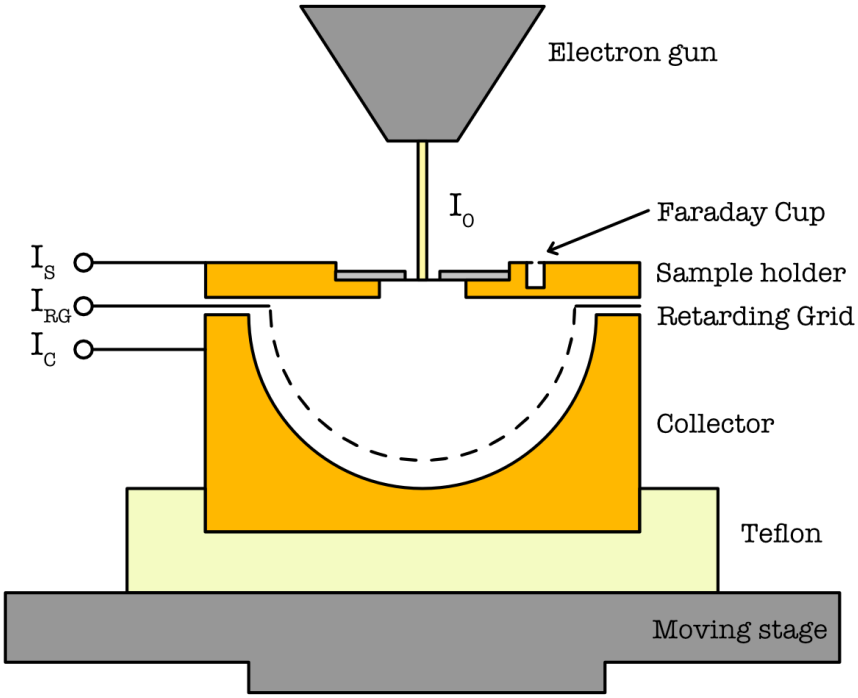

Figure 2.4: Schematic drawing of the experimental setup. The primary beam current I_0 is measured within the Faraday cup. The sample holder, retarding grid and collector are electrically insulated from each other with Kapton foils. Each is connected via feedhrough to source meters.

current is measured under a negative sample bias. The total emission $\sigma(E_0)$, which is the sum of the reflection coefficient $\sigma_R(E_0)$ and transmission coefficient $\sigma_T(E_0)$, is determined by measuring the sample current and is given by:

$$\sigma(E_0) = \frac{I_0 - I_{S-}}{I_0} \tag{2.4}$$

where I_{S-} is the sample current. The reflection coefficient is then given by:

$$\sigma_R(E_0) = \sigma(E_0) - \sigma_T(E_0) = \frac{I_0 - I_{S-} - I_{RG-} - I_{C-}}{I_0} \tag{2.5}$$

An additional measurement with a positive biased sample can be performed to separate the fast electrons from the slow ones. The sample holder, retarding grid and collector are biased to 50 V, 0 V and 0 V, respectively. The positive voltage retracts the slow electrons to the sample, while allowing fast electrons ($E_{se} > 50$ eV) to escape. The retarding grid prevents tertiary electrons from the collector wall (i.e. unwanted SEs induced within the setup) to flow back towards the sample. The FSE coefficient $\eta_T(E_0)$ is determined by measuring the transmission current with the retarding grid and collector and is given by:

$$\eta_T(E_0) = \frac{I_{RG+} + I_{C+}}{I_0} \tag{2.6}$$

where E_0 is the electron energy of the PE, I_0 is the primary beam current, I_{RG+} is the retarding grid current and I_{C+} collector current, where the plus-subscript indicates a positively biased sample. Since $\sigma_T(E_0) = \eta_T(E_0) + \delta_T(E_0)$, the TSE coefficient $\delta_T(E_0)$ is given by

$$\delta_T(E_0) = \frac{I_{RG-} - I_{C-}}{I_0} - \frac{I_{RG+} + I_{C+}}{I_0} \tag{2.7}$$

The sample current I_{S+} is again the sum of the reflection and transmission current. In this case

$$\eta_T(E_0) + \eta_R(E_0) = \frac{I_0 - I_{S+}}{I_0} \tag{2.8}$$

After substituting $\eta_T(E_0)$, the BSE coefficient $\eta_R(E_0)$ is given by:

$$\eta_R(E_0) = \frac{I_0 - I_{S+} - I_{RG+} - I_{C+}}{I_0} \tag{2.9}$$

The RSE coefficient $\delta_R(E_0)$ can be determined by using the definition of the total emission coefficient: $\sigma(E_0) = \eta_R(E_0) + \delta_R(E_0) + \eta_T(E_0) + \delta_T(E_0)$, from which it follows that

$$\delta_R(E_0) = \sigma(E_0) - \eta_T(E_0) - \delta_T(E_0) - \eta_R(E_0) \tag{2.10a}$$

$$\delta_R(E_0) = \frac{I_0 - I_{S-} - I_{RG-} - I_{C-}}{I_0} - \frac{I_0 - I_{S+} - I_{RG+} - I_{C+}}{I_0} \tag{2.10b}$$

With eq. (2.7), (2.8), (2.9) and (2.10b), all relevant yields can be calculated from the measured currents.

2.3. RESULTS

2.3.1. BI-LAYER MEMBRANE

In figure 2.5, a schematic drawing of a bi-layer membrane is given with all the currents that flow to and from the irradiated region. The flat side of the sample with the ALD alumina layer is facing downwards in the transmission direction, while the window opening in the Si substrate is facing upwards. The conductive TiN layer is deposited inside the window opening.

The (secondary) electron yield curves as a function of the PE energy E_0 are given in figure 2.6 for bi-layer TiN/Al_2O_3 membranes with thicknesses of 2.5/10, 5.7/25 and 5.7/50 nm, respectively. The total effective film thickness d is calculated with equation (2.2). For low-Z materials, the transmission parameters are assumed to be approximately equal: $p_1 \cong p_2$. The conversion factor is then simply the ratio between the ranges: $R_{Al_2O_3}/R_{TiN} \cong 1.51$, i.e. the TiN layer can be replaced by an Al_2O_3 layer with an effective thickness that is 1.51 times larger. It is listed in table 2.1 along with the transmission yield curve characteristics; the critical energy E_c, maximum TEY $\sigma_T^{max}(E_T^{max})$ and maximum TSEY $\delta_T^{max}(E_0^{max})$.

The reflection SEE coefficients are represented by the red curves in figure 2.5. For a bi-layer membrane, the contribution to the reflection yields is from the TiN layer. The BSE coefficient $\eta_R(E_0)$ is close to zero for all three thicknesses. There are two factors that

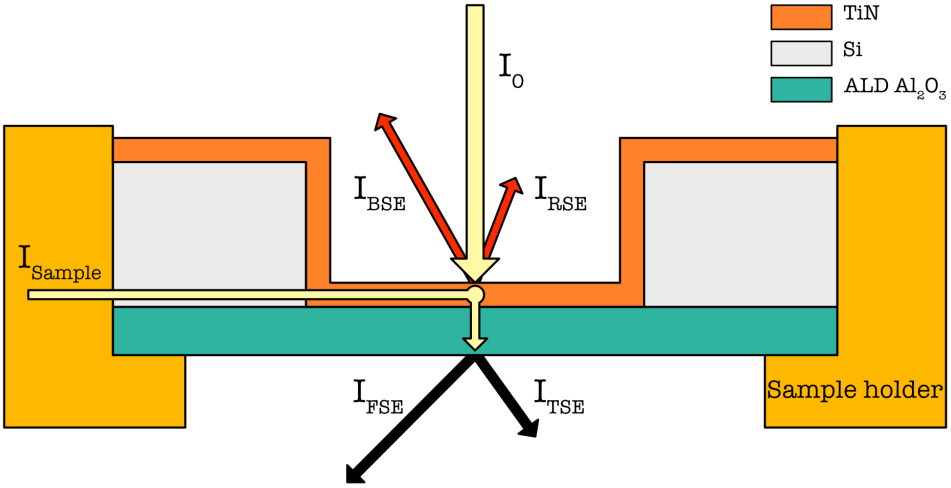

Figure 2.5: The currents to and from a bi-layer membrane irradiated by an electron beam. TiN is sputtered into the window opening on the reflection side to provide a conductive path from the sample holder to the irradiated region.

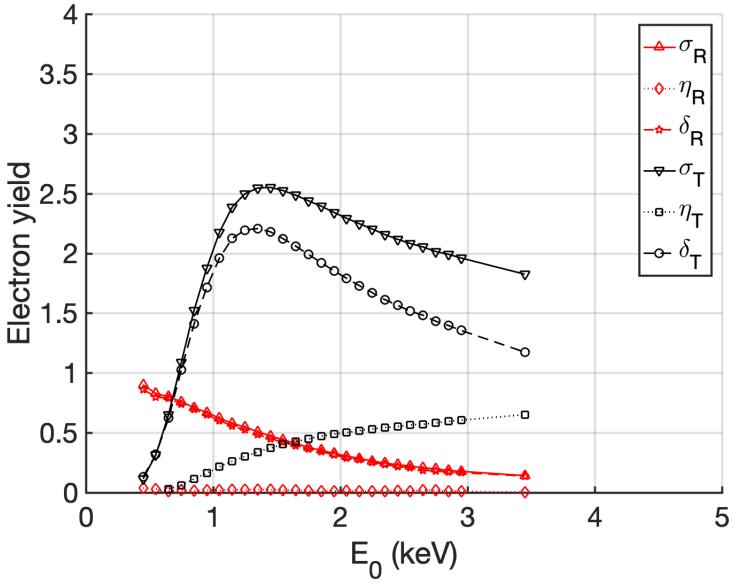

(a) 2.5 / 10 nm

Figure 2.6: Electron emission coefficients of a bi-layer membrane TiN/Al_2O_3 with thicknesses $d_{TiN}/d_{Al_2O_3}$

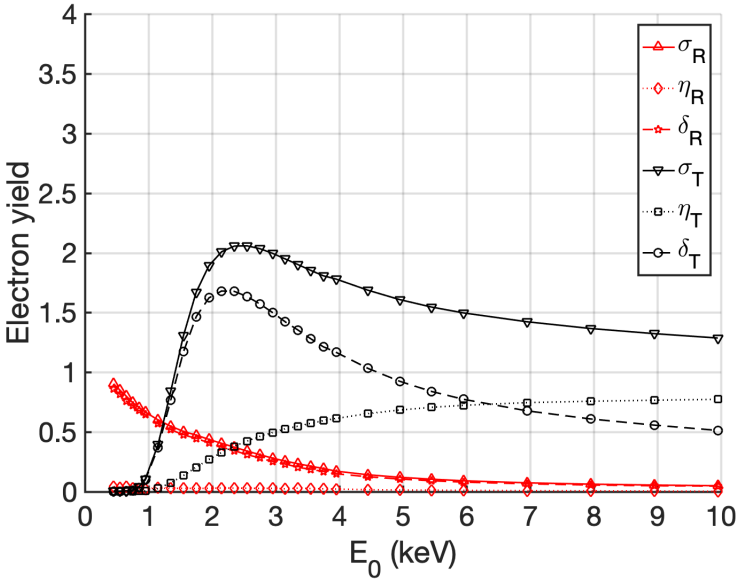

(b) 5.7 / 25 nm

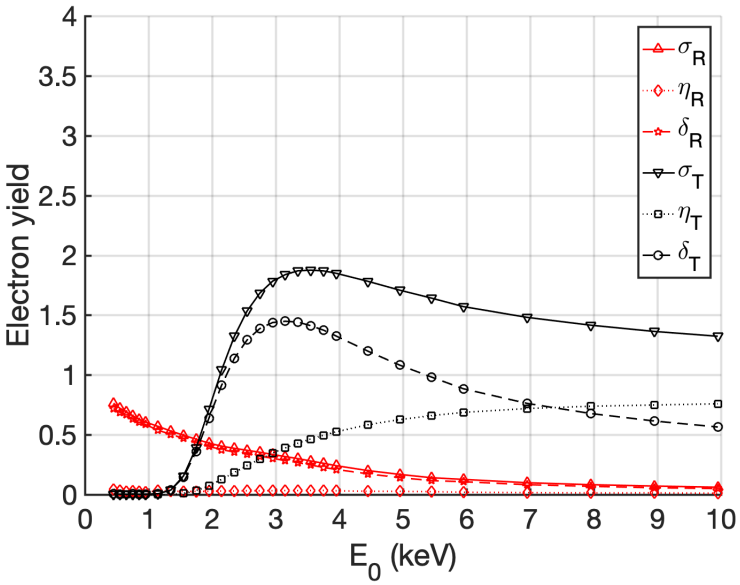

(c) 5.7 / 50 nm

Figure 2.6: Electron emission coefficients of a bi-layer membrane TiN/Al_2O_3 with thicknesses $d_{TiN}/d_{Al_2O_3}$

Table 2.1: Summary of important electron emission values of all composite membranes. The total effective thickness d is calculated with eq. (2.2). The density of ALD Al_2O_3 and sputtered TiN are 3.1 g/cm^3 and 5.2 g/cm^3, respectively.

	$d_{Al_2O_3}$ (nm)	d_{TiN} (nm)	$d_{Al_2O_3}$ (nm)	d (nm)	d ($\frac{\mu g}{cm^2}$)	σ_T^{max}	E_T^{max} (keV)	δ_T^{max}	E_0^{max} (keV)	E_c (keV)
Bi	-	2.5	10	13.8	4.40	2.6	1.45	2.2	1.35	0.5
Bi	-	5.7	25	33.6	10.7	2.1	2.55	1.7	2.15	1.0
Bi	-	5.7	50	58.6	18.5	1.9	3.55	1.5	3.15	1.4
Tri	5	2.5	5	13.8	4.40	3.1	1.55	-	-	-
Tri	12.5	5.7	12.5	33.6	10.7	2.7	2.75	-	-	-

contribute to this low value. First, the BSE yield of membranes and foils are expected to be lower in comparison with their bulk counterpart [33, 34]. Second, the Si window frame reduces the field of view for BSEs and will recapture some. The RSE coefficient $\delta_R(E_0)$ is below 1 and is lower than expected. The reduction in yield can again be attributed to recapture. The maximum REY on a bulk TiN sample can range from 1.4 to 2.8 for a PE energy of 300 eV depending on the deposition technique and conditions [35, 36].

The reduction in REY due to the Si window frame is estimated by using a test sample. In appendix A, a p-type Si membrane with widths of 400 µm is used to estimate the reduction in yield due to recapture. The aspect ratio of the window and the wall is ~1.2 and is the same as the other samples. The emission surface of the Si membrane on both sides is identical, so the difference in yield is solely due to the presence of the window walls on one side. When the window opening is facing the electron gun, the REY was reduced by 35 to 45%. When the window opening was facing away, the TEY was reduced by 15 to 30 %.

The transmission SEE coefficients are represented by the black curves in figure 2.6. The transmission side consists of Al_2O_3. The FSE coefficient $\eta_T(E_0)$ is the fraction of the PE beam that penetrates through the membrane and contains electrons with energy $E > 50$ eV. Thin films become transparent for high-energetic electrons. As such, almost all PEs should be collected by the collector, i.e. the FSE curve approach 1 for high PE energies. However, the curves converge to 0.8 instead. The discrepancy can be attributed to (back)scattering of the transmitted PEs on the retarding grid and the collector wall, which will induce tertiary currents that can lower the net transmission current. The effect of tertiary currents on the transmitted fraction will be discussed in 2.4.2. In appendix 2.5, a correction term is estimated by taking scattering events in the collector into account.

The TSE coefficient $\delta_T(E_0)$ represents electrons with $E < 50$ eV, which originates from the Al_2O_3 layer within the escape depth. The initial rise of the TSEY curve starts at the threshold energy E_{th}. At this energy, the first (slow) secondary electrons emerge from the membrane in transmission. It is correlated to the critical energy E_c for which 1% of the PEs are transmitted. Another characteristic is the maximum TSEY obtained with PEs with energy $E_0^{max} : \delta_T^{max}(E_0^{max})$. The thinnest membrane with a total effective thickness of 13.8 nm has the highest maximum TSEY of 2.21 (1.35 keV).

The (total) transmission electron coefficient $\sigma_T(E_0)$ is the sum of $\delta_T(E_0)$ and $\eta_T(E_0)$.

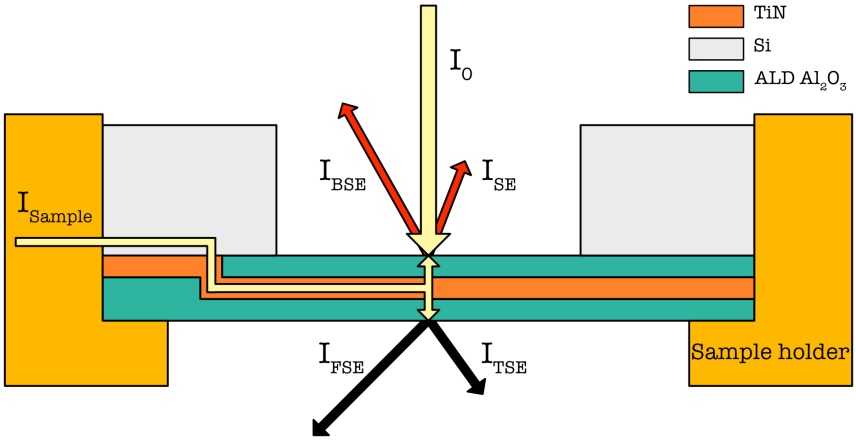

Figure 2.7: The currents to and from a tynode with a sandwiched TiN layer irradiated by an electron beam. The reflection side is also covered with Al_2O_3, which protects the conductive layer during the fabrication process.

In literature, the distinction between $\delta_T(E_0)$ and $\eta_T(E_0)$ is often not made. Unless specified, usually the total transmission yield $\sigma_T(E_0)$ is given. The performance of a tynode can be expressed by the maximum TEY: $\sigma_T^{\max}(E_T^{\max})$. The highest maximum TEY of 2.55 (1.45 keV) was measured on a membrane with $d = 13.8$ nm. The maximum TEY and TSEY of the other membranes are listed in table 2.1.

2.3.2. TRI-LAYER MEMBRANE

In figure 2.7, a schematic drawing of a tri-layer membrane is shown. The TiN layer is sandwiched between two layers of alumina. The three layers are deposited subsequently in the fabrication process, which improves the reliability of the conductive layer. The currents flowing to and from the irradiated regions are indicated by the arrows.

In figure 2.8a, the reflection $\sigma_R(E_0)$ and transmission $\sigma_T(E_0)$ coefficients of a bi-layer membrane TiN/Al_2O_3 are compared to a tri-layer membrane $Al_2O_3/TiN/Al_2O_3$. The thicknesses of the layers for the two membranes are 2.5/10 nm and 5/2.5/5 nm, respectively, with a total effective thickness of 13.8 nm for both.

The reflection coefficient $\sigma_R(E_0)$ is significantly smaller for the bi-layer compared to the tri-layer, since the material of the emission surfaces are different. The REY of TiN is lower than that for Al_2O_3. Therefore, a direct comparison of the REY is not useful.

The transmission electron coefficient $\sigma_T(E_0)$ for both type of membrane has the same threshold energy E_{th}. This shows that both membranes have a similar thickness and stopping power. However, the maximum TEY of 3.1 (1.55 keV) is higher for the tri-layer membrane compared to the bi-layer yield of 2.6 (1.45 keV). The better performance is also observed for the membrane with $d = 33.6$ nm as shown in figure 2.8b. The maximum TEY is 2.7 (2.75 keV) for the tri-layer and 2.1 (2.55 keV) for the bi-layer. Hence, encapsulating the conductive layer of TiN between two layers of Al_2O_3 improves the TEY in comparison with the bi-layer membrane.

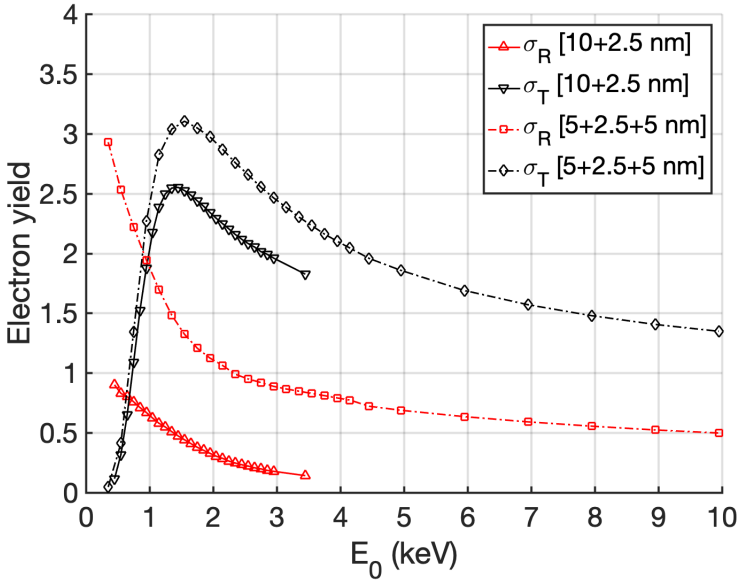

(a)

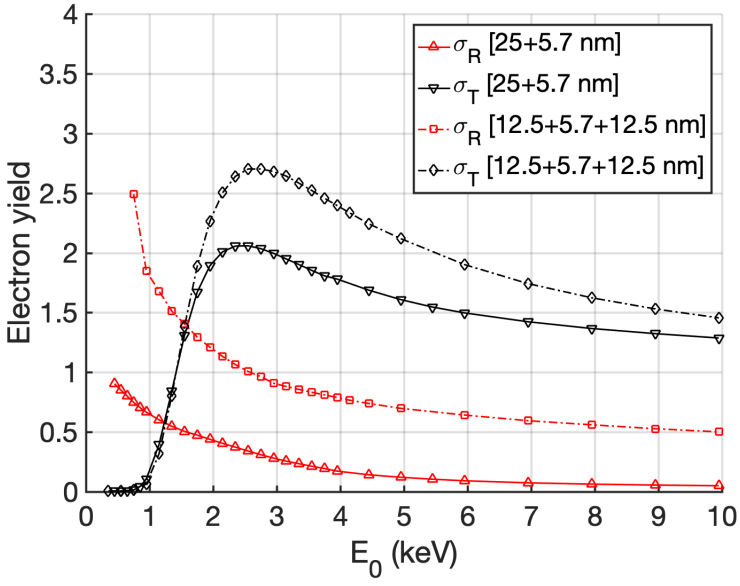

(b)

Figure 2.8: Electron emission yield curves of a bi-layer membrane compared to a tri-layer membrane Al_2O_3/TiN/Al_2O_3 with the same total effective thickness: (a) $d = 13.8$ nm (b) $d = 33.6$ nm

2.4. DISCUSSION

2.4.1. REFLECTION VS. TRANSMISSION YIELD

THE REY of a thin film can provide valuable information for the design process of tynodes. Film-on-bulk samples are less complex to manufacture, but can provide insight on the TEY if the ratio between REY and TEY is known. Furthermore, the effect of surface and/or thermal treatment on the REY can be measured on film-on-bulk samples. An estimate can then be made on how the treatment affects the TEY of tynodes.

An ideal sample would be a large freestanding symmetrical film without any obstructions on both side. Regrettably, such sample cannot be made due to the fragility of ultra-thin films. However, a method to circumvent the shortcoming of our samples is to perform an additional measurement on the bi-layer membranes and combine the results of the two separate measurements. In the first measurement, the Al_2O_3-layer is facing downwards, so emission in transmission is unobstructed. In the second measurement, the sample is flipped over so that the Al_2O_3-layer is facing upwards. By combining the TEY of the first measurement and the REY of the second, the electron emission characteristic of a flat Al_2O_3 membrane is represented. The combined yield curves are shown in figure 2.9 for the bi-layer membranes with $d = 13.8\,\text{nm}$ and $d = 33.6\,\text{nm}$. The maximum REY $\sigma_R^{\max}(E_R^{\max})$ is 3.3 (0.30 keV) and 3.7 (0.35 keV), respectively. This result is close to the maximum REY of an ALD Al_2O_3-film (12.5 nm) on bulk Si sample, which has a $\sigma_R^{\max}$ of 3.6 (0.4 keV) [4].

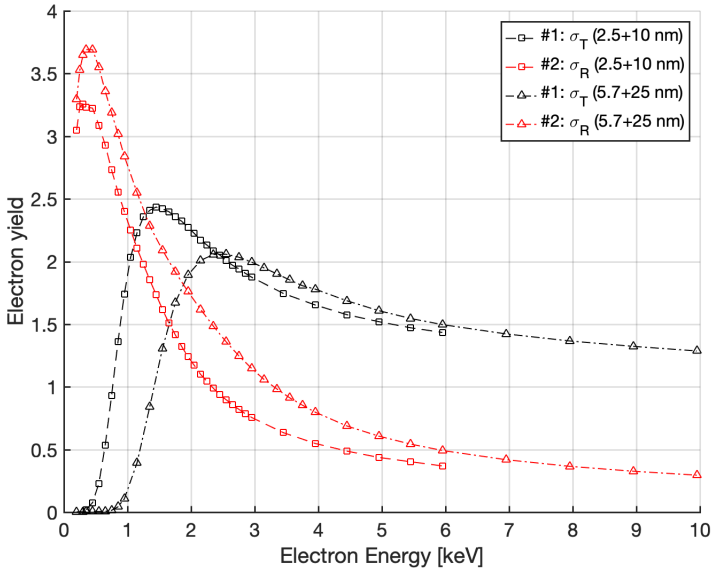

Figure 2.9: The combined results obtained from two separate measurements on the same bi-layer sample. In the first measurement, the flat surface is facing downwards to obtain σ_T. In the second measurement, the flat surface is facing upwards to obtain σ_R. The combined results portray the electron emission characteristic of a flat Al_2O_3 membrane with a thickness of 13.8 nm and one with 33.6 nm.

When comparing the REY curves in figure 2.9, the curve of the thinner film with $d = 13.8\,\text{nm}$ is lower for all energies compared to the film with $d = 33.6\,\text{nm}$. The RSEY comprises of SEs generated by forward-moving PEs δ_p and back-scattered (primary) electrons δ_b: $\delta_R = \delta_p + \delta_b$ [9]. In bulk samples (and thick films), a large contribution to RSE generation comes from BSEs that dissipate energy when they return from the interior. In an experiment, where an aluminum target was irradiated with keV-electrons, the back-scattered electrons contributed close to 40% of the generated RSEs [33]. Also, backscattered electrons were found to be 4.9 times as effective in generating SEs compared to incoming PEs. In thin films, the backscatter contribution δ_b is negligible when $R(E_0) \gg d$, since most PEs will be transmitted through the film. The lower REY of the thinner film can be attributed to the reduced backscatter contribution δ_b. A similar graph was found for thin Al films and Al bulk material by Kanter [33]. As such, the thickness $d = 13.8\,\text{nm}$ is near the optimal thickness for Al_2O_3 films. Reducing the thickness further, the REY will decrease and in ratio also the TEY.

2.4.2. TRANSMITTED FRACTION

The FSE coefficient η_T is defined as the ratio between the number of initial and transmitted PEs. In early experiments, this ratio is often referred as the transmitted fraction and is used to obtain electron-range relations, such as equation (2.1) [8]. The transmission characteristic of PEs passing through thick films is material-dependent and well-defined. It can be represented by a universal transmission curve [37] or a (constant) transmission parameter [8]. However, for ultra-thin films the transmission characteristics deviate.

In figure 2.10a, the transmitted fraction of the bi-layer films with different thicknesses is shown. A correction term of 0.2 has been applied to $\eta_T(E_0)$ to account for tertiary currents in the semi-spherical collector (see appendix B). In figure 2.10b, the transmitted fraction is plotted against the reduced initial energy E_0/E_c. This normalization was proposed by Kanter to define the transmission characteristics of electrons through foils of various materials with different thicknesses [37]. According to Kanter, the transmission curve approaches a (material-dependent) universal transmission curve for large film thickness ($d_c \geq 20\,\mu\text{g/cm}^2$). However, for thinner films the curve deviated as was shown for carbon foils. The same deviation is also observed in figure 2.10b for the films with $d = 13.8\,\text{nm}$ and $d = 33.6\,\text{nm}$, while the curve of the thicker film seems to converge towards a universal curve. For ALD Al_2O_3 with a density of $3.1\,\text{g/cm}^3$, a universal curve is expected to be found for a film thickness of $d_c \geq 64.5\,\text{nm}$. This is in agreement with the results of Kanter.

A different normalization was proposed by Fitting [8] in which the transmitted fraction is expressed as a function of the reduced film thickness d/R as shown in figure 2.11. The transmitted fraction can then be expressed by:

$$\eta_T(E_0) = \exp\left[-4.605\left(\frac{d}{R(E_0,Z)}\right)^{p(E_0,Z)}\right] \tag{2.11}$$

with E_0 the PE energy, d the film thickness, R the range and p the transmission parameter. The transmission curves normalized this way can be characterized by the transmission parameter p. In figure 2.11, the transmission curves with different p-values are plot-

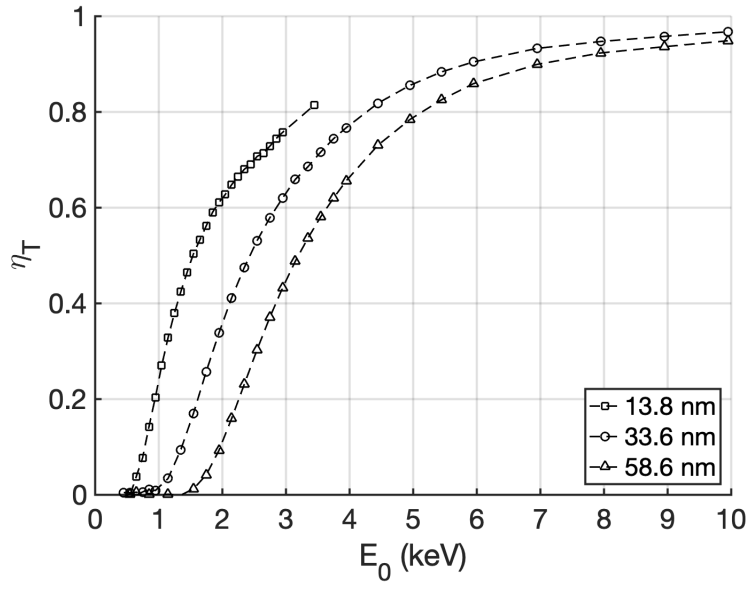

(a)

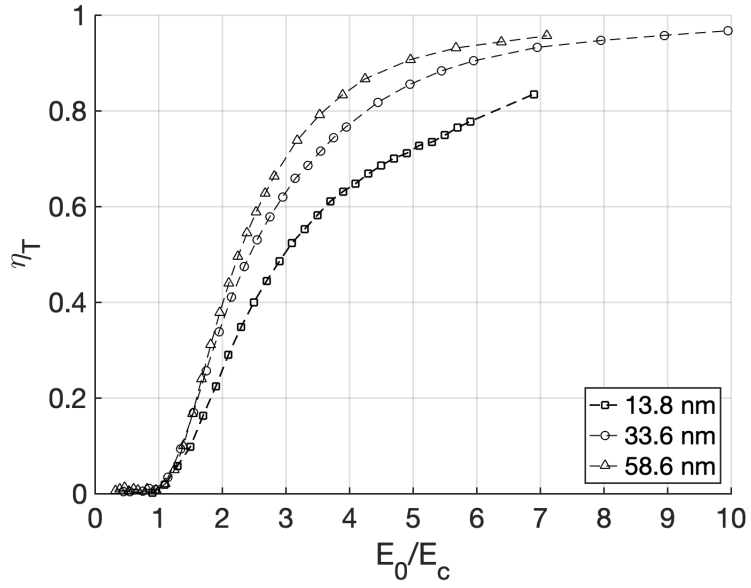

(b)

Figure 2.10: Transmitted fraction as a function of (a) the PE energy, (b) the reduced inital energy E_0/E_c.

ted using eq. (2.11). Lighter elements have a transmission characteristic similar to the curve with $p \approx 2$, while heavier elements have curves with $p \approx 1.5$. The p-value is constant over a wide range of energy E_0 for heavier elements, but depends on E_0 for lighter elements. For aluminum and alumina, it is fairly constant and $p \approx 1.9$ for $E_0 = 2\,\text{keV}$ to $10\,\text{keV}$.

In figure 2.11, the transmission parameter is determined by superimposing curves calculated with eq. (2.11) onto the normalized measurement data. The reduced film thickness d/R is determined for each film thickness d by using eq. (2.1) to calculate the range R for each E_0. The thicker film with $d = 58.6\,\text{nm}$ has a transmission characteristic as predicted by eq. (2.11) for alumina with $p \approx 1.8$, while the p-value and characteristics deviates for the thinner films. For the films with $d = 13.8\,\text{nm}$ and $d = 33.6\,\text{nm}$, the transmission parameters are $p \approx 1.3$ and $p \approx 1.5$, which resembles the transmission characteristics of PEs passing through gold and silver foils, respectively.

Hence, the transmission characteristic of ultra-thin films depends on the film thickness. One of our goal is to optimize the film thickness, so that the tynodes can perform optimally for sub-2 keV electrons. For this energy range, the transmission parameter $p(E_0, Z)$ is energy-dependent for alumina [8]. As we have shown, the transmission parameter is lower for the thinner films in comparison, which indicates that a relatively larger fraction of PEs are absorbed within the film. This is beneficial to (transmission) SEE since more energy is transferred and might be one of the contributing factors to the high TEY of the thinnest membrane.

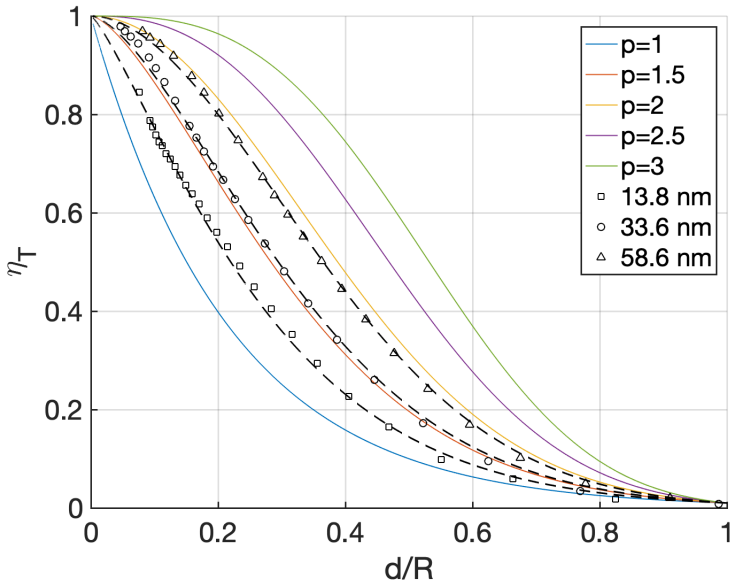

Figure 2.11: The reduced thickness d/R of the membranes. The p-value for the three film thicknesses are 1.25, 1.55 and 1.88, respectively.

2.4.3. TRANSMISSION SECONDARY ELECTRON YIELD

The TSEY of thin films depends on its thickness. In figure 2.12a, the TSEY curves for the bi-layer films are combined in one graph. Obviously, the film thickness determines the threshold energy E_{th} at which the first TSE are observed and the maximum energy E_0^{max} at which the maximum TSEY is achieved. The width of the peak is narrower for the thinnest film and broadens for increasing thicknesses. Also, the maximum TSEY decreases as the film thickness increases. As discussed in 2.4.1, the film with $d = 13.8\,\text{nm}$ is near the optimal thickness. When the film thickness is further reduced, the interaction volume for the PEs will decrease and less SEs will be generated.

The differences in the magnitude of the TSEY curve is solely due to the energy transfer process from PEs to the film. In the three-step model, the transport and escape mechanisms for internal SEs is the same for the films with different thicknesses. They consist of the same material and have the same surface condition. As such, the TSEY is proportional to the energy transfer near the exit surface of the films. The energy transfer profile $dE/dx(x, E_0)$ of an electron in bulk material can be determined by using this method; the energy transfer at depth x is 'probed' by measuring the TSEY of a film with thickness $d = x$. By combining the results of multiple films with increasing thicknesses, the energy transfer profile in a solid can be obtained [38].

In our case the film thickness is fixed, while the electron energy E_0 increases. The TSEY curve in this case is 'probing' the increasing interaction volume of the PEs as the energy is increased. For simplicity, if we assume that the interaction volume is spherical or ellipsoidal and only grows in size for increasing energy E_0, then for E_{th} the interaction volume will be a sphere (or ellipsoid) with a diameter equal to the film thickness. For E_0^{max}, the interaction volume will coincide with an interaction volume that is a half of a sphere with a diameter twice the film thickness. Using this simplified model, the width of the TSEY curves in figure 2.12a coincides with the growth of the energy transfer profile as a function the electron energy E_0. The width of the TSEY curve is proportional to the film thickness.

In figure 2.12b, a normalization is applied to both the TSEY $\delta_T/\delta_T^{\text{max}}$ and the energy E_0/E_0^{max}. After normalization, the TSEY curves show remarkable resemblance. A similar result was found for carbon foils by Hölzl & Jacobi [34]. There is a clear correlation between the threshold energy E_{th} and the maximum energy E_0^{max}. By using the latter as the normalization constant, the normalized TSEY curve no longer depends on the film thickness.

In figure 2.13, the reduced TSEY $\delta_T/\delta_T^{\text{max}}$ is plotted against the transmitted fraction η_T, since they are strongly correlated. The max TSEY coincides with a transmitted fraction of approximately 0.4 to 0.5. As such, when PEs with the optimal energy E_0^{max} is used to target the film, half of the initial PEs are either reflected or transmitted. Transmitted electrons still carry a considerable amount of energy: $E_x(x = R) \approx (0.3 \text{ to } 0.4)\ E_0$ [39], which can induce tertiary currents and/or feedback signals in detectors such as the TiPC. They should therefore not be neglected in the detector design.

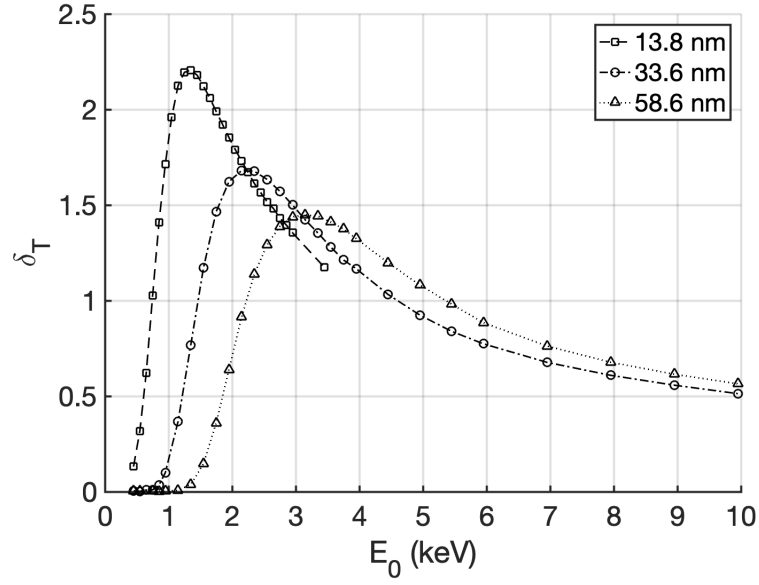

(a)

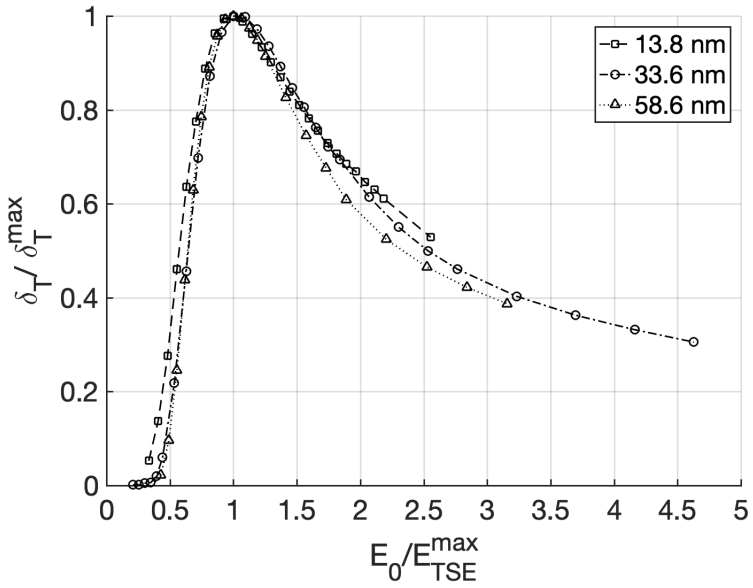

(b)

Figure 2.12: (a) TSEY (b) Normalized TSEY curve

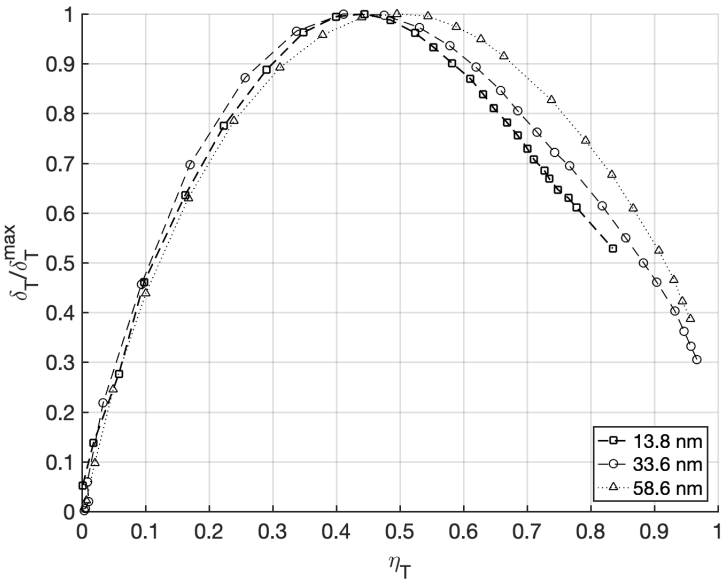

Figure 2.13: Normalized yield vs. transmitted fraction

2.5. CONCLUSIONS & OUTLOOK

We have successfully constructed multilayered Al_2O_3/TiN membranes that can be used as tynodes in photodetectors. Two types of films have been made, a bilayer TiN/Al_2O_3 and a tri-layer Al_2O_3/TiN/Al_2O_3. The tri-layer film has the conductive TiN encapsulated in order to improve the reliability of the manufacturing process. The TiN layer provides in-plane conductivity to sustain prolonged electron emission and to prevent charge-up. The highest TEY was achieved for the thinnest tri-layer film, which has a TEY of 3.1 (1.55 keV) for a film with a thickness of 13.8 nm. The requirements for the tynodes in TiPC is a TEY of 4 or higher for sub-2 keV electrons.

The results so far are promising and the tri-layer membrane design provides a solid foundation for future work. First, the tri-layer membrane samples presented in this work will be used to build a multi-stack prototype TiPC. In a recent publication, the electron emission from one tynode similar to the ones presented in this paper was measured in a dedicated vacuum setup using a TimePix chip as readout [40].

Second, the transmission yield of the tri-layer membrane can be improved by applying surface treatment, such as caesiation or hydrogen-termination. For this purpose, film-on-bulk samples can be used to measure the effect of termination on the reflection yield. However, a dedicated UHV system is required to prevent surface contamination.

Third, new materials can be considered as substitute for ALD Al_2O_3. The fabrication process presented in this work can be easily adapted for new materials, such as ALD MgO, which is a promising candidate. The first experiments on film-on-bulk samples have shown a higher reflection yield compared to Al_2O_3 [41].

Lastly, the active surface area of tynodes can be increased by forming a corrugated membrane of ALD Al_2O_3/TiN/Al_2O_3 film. The corrugated film has enhanced mechanical strength, which allows it to span over a larger surface area. This will improve the collection efficiency of the Timed Photon Counter.

REFERENCES

[1] H. Chan, V. Prodanović, A. Theulings, C. Hagen, P. Sarro, and H. Graaf, "Secondary electron emission from multi-layered TiN/Al_2O_3 transmission dynodes," *Journal of Instrumentation*, vol. 16, p. P07024, 7 2021.

[2] T. Hakamata, Ed., *Photomultiplier tubes*, 3rd ed. Hamamatsu Photonics K.K., 2007.

[3] S. Donati and T. Tambosso, "Single-Photon Detectors: From Traditional PMT to Solid-State SPAD-Based Technology," *IEEE Journal of Selected Topics in Quantum Electronics*, vol. 20, pp. 204–211, 11 2014.

[4] H. van der Graaf, H. Akhtar, N. Budko, H. W. Chan, C. W. Hagen, C. C. Hansson *et al.*, "The Tynode: A new vacuum electron multiplier," *Nuclear Instruments and Methods in Physics Research Section A: Accelerators, Spectrometers, Detectors and Associated Equipment*, vol. 847, pp. 148–161, 3 2017.

[5] H. Bruining, *Physics and Applications of Secondary Electron Emission*, 1st ed. McGraw-Hill Book Company, 1954.

[6] A. Dekker, *Secondary Electron Emission*, 1958, vol. Volume 6, pp. 251–311.

[7] J. E. Yater and A. Shih, "Secondary electron emission characteristics of single-crystal and polycrystalline diamond," *Journal of Applied Physics*, vol. 87, pp. 8103–8112, 6 2000.

[8] H.-J. Fitting, "Transmission, energy distribution, and SE excitation of fast electrons in thin solid films," *Physica Status Solidi (a)*, vol. 26, pp. 525–535, 12 1974.

[9] K. Kanaya and H. Kawakatsu, "Secondary electron emission due to primary and backscattered electrons," *Journal of Physics D: Applied Physics*, vol. 5, p. 330, 9 1972.

[10] F. A. Lukiyanov, E. I. Rau, and R. A. Sennov, "Depth range of primary electrons, electron beam broadening, and spatial resolution in electron-beam studies," *Bulletin of the Russian Academy of Sciences: Physics*, vol. 73, pp. 441–449, 4 2009.

[11] H.-J. Fitting, N. Cornet, R. Salh, C. Guerret-Piécourt, D. Goeuriot, and A. von Czarnowski, "Electron beam excitation in thin layered samples," *Journal of Electron Spectroscopy and Related Phenomena*, vol. 159, pp. 46–52, 6 2007.

[12] N. R. Whetten, "Cleavage in High Vacuums of Alkali Halide Single Crystals—Secondary Electron Emission," *Journal of Applied Physics*, vol. 35, pp. 3279–3282, 11 1964.

[13] A. Chvyreva and A. J. M. Pemen, "Experimental investigation of electron emission from dielectric surfaces due to primary electron beam: a review," *IEEE Transactions on Dielectrics and Electrical Insulation*, vol. 21, pp. 2274–2282, 10 2014.

[14] K. Handel, A. Jensen, and M. Siedband, "A two electron gun technique for the measurement of secondary emission characteristics of a variety of materials," *IEEE Transactions on Electron Devices*, vol. ED-13, pp. 525–528, 6 1966.

[15] N. Balcon, D. Payan, M. Belhaj, T. Tondu, and V. Inguimbert, "Secondary Electron Emission on Space Materials: Evaluation of the Total Secondary Electron Yield From Surface Potential Measurements," *IEEE Transactions on Plasma Science*, vol. 40, pp. 282–290, 2 2012.

[16] V. Prodanović, H. W. Chan, H. van der Graaf, and P. M. Sarro, "Ultra-thin alumina and silicon nitride MEMS fabricated membranes for the electron multiplication," *Nanotechnology*, vol. 29, p. 155703, 4 2018.

[17] A. E. Vladar, J. Michael T. Postek, and R. Vane, "Active monitoring and control of electron-beam-induced contamination," N. T. Sullivan, Ed., vol. 4344, 8 2001, p. 835.

[18] E. J. Sternglass, "High-Speed Electron Multiplication by Transmission Secondary Electron Emission," *Review of Scientific Instruments*, vol. 26, pp. 1202–1202, 12 1955.

[19] E. J. Sternglass and M. M. Wachtel, "Transmission Secondary Electron Multiplication for High-Speed Pulse Counting," *IRE Transactions on Nuclear Science*, vol. 3, pp. 29–32, 11 1956.

[20] W. W. Sapp and E. J. Sternglass, "Planar Dynode Multipliers for High-Speed Counting," *IEEE Transactions on Nuclear Science*, vol. 11, pp. 108–113, 1964.

[21] J. Llacer and E. L. Garwin, "Electron-Phonon Interaction in Alkali Halides. II. Transmission Secondary Emission from Alkali Halides," *Journal of Applied Physics*, vol. 40, pp. 2776–2792, 6 1969.

[22] M. Hagino, S. Yoshizaki, M. Kinoshita, and R. Nishida, *Caesium Activated CsI Transmission-type Secondary Emission Dynode*, 1972, pp. 469–482.

[23] R. U. Martinelli, "Reflection and transmission secondary emission from silicon," *Applied Physics Letters*, vol. 17, pp. 313–314, 10 1970.

[24] J. Yater, A. Shih, J. Butler, and P. Pehrsson, "Electron transmission studies of diamond films," *Applied Surface Science*, vol. 191, pp. 52–60, 5 2002.

[25] J. E. Yater, A. Shih, J. E. Butler, and P. E. Pehrsson, "Transmission of low-energy electrons in boron-doped nanocrystalline diamond films," *Journal of Applied Physics*, vol. 93, pp. 3082–3089, 3 2003.

[26] J. E. Yater, A. Shih, J. E. Butler, and P. E. Pehrsson, "Electron transport mechanisms in thin boron-doped diamond films," *Journal of Applied Physics*, vol. 96, pp. 446–453, 7 2004.

[27] J. Yater, J. Shaw, K. Jensen, T. Feygelson, R. Myers, B. Pate *et al.*, "Secondary electron amplification using single-crystal CVD diamond film," *Diamond and Related Materials*, vol. 20, pp. 798–802, 5 2011.

[28] S. X. Tao, H. W. Chan, and H. van der Graaf, "Secondary Electron Emission Materials for Transmission Dynodes in Novel Photomultipliers: A Review," *Materials*, vol. 9, p. 1017, 12 2016.

[29] V. Prodanović, H. Chan, J. Smedley, A. Theulings, S. Tao, H. Graaf *et al.*, "Optimization of Silicon-rich Silicon Nitride Films for Electron Multiplication in Timed Photon Counters," *Procedia Engineering*, vol. 120, pp. 1111–1114, 2015.

[30] S. Logothetidis, E. I. Meletis, G. Stergioudis, and A. A. Adjaottor, "Room temperature oxidation behavior of TiN thin films," *Thin Solid Films*, vol. 338, pp. 304–313, 1999.

[31] D. M. Taylor and Q. H. Mehdi, "Electron-beam-induced conduction in SiO_2 thin films," *Journal of Physics D: Applied Physics*, vol. 12, pp. 2253–2267, 12 1979.

[32] J. Lee, T. Jeong, S. Yu, S. Jin, J. Heo, W. Yi *et al.*, "Thickness effect on secondary electron emission of MgO layers," *Applied Surface Science*, vol. 174, pp. 62–69, 4 2001.

[33] H. Kanter, "Contribution of backscattered electrons to secondary electron formation," *Physical Review*, vol. 121, pp. 681–684, 2 1961.

[34] J. Hölzl and K. Jacobi, "Sekundärelektronen-ausbeute an dünnen kohlenstoffolien in transmission und reflexion," *Surface Science*, vol. 14, pp. 351–360, 4 1969.

[35] P. He, H. C. Hseuh, R. Todd, B. Henrist, N. Hilleret, F. L. Pimpec *et al.*, "Secondary Electron Emission Measurements for Tin Coating on the Stainless Steel of Sns Accumulator Ring Vacuum Chamber." JACoW Publishing, 2004, pp. 5–8.

[36] D. Wang, Y. He, and W. Cui, "Secondary electron emission characteristics of TiN coatings produced by RF magnetron sputtering," *Journal of Applied Physics*, vol. 124, 8 2018.

[37] H. Kanter, "Electron Scattering by Thin Foils for Energies Below 10 keV," *Physical Review*, vol. 121, pp. 461–471, 1 1961.

[38] H.-J. Fitting, H. Glaefeke, and W. Wild, "Electron penetration and energy transfer in solid targets," *Physica Status Solidi (a)*, vol. 43, pp. 185–190, 9 1977.

[39] H.-J. Fitting, "Six laws of low-energy electron scattering in solids," *Journal of Electron Spectroscopy and Related Phenomena*, vol. 136, pp. 265–272, 6 2004.

[40] T. van der Reep, B. Looman, H. Chan, C. Hagen, and H. van der Graaf, "Measurement of the transmission secondary electron yield of nanometer-thick films in a prototype Timed Photon Counter," *Journal of Instrumentation*, vol. 15, pp. P10 022–P10 022, 10 2020.

[41] V. Prodanović, H. W. Chan, A. U. Mane, J. W. Elam, M. M. Minjauw, C. Detavernier *et al.*, "Effect of thermal annealing and chemical treatments on secondary electron emission properties of atomic layer deposited MgO," *Journal of Vacuum Science & Technology A: Vacuum, Surfaces, and Films*, vol. 36, p. 06A102, 11 2018.

APPENDIX A: SAMPLE GEOMETRY CORRECTION

The reduction in yield due to reabsorption by the walls of the window frame is estimated by comparing two measurements on a p-type Si membrane with a thickness of 39 nm. The width, height and aspect ratio of the window is the same as the other samples presented in this paper. The emission surface of the Si membrane is identical on both side, so the reduction in yield is only due the window frame, which obstruct electron emission on one side.

In figure 2.14a, the REY and TEY curves of two separate measurements are given. The first measurement, with the window frame facing upwards, shows a reduction in REY, while the TEY is unaffected. In the second measurement, the window frame is facing

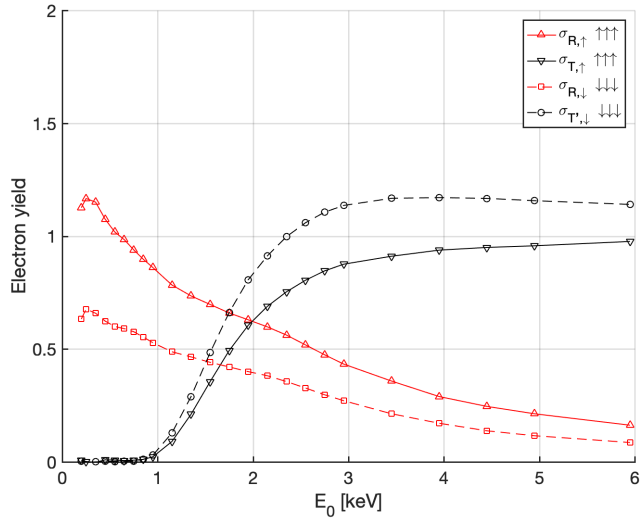

(a)

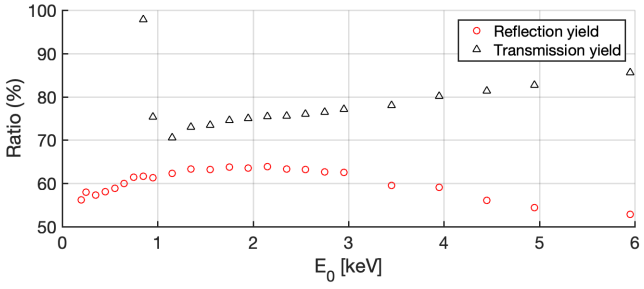

(b)

Figure 2.14: (a) The influence of reabsorption by the window opening on SEE of a Si membrane on a silicon-on-oxide (SOI) substrate. The arrows indicate the direction the flat side is facing. (b) The ratio between the obstructed and unobstructed yield for REY and TEY.

downwards and the result shows a reduction in the TEY, while the REY is unaffected. The ratio between the reduced and unaffected yields is given in figure 2.14b. Reabsorption decreases the REY by 35 to 45% and the TEY by 15 to 30%. A correction can be applied to the obtained results, but the correction factor depends on the beam energy and is only valid for these specific samples.

APPENDIX B: MEASUREMENT SETUP CORRECTION

When the measurement setup is operated with a positive sample bias, a FSE can cause tertiary currents on the retarding grid and collector. As a result, the transmitted fraction is lower than expected: it converges to 0.8, while it should converge to 1 for high energetic PEs. A correction term is therefore needed to account for the tertiary currents caused by the FSEs on the retarding grid and collector. In this appendix, we estimate the correction term by considering the scenarios in which a FSE can induce tertiary currents. For simplicity we will use the following assumptions in the model:

- Each FSE scatters only once.
- The electron emission distributions of the SEs and BSEs are uniform, hemispherical and normal to the surface.

In the first scenario, a FSE scatters on the surface of the retarding grid. It can either be scattered towards the collector, be absorbed by the grid or be backscattered towards the sample holder. In the last case, the BSE current $I_{\text{BSE,grid}}$ can be considered as a 'tertiary' current, since the FSE will be recollected by the sample holder and not be counted. In all cases, tertiary electrons (unwanted SEs) are generated that will either flow to the collector or the sample holder since both are positively biased with respect to the grid. This induces a tertiary current I_{tertiary} from the grid to the sample holder. The tertiary current from the grid to the collector can be disregarded, since it has a zero net effect on the transmitted fraction: $\eta_T(E_0) = (I_{RG+} - I_{\text{tertiary,c}}) + (I_{C+} + I_{\text{tertiary,c}})$.

In the second scenario, a FSE scatters on the wall of the collector and will either be absorbed or backscattered. Again, the BSE current $I_{\text{BSE,col}}$ is considered as a 'tertiary' current. In both cases, tertiary electrons are generated as well, but they will not be able to escape due to the positive bias of the collector and does not cause a tertiary current.

If we include the tertiary currents, then the measured transmitted fraction is given by:

$$\eta_{T,\text{meas}}(E_0) = \frac{I_T - I_{\text{BSE,grid}} - I_{\text{BSE,col}} - I_{\text{tertiary}}}{I_0} \tag{2.12a}$$

$$= \frac{I_T}{I_0} - \frac{I_{\text{BSE,grid}} + I_{\text{BSE,col}} + I_{\text{tertiary}}}{I_0} \tag{2.12b}$$

$$= \eta_{T,\text{true}}(E_0)) - \frac{I_{\text{BSE,grid}} + I_{\text{BSE,col}} + I_{\text{tertiary}}}{I_0} \tag{2.12c}$$

$$\eta_{T,\text{meas}}(E_0) = \eta_{T,\text{true}}(E_0) - \alpha(E_0) \tag{2.12d}$$

with I_T the (true) transmission current in nA, $\eta_{T,\text{true}}(E_0)$ the true transmitted fraction, $I_{\text{BSE,col}}$ the BSE current from the collector to the sample holder in nA, $I_{\text{BSE,grid}}$ the BSE

current from the grid to the sample holder in nA, I_{tertiary} the tertiary current from the grid to the sample holder in nA and $\alpha(E_0)$ a correction term.

The tertiary current from the grid is given by:

$$I_{\text{tertiary}} = I_0 \gamma \delta_{R,\text{grid}} \tag{2.13}$$

with I_0 the primary current, γ the opacity of the retarding grid mesh and $\delta_{R,\text{grid}}$ the reflection yield of the grid mesh material. The BSE current from the grid is given by:

$$I_{\text{BSE,grid}} = I_0 \gamma \varepsilon_\theta \eta_{R,\text{grid}} \tag{2.14}$$

where I_0 is the primary current, γ the opacity of the retarding grid mesh, ε_θ the backscattered angle efficiency and $\eta_{R,\text{grid}}$ the BSE yield of the retarding grid material. The BSE current from the collector is given by:

$$I_{\text{BSE,col}} = I_0 (1-\gamma)^2 \varepsilon_\theta \eta_{R,\text{col}} \tag{2.15}$$

where I_0 is the primary current, γ the opacity of the retarding grid mesh, ε_θ the backscattered angle efficiency and $\eta_{R,\text{col}}$ the BSE yield of the collector material. In this case, a BSE only counts towards the current if it passes through the retarding grid again. Otherwise, we assume that it remains trapped between the collector and grid, and will eventually be absorbed. Therefore, the probability for a BSE to pass the grid twice is given by the square of the transparency of the grid: $(1-\gamma)^2$.

The backscattered angle efficiency ε_θ is the ratio of the field of view of an electron and its emission angle distribution. The field of view of an electron on the collector wall is dome-shaped. We assumed that SEs and BSEs are emitted uniformly and hemispherically. Therefore, we can use the ratio of the surface area of a spherical cap (of a dome) to a hemisphere to find ε_θ. The surface area of a spherical cap is given by $A_{\text{cap}} = 2\pi r^2 \times (1-\cos\theta)$. The surface of this hemisphere (without its base) is given by $A_{\text{hemi}} = 2\pi r^2$. The polar angle of an electron at the bottom center of the collector is $\theta = \frac{\pi}{4}$. As a result, the backscattered angle efficiency is given by $\varepsilon_\theta = (1-\cos\theta = 0.29)$.

The correction term $\alpha(E_0)$ is given by:

$$\alpha(E_0) = \frac{I_{\text{BSE,grid}} + I_{\text{BSE,col}} + I_{\text{tertiary}}}{I_0} = \frac{I_0 \gamma \delta_{R,\text{grid}} + I_0 \gamma \varepsilon_\theta \eta_{R,\text{grid}} + I_0 (1-\gamma)^2 \varepsilon_\theta \eta_{R,\text{col}}}{I_0} \tag{2.16a}$$

$$= \gamma \delta_{R,\text{grid}} + \gamma \varepsilon_\theta \eta_{R,\text{grid}} + (1-\gamma)^2 \varepsilon_\theta \eta_{R,\text{col}} \tag{2.16b}$$

$$= 0.1 \times 1.3 + 0.1 \times 0.29 \times 0.33 + (1-0.1)^2 \times 0.29 \times 0.34 \approx 0.22 \tag{2.16c}$$

The correction term is estimated for PEs with $E_0 = 10\,\text{keV}$. The retarding grid has an opacity of 0.1 and is made of stainless steel. The RSE and BSE yield for $E_0 = 10\,\text{keV}$ are $\delta_{R,\text{grid}} = 1.3$ and $\eta_{R,\text{grid}} = 0.33$, respectively. The BSE yield of the copper collector is $\eta_{R,\text{col}} = 0.34$.

Despite the simplicity of the model, the estimated correction term $\alpha(10\,\text{keV}) \approx 0.22$ is close to the expected value. However, the correction term is energy-dependent. For low electron beam energy, the PEs will lose a large fraction of its energy before it can

transmit through the membrane. As such, they will barely induce tertiary currents and the correction term will be close to zero. On the other end, high energetic PEs will barely lose energy as they transmit through the membrane. It is likely that they will scatter multiple times within the closed collector system and induce tertiary currents on each impact. Therefore, we can assume that tertiary currents are directly proportional to the electron beam energy. As a result, we can make a rough estimation for the correction term $\alpha(E_0)$: when the electron beam energy is increased from E_c to $E_0 = 10\,\text{keV}$, the correction term increases linearly from 0 to 0.22.

3

THE CONSTRUCTION AND CHARACTERIZATION OF MGO TRANSMISSION DYNODES

In this work we demonstrate that ultra-thin (5 and 15 nm*) magnesium oxide (MgO) transmission dynodes with sufficient high (total) transmission electron yield (TEY) can be constructed. These transmission dynodes act as electron amplification stages in a novel vacuum electron multiplier: the Timed Photon Counter. The ultra-thin membranes with a diameter of* 30 µm *are arranged in a square 64-by-64-array. The TEY was determined with a scanning electron microscope using primary electrons with primary energies of 0.75 -* 5 keV*. The method allows a TEY map of the surface to be made while simultaneously imaging the surface. The TEY of individual membranes can be extracted from the TEY map. An averaged maximum TEY of* 4.6 ± 0.2 *was achieved by using* 1.35 keV *primary electrons on a TiN/MgO bi-layer membrane with a layer thickness of 2 and* 5 nm*, respectively. The TiN/MgO membrane with a layer thickness of 2 and* 15 nm*, respectively, has a maximum TEY of* 3.3 ± 0.1 *(*2.35 keV*). Furthermore, the effect of the electric field strength on transmission (secondary) electron emission was investigated by placing the emission surface of a transmission dynode in close proximity to a planar collector. By increasing the electric potential between the transmission dynode and the collector, from* -50 V *to* -100 V*, the averaged maximum TEY improved from* 4.6 ± 0.2 *to* 5.0 ± 0.3 *at a primary energy of* 1.35 keV *with an upper limit of 5.5 on one of the membranes.*

This chapter has been published in the Journal of Instrumentation **18**, 6 (2023) [1].

3.1. INTRODUCTION

VACUUM electron multipliers, such as PhotoMultiplier Tubes (PMTs), are versatile photon detectors with high gain and low noise [2]. They are essential in single photon counting applications, which can be found in, among others, high energy physics experiments and medical imaging. The operating principle of a PMT is the conversion of photons into photoelectrons and subsequent electron multiplication in vacuum. The sensitivity of the photocathode depends on the photocathode material and can be tailored to a part of the spectrum ranging from infrared to ultraviolet. An incoming (photo-)electron that impacts on the surface of a reflective dynode generates multiple secondary electrons (SEs). An intricate reflective geometry is required to ensure that the SEs are directed from dynode to dynode and eventually be collected by an anode. A disadvantage of this design is that PMTs are sensitive to external magnetic fields which can disturb the electron paths within the device. In addition, the detectors have low spatial resolution due to their bulkiness and are expensive to fabricate.

The Timed Photon Counter (TiPC) is a novel electron multiplier that utilizes tynodes for electron multiplication [3]. The mode of operation of a transmissive vacuum electron multiplier allows for a compact, planar and closely-stacked design (Figure 3.1), which outperforms traditional reflective electron multipliers, such as PMTs, in terms of temporal and spatial resolution. The electric field between the multiplication stages are stronger and more homogeneous in comparison to the electric fields in reflective geometries used in PMTs. As a result, the transit time of the SEs will be only tens of picosecond with a small spread, which results in an improved temporal resolution. An additional benefit of the stronger electric field is the reduced susceptibility to external magnetic fields that might disrupt the detector.

The core innovation in TiPC are the ultra-thin transmission dynodes. A primary electron (PE) with sufficient energy can penetrate a thin membrane. The range of a PE in bulk material is given by $R = CE_0^n$, where E_0 is the PE energy, C is a material-dependent constant and n is a constant that depends on the energy of the PE [4, 5]. In the process, the PE loses energy and generates internal SEs along its track. Internal SEs near the surface of the membrane have a chance to escape into vacuum. In the case of a thin membrane, this can either be on the side the PE entered or the opposite side, resulting in reflection and transmission SEs, respectively.

For TiPC, we aim to fabricate tynodes with a TEY of 4 or higher for 1-keV-electrons [3]. The gain G of the detector is given by $G = \sigma_T^m$, where σ_T is the TEY per tynode and m is the number of multiplication stages. A design with 5 tynodes with $\sigma_T = 4$ will have a gain of 1024, which is above the detection threshold of the TimePix pixels [6]. A tynode is characterized by its energy-yield-curve (see figure 3.2), which is determined by measuring the TEY while incrementally increasing the PE energy E_0. The yield curve $\sigma_T(E_0)$ has two features that depend on the thickness of the tynode: the critical energy E_c and the maximum TEY $\sigma_T^{\max}(E_T^{\max})$. The former is defined as the threshold where 1% of the PEs crosses the entire membrane. It coincides with the onset of the yield curve. The latter is used to express the performance of a tynode, since it contains the two benchmarks that concerns TiPC: the maximum TEY and PE energy.

Although one of the first working transmission dynodes were made in the 60's by Sternglass and Wachtel [8], the thickness of the transmission dynode was one of the

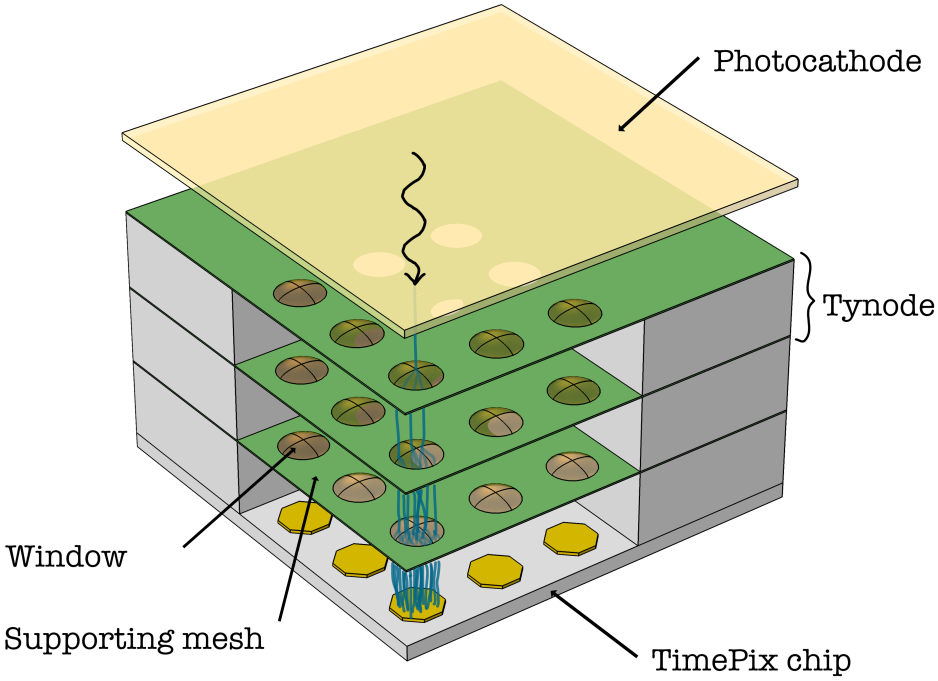

Figure 3.1: The Timed Photon Counter is a novel vacuum electron multiplier that consists of a photocathode, a transmission dynode (tynode) stack and a TimePix chip in an enclosed vacuum package [3]. The ultra-thin membranes are suspended in a supporting mesh and are spaced to align with the pixel pads of a TimePix chip. A photon that hits the photocathode is converted to a photoelectron. The photocathode is at a negative potential with respect to the first tynode. As a consequence, the photoelectron accelerates towards the first tynode and gains energy E equal to $E = q\Delta V$, where q is the charge and ΔV the potential difference. When the photoelectron impacts the top of the first tynode, multiple SEs are emitted from the bottom. Subsequently, the SEs are accelerated and gain energy before they impact the next tynode. The process repeats until the avalanche of electrons is collected by the pixel pad of the TimePix chip. For a stack with m tynodes, the gain G is $G = \sigma_T^m$, where σ_T is the (total) transmission electron yield (TEY) per tynode.

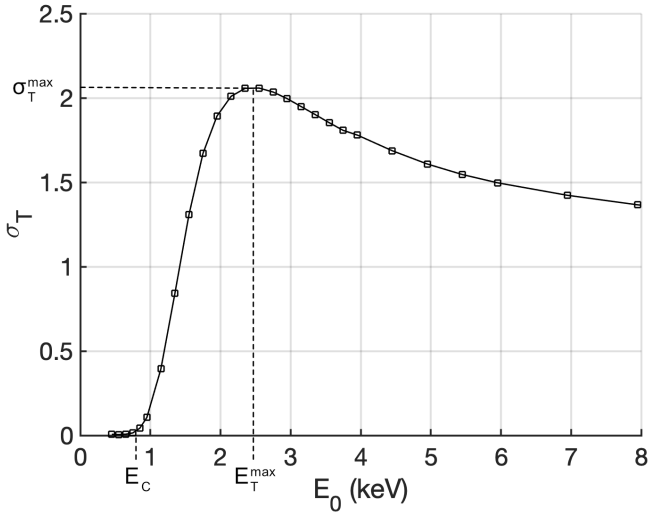

Figure 3.2: A typical TEY curve with two distinctive characteristics that depend on film thickness: the critical energy E_c and the maximum TEY $\sigma_T^{\max}(ETmax)$. The performance of a tynode is expressed by the latter. This TEY curve was determined for a TiN/Al_2O_3 membrane with layer thicknesses of 5.7/25 nm (see chapter 2 [7]).

limiting factors for wider application. In their case, the optimum film thicknesses for a KCl/Au/SiO2 film was found to be 60/2/10 nm respectively, which have a maximum TEY of 8.4 at 3.2 keV. A review on a variety of thin film materials has shown that high yields can be achieved for alkali halides, semiconductors and insulators, though the required PE energy is often a few to tens of keVs [9]. The thicknesses of these membranes are usually above 100 nm due to the complexity of fabricating freestanding thin films.

As part of the MEMBrane project, we aim to fabricate ultra-thin tynodes using Micro-ElectroMechanical System (MEMS) fabrication techniques. The advancement in MEMS technology allows for the creation of ultra-thin membranes. For instance, electron transparent windows with a thickness of 10 nm are used in the design of MEMS nanoreactors [10]. The silicon nitride (SiN) film was deposited by low-pressure chemical vapor deposition (LPCVD) and released by subsequent chemical and plasma etching. Using a similar process, we have constructed a tynode with LPCVD SiN membranes [11]. The ultra-thin membranes with a thickness of 40 nm and a diameter of 30 µm were arranged in a 64-by-64 array (see figure 3.1) and have a TEY of 1.6 (2.85 keV). In addition, a tynode with a different membrane material was fabricated by means of Atomic Layer Deposition (ALD). A TEY of 2.6 (1.45 keV) was measured on an ALD aluminum oxide (Al_2O_3) membrane with a thickness of 10 nm. On top of the membrane, a titanium nitride (TiN) layer with a thickness of 2 nm was sputtered, which provides lateral conductivity. In another design, the TiN layer was encapsulated between two Al_2O_3 layers, which improved the reliability of the conductive layer (see chapter 2 [7]). A TEY of 3.1 (1.55 keV) was measured on a membrane consisting of Al_2O_3/TiN/Al_2O_3 with layer thicknesses of 5/2.5/5 nm.

In pursuit of a better performing tynode, ALD MgO is being considered as mem-

brane material. The choice for MgO stems from the reported (total) reflection electron yield (REY) of crystalline MgO, which has a REY of 24.3 (1.3 keV) [12]. It performs better in comparison with Al_2O_3 (sapphire) and Al_2O_3 (lucalox), which have a maximum REY of 6.4 (0.75 keV) and 19.0 (1.3 keV), respectively [13]. More recently, we have reported the REY of ALD MgO and ALD Al_2O_3, which was deposited as thin films on bulk silicon substrates [3]. An as-deposited ALD Al_2O_3 film (12.5 nm) has a maximum REY of 3.6 (0.4 keV), whereas an as-deposited ALD MgO film (15 nm) has a maximum REY of 4.1 (0.5 keV). We have also shown that thermal and chemical treatment of the thin films can improve the REY [14]. For instance, the REY of ALD MgO film (15 nm) on bulk silicon improved from 4.1 (0.5 keV) to 5.4 (0.65 keV) by annealing the film at 700 °C. Exposure to both high temperatures and chemicals is often part of MEMS fabrication. Fortunately, these treatments seem to be beneficial for our purpose. Additional thermal and/or chemical treatments with the sole purpose to improve the TEY can be considered in the fabrication process as well.

In ref [15], we have implemented ALD MgO as membrane material in a tynode and reported preliminary TEY results. The maximum TEYs of the TiN/MgO films were 2.9 (1.35 keV), 2.4 (2.35 keV) and 2.5 (5.05 keV) for membranes with a thickness of 5, 15 and 25 nm, respectively. The thickness of the TiN layer is 1.8 - 2 nm. However, the membranes seemed to be affected by charge-up effects during the measurement, which resulted in non-smooth yield curves for the membranes with a thickness of 5 and 15 nm. Charge-up effects often suppress the secondary electron yield (SEY). The TEY curve of the membrane with a thickness of 25 nm is smooth. The TEY curve is similar to the curve reported by Arntz & van Vliet [16]. They reported a maximum TEY of 2.6 (3 keV) from a 47.5 nm self-supported MgO film.

In this work we present a new measurement method that we will use to reexamine the ALD MgO tynodes of ref [15]. The new method requires a lower electron dose, which can prevent charge-up effects that was observed before. It utilizes the imaging capability of a scanning electron microscope (SEM). During image acquisition, the transmission current is measured simultaneously, which is used to construct a TEY map. Using the matching SEM image, the TEYs of individual membranes can be extracted. The TEY of ALD MgO tynodes with membrane thickness of 5 and 15 nm will be re-evaluated using this new method. Also, the collector setup is modified: the semi-spherical grid and collector are replaced by a planar collector. The planar collector is used to investigate the effect of a strong electric field on the TEY of tynodes. A strong electric field can increase the transmission secondary electron yield, as reported by Qin et al. [17]. Increased secondary electron emission (SEE) due to electric fields just below the field emission threshold was observed. If a similar enhancement is present in a tynode stack, then the (intrinsic) TEY requirement of 4 or higher can be lowered.

We will present the fabrication process of ALD MgO tynodes in section 3.2 and the new method to reexamine them in section 3.3. In section 3.4, we will first discuss the reliability of the fabrication process and how improvements can be made. Second, we will make a comparison between the method that was used in ref [15] and the method presented in this work. Third, we will discuss the variance in TEY of individual membranes in an array of a tynode. Lastly, we will discuss the effect of an extracting field on the TEY. In section 3.5, we will give an outlook of the development of TiPC.

3.2. FABRICATION

THE fabrication process of a tynode can be divided in three parts. First, a support mesh of SiN was formed on a silicon (Si) wafer (Figure 3.3a,b). Second, the ultra-thin film and a protective sacrificial layer of silicon dioxide (SiO_2) were deposited on the mesh (Figure 3.3c,d). Third, the support mesh and ultra-thin membranes are released (Figure 3.3e-h). The fabrication process and the properties of the ALD MgO layer, such as its optical properties, elemental composition and surface morphology, can be found in ref [15, 18].

As substrate, a 4-inch p-type (5 - 10 Ω) Si wafer with a thickness of 525 ± 15 µm was used. After a standard cleaning procedure, a thermal SiO2 layer (500 nm) was grown in a wet thermal environment at 1100 °C. This layer will act as a stopping and sacrificial layer in the process. On top, a LPCVD SiN layer (500 nm) was deposited to form the support mesh (Figure 3.3a-b). A grid pattern with circular openings with a diameter of 30 µm was transferred by photolithography. The pitch between the openings is 55 µm, which matches the pixel pitch of a TimePix chip. The SiN in these openings was removed by a plasma etch using hexafluoroethane (C_2F_6).

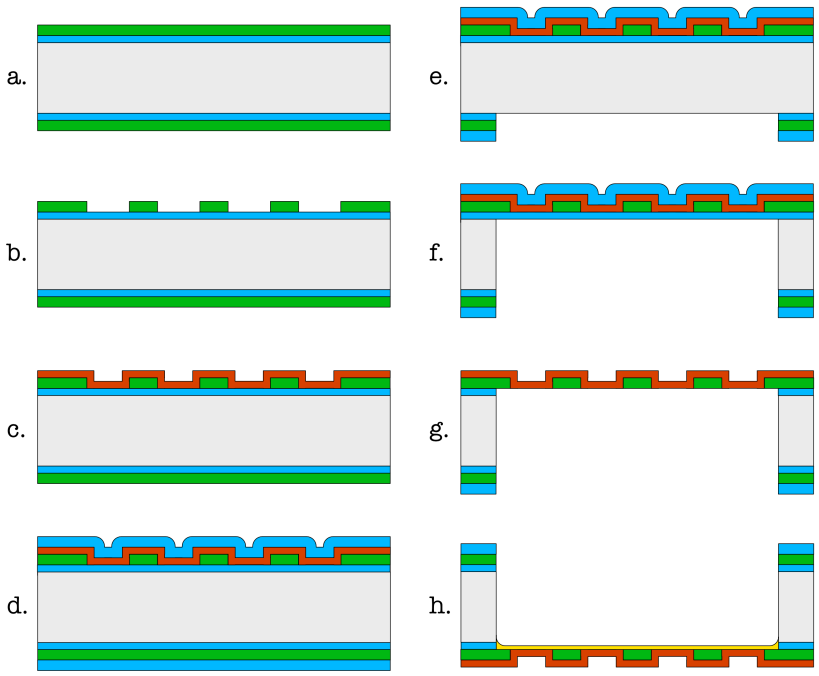

Figure 3.3: The fabrication process of a tynode: (a.) Thermal oxidation (500 nm) and LPCVD of SiN (500 nm) (b.) Lithography and plasma etch (c.) ALD of MgO (5 or 15 nm) (d.) PECVD of SiO2 on the front (1 µm) and back (3 µm) (e.) Backside lithography and plasma etch (f.) Deep-Reactive Ion Etching (DRIE) etching (g.) HF vapor etching (h.) TiN sputtering

The wafer was then transferred to a hot wall ALD reactor at 200 °C (Figure 3.3c). As precursors, $Mg(Cp)_2$ maintained at 80 °C, and deionized H_2O at room temperature was used. The gas flow of the N_2 carrier was set to 300 sccm to provide a background pressure of 1 Torr. The precursors and carrier gas were alternately pulsed for a duration of 3, 15, 1 and 15 s for $Mg(Cp)_2$, N_2, H_2O and N_2, respectively. The cycle was repeated until the desired thickness was achieved. A PECVD oxide layer (1 µm) was deposited on top of the ALD MgO layer to protect it against subsequent processing steps (Figure 3.3d). On the backside, a plasma-enhanced chemical vapor deposition (PECVD) oxide layer (3 µm) was deposited that acted as a masking layer for DRIE. A pattern of large square openings and break lines was transferred by photolithography to the backside of the wafer. First, the PECVD oxide in the openings was removed by a plasma etch (Figure 3.3e). Then, the silicon was etched by DRIE (Figure 3.3f). The wafer was then separated into individual dies. The individual dies were placed on a carrier wafer for further processing. The support grid and the ultra-thin membranes were released by etching the oxide layers in a hydrofluoric (HF) vapor chamber (Figure 3.3g) using 4 etching cycles of HF and ethanol with a flow of 190 sccm and 220 sccm, respectively, at 125 Torr. Each cycle had a duration of 10 min and the chamber was purged after each cycle with N_2. The final step was the deposition of a TiN layer (2 nm) into the opening on the backside onto the silicon support grid and the ultra-thin membranes, which provides lateral conductivity. Silver paint was applied to the silicon substrate as electrical contact points to the sample holder.

3.3. EXPERIMENTAL SETUP

THE transmission electron yield is determined by using a collector-based method within a SEM. A collector assembly is mounted on the moving stage of a Thermo Fischer NovaNanolab 650 Dual Beam SEM using a teflon holder (Figure 3.4a). The collector assembly has two electrodes, the collector and the sample holder, which are connected to two separate Keithley 2450 sourcemeters via a feedthrough into the SEM chamber. They are electrically insulated from each other using a teflon spacer and teflon screws (Figure 3.4b). The sourcemeters can apply a bias voltage to each electrode, ranging from −200 V to +200 V, while simultaneously performing a current measurement. The sample is placed on a thin sheet of Kapton (50 µm) with a square opening of 1 cm^2 in the center. It is electrically insulated from the collector, but is in contact with the sample holder via folded pressing pins. The distance between the exit surface of the tynode and the bottom electrode can be varied by using Kapton sheets with different thicknesses.

The sample holder is biased to −50 V with respect to the collector and the SEM chamber, which are both grounded. In this case, the (secondary) electrons that escape into vacuum are repelled from the sample and sample holder. In this work, we do not distinguish the fast electrons, backscattered and forward-scattered, from the slow secondary electrons. The transmission electrons are collected by the collector, while reflection electrons are absorbed by the chamber. The beam current I_0 depends on the primary energy E_0 of the beam and is measured with a Faraday cup. Before and after a measurement, the leakage and background currents in the setup are measured, which are subtracted from the collector and the sample current. The actual landing energy of the PEs is lower due to the negative bias on the sample with respect to the SEM and should be corrected by 50 eV. The electron dose of a beam on a single spot can be quite high, which can give rise

to charge-up effects and surface contamination. Therefore, a scanning electron beam is preferred to distribute the electrons over a larger surface (see chapter 2 [7]). The TEY is determined by measuring the transmission current and is given by

$$\sigma_T(E_0) = \frac{I_C}{I_0} \tag{3.1}$$

where I_C is the collector current. The total electron emission is the sum of the emissions on both sides of the membrane: $\sigma(E_0) = \sigma_R(E_0) + \sigma_T(E_0)$, and is given by

$$\sigma(E_0) = \frac{I_0 - I_S}{I_0} \tag{3.2}$$

where I_S is the sample current. The REY is then given by

$$\sigma_R(E_0) = \frac{I_0 - I_S - I_C}{I_0} \tag{3.3}$$

In this work, we present a method that allows us to determine the TEY of multiple membranes in the support grid. During the acquisition of a SEM image, the transmission current is measured as a function of time. From this current the TEY is determined using formula 3.1 and a TEY map is constructed using the same principles as for the SEM image construction. A SEM image is acquired by scanning an electron beam on the surface of the specimen. A surface area corresponding with one pixel in the image is irradiated by an electron beam for the duration of the dwell time. The line time is the required time to acquire one row of pixels plus the time needed to reposition the beam to the next

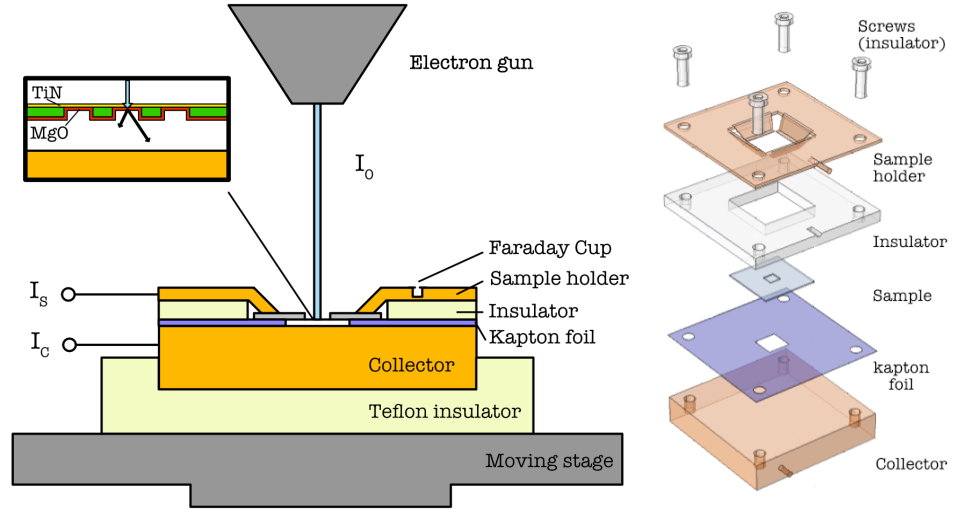

Figure 3.4: Experimental setup. (a) Schematic drawing of the collector system. (b) Exploded view of the collector assembly

row. The frame time is the acquisition time of the whole image. For this method, a set of SEM parameters is chosen that is optimized to the fastest acquisition rate of a Keithley 2450 sourcemeter, which is the limiting factor. A larger dwell time can be considered, but that would increase the electron dose. The image, with a resolution of 512 x 442, is acquired using a dwell-, line and frame time of 1 ms, 560 ms and 4.2 min, respectively. This timing information is used to divide the measured TEYs in intervals of 560 ms to obtain the rows of pixels that will be used to construct the TEY map. The sourcemeter has an acquisition rate of 333 s^{-1} or a sample time of 3.3 ms, so each row will correspond to only 168 data points. The missing pixels in the TEY map are interpolated to obtain a map with a resolution of 512 x 442. The individual membranes are identifiable on this map and the TEY of each membrane can be extracted. Likewise, the REY map can be obtained using this method.

The collector assembly with the planar collector is designed to investigate the effect of the electric field strength on the TEY. In the design of TiPC, the tynodes are separated by insulating spacers. The distance between two tynode membranes will be approximately 600 µm, which is the substrate thickness plus the height of the spacer. With a bias voltage of 1000 V, the electric field will be 1.67×10^6 V/m. In this measurement, the electric field will be in the same order of magnitude as the intended operating conditions of TiPC. The distance between the emission surface and the collector depends on the thickness of the Kapton foil, which is 50 µm. In a standard measurement, the bias voltage between the sample and collector is 50 V, which gives an electric field of 1×10^6 V/m.

3.4. RESULTS AND DISCUSSIONS

3.4.1. TYNODE FABRICATION

An image of a tynode is acquired with a SEM using an electron beam energy of E_0 = 2000 eV (Figure 3.5). The contrast in the image is due to the different materials that are present on the tynode. Also, in the case of ultra-thin membranes, the thickness plays a role in the contrast, since the PEs have sufficient energy to penetrate the membranes. As a result, a thinner membrane backscatters less PEs. The PEs generate less reflection secondary electrons (RSEs)s, which results in a darker appearance on the image. In figure 3.5, the membranes consist of a layer of MgO with a thickness of 5 nm and a layer of TiN with a thickness of 2 nm. The TiN layer was sputtered as a post-process on an uneven surface, which could lead to a less uniform deposition in comparison with a deposition on a flat wafer surface.

The ultra-thin membranes differ slightly in shape across the array (Figure 3.6). There are some that are buckled, some that have tears near their edges and others that are flat. Buckling and tearing are due to residual stress in the membrane, which can vary across the array. There are minute differences in etch and deposition rates that depend on the surface topography. For instance, the etch rate of DRIE is higher in the center of a square cavity. The silicon is removed quicker and more landing material (SiO2) is removed from the center of the cavity. As a result, the MgO membranes in the center are exposed to HF vapor for a longer duration in comparison to the membranes near the edges. Also, the deposition rate for sputtering is higher in the center of a cavity. The composition of the membranes may vary as well as their residual stress.

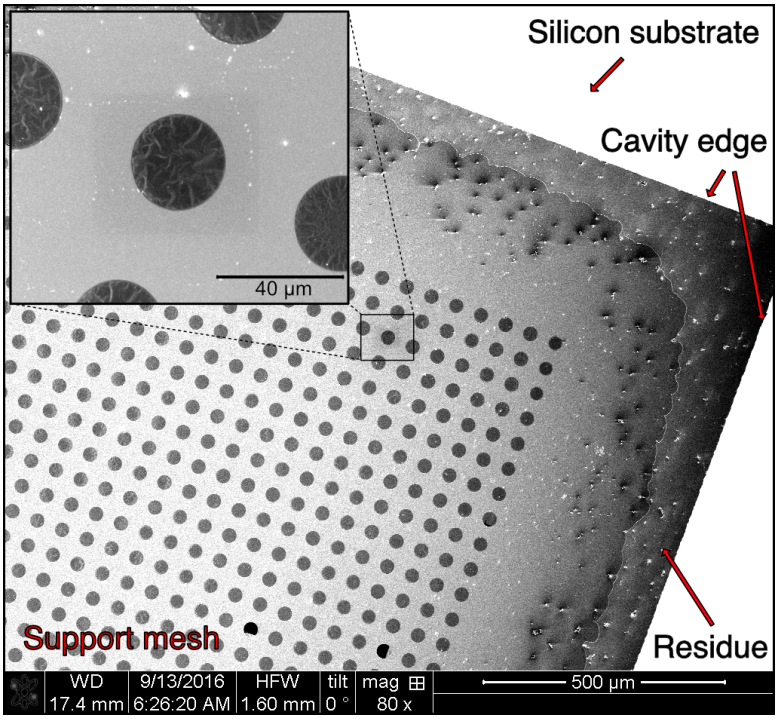

Figure 3.5: A SEM image of a tynode acquired with 2-keV-electrons using a magnification of 80x and 1200x (Overlay image). The tynode membranes have a thickness of 5 nm and a diameter of 30 µm. The SEM image depicts the backside of a tynode in which a large square cavity is etched into the silicon substrate. The cavity edge is clearly visible. The support grid in which the ultra-thin membranes are suspended is fully released. Near the side of the cavity, there are some residues, which are the remains of the sacrificial SiO2 layer. In the array, the ultra-thin membranes are also fully released. They appear to be translucent in comparison with the support grid, which is expected since 2-keV-electrons have sufficient energy to penetrate the membranes. As a result, less back-scattered and reflection secondary electrons are reemitted from the membranes.

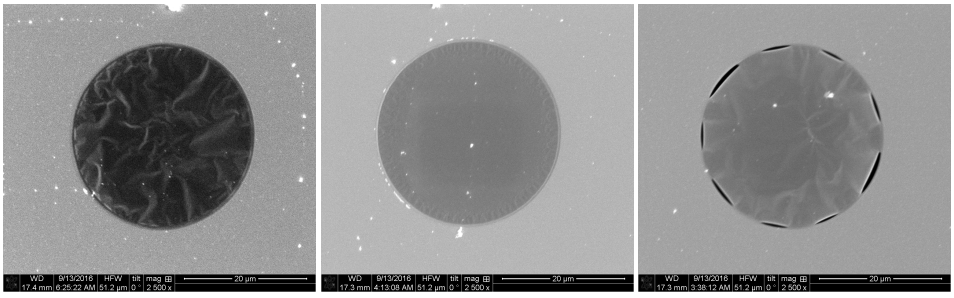

(a) (b) (c)

Figure 3.6: SEM images of various membranes on a tynode acquired with 2-keV-electrons using a magnification of 2500x. The membranes across the array differ in shape, as (a) some are buckled while (b) others are flat and (c) some shows tears near the edge. The difference in contrast is due to the SEM setting used to acquire the image and not necessarily an intrinsic difference between the membranes. Other variations are due to minute differences in etch time and conditions to which the membranes are subjected depending on their position in the array.

In a different study, the effects of HF vapor etching on ALD MgO films have been investigated using X-ray photoelectron spectroscopy (XPS) [14]. The XPS data showed that fluorine was present on the surface as well as in the bulk of thin MgO films after exposure to HF vapor. The samples were prepared by depositing thin ALD MgO films on silicon substrates. Some of the films were encapsulated with a protective oxide layer to mimic the fabrication processes involved in the present work. The samples were subsequently exposed to HF vapor for a short duration or until the oxide layers were removed. An in-depth XPS analysis of atomic content was performed by argon-ion-sputtering of the films. The results indicate that some of the oxygen atoms were exchanged for fluorine and that MgF_2/MgO compounds had formed. Moreover, the electron emission properties of the films changed. In all cases, the RSEs yields improved. It is likely that fluorine is present in the MgO membranes of tynodes.

3.4.2. SURFACE SCAN METHOD

The surface scan method has two advantages in comparison with methods that use an electron gun with a static beam. First, the SEM provides an image of the surface that allows us to determine the electron emission of multiple membranes on a tynode simultaneously. Second, the electron dose that is subjected to the surface is lower in comparison with a direct beam, which will minimize charge-up effects and/or build-up of contamination.

In figure 3.7, the surface scan method was applied to a section of a tynode. A SEM image with a resolution of 512 x 442 pixels was acquired using a magnification of 350x, a dwell time of 1 ms and a beam energy of 1.2 keV (Figure 3.7a). Simultaneously, the sample and collector currents were measured as a function of time. By splitting the currents in segments that correspond with the rows of the SEM image and placing them in order, a map that matches the SEM image was constructed (Figure 3.7b,d). From this map, the measured currents were extracted for individual membranes and their REYs and TEYs were determined using formula 3.1 and 3.3. A TEY map was drawn by dividing the collector current by the beam current, which was 0.101 nA for 1.2-keV-electrons (Figure 3.7c).

As seen in figure 3.7, one of the membranes broke off during the fabrication process. The opening contrasts sharply with its surroundings and was used as a reference point on the grid. Surprisingly, a sample current was measured on that position during a surface scan. The PEs should pass through the opening and land on the collector directly. The collector current would be equal to the beam current and a TEY of 1 was expected. However, the measured collector current was larger than the beam current. This discrepancy can be attributed to backscatter electrons from the collector surface. The backscattered electrons generate SEEs on the backside of the tynode/membranes, which will subsequently be absorbed by the collector. In this case, the measured sample current is due to this 'secondary' process. When a membrane is present, this 'secondary' process will also occur for PEs with sufficient energy to penetrate the membrane and backscatter from the collector.

As mentioned, the electron dose that is applied to the surface is lower in comparison with static beam setups. It is also lower in comparison with the previous method that we have used in ref [15]. In figure 3.8a, a consequence of a high electron dose can be

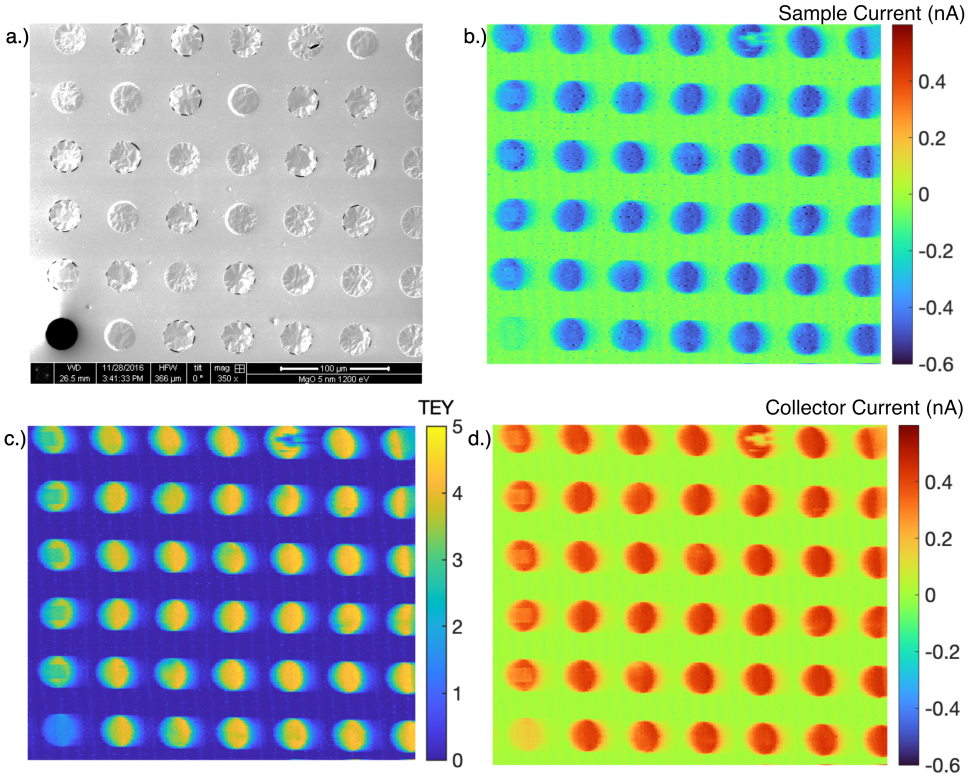

Figure 3.7: A TEY map (re)construction using the measured currents as a function of time. (a) A SEM image with a resolution of 512 x 442 pixels is acquired with a dwell time of 1 ms using 1.2-keV-electrons. (b), (d) The sample current and collector current are used to construct maps from which the emission currents of individual membranes in the array can be extracted to determine their REYs and TEYs. (c) A TEY map that is determined by using formula 3.1.

seen. The first column was subjected to a series of measurements in which the electron beam targeted single membranes. The membranes have discolorations at their centers. A rectangle is vaguely visible on the SEM image, the sample and collector current maps. The rectangle corresponds with the surface area that was imaged by the SEM using a magnification of 8000x. The electron dose to obtain one yield curve (see figure 3.8b) is approximately 9×10^{-3} C/µm^2. In comparison, using the method presented in this work, the electron dose to obtain a TEY curve (see figure 3.9b) is 1.96×10^{-4} C/µm^2, which is 46 times lower. Apparently, prolonged exposure to electron bombardment reduces the electron emission of these membranes. There are two mechanisms that can lead to a reduction in electron yield. First, when an insulator is irradiated by an electron beam, a positive charge can accumulate if there is insufficient conductivity to replenish the emitted electrons. As charge builds up, the electric field with increasing strength will retract more SEs until it reaches an equilibrium where the net yield is one. The second mechanism is the buildup of electron-beam induced currents (EBICs). Hydrocarbons on the surface of a sample that are being irradiated by an electron beam will start to form a contamination layer. The SEE properties of this contaminant differ from MgO. Of these two mechanisms, one is reversible and one is permanent. In the first case, there are mechanisms to discharge the trapped charge, whereas in the second case, once the contaminant is formed, it cannot be removed. Therefore, the electron dose that is used to inspect the samples should be kept at a minimum.

3.4.3. TRANSMISSION ELECTRON YIELD

The transmission electron yields of tynodes with two different thicknesses have been determined using the surface scan method. In figure 3.9a, a different section of the tynode with membranes with a thickness $d = 5$ nm and a diameter $\varnothing = 30$ µm is shown. This section has not been irradiated by an electron beam before the measurement. The TEYs of 20 individual membranes have been determined using the surface scan method for electron beam energies of 0.75 - 2.95 keV. Their individual TEY curves and their average (red line) are shown in figure 3.9b. An averaged maximum TEY of 4.6 was achieved with a beam energy of 1.35 keV. In figure 3.10a, a tynode with membranes with $d = 15$ nm and $\varnothing = 20$ µm is shown. The TEYs of 18 membranes have been determined for primary energies of 1.15 - 4.95 keV. The averaged maximum TEY was found to be 3.3 (2.35 keV).

The maximum TEY of the membranes with $d = 5$ nm is higher than was reported before in ref [15], which was 2.9 (1.35 keV). In figure 3.8b, the TEY curves of additional membranes on the same tynode are shown, which were determined using the same method as described in ref [15]. Each curve is obtained by repeatedly irradiating a single membrane with increasing beam energy. Overall, the maximum TEY is lower using this method compared to the surface scan method. This can be attributed to the relatively high electron beam intensity, which contaminated the surface as can be seen in figure 3.8a. Also, the irregularities in the TEY curves are indications that some charge-up effects were present. Another factor is the presence of a strong electric field near the exit surface using the new setup, which can lower the electron affinity and increase the TEY. We will discuss this in section 3.4.4.

The variance in the TEY can be attributed to two major factors: the sensitive nature of SEE, and small variations in film thickness. The first factor has been investigated ex-

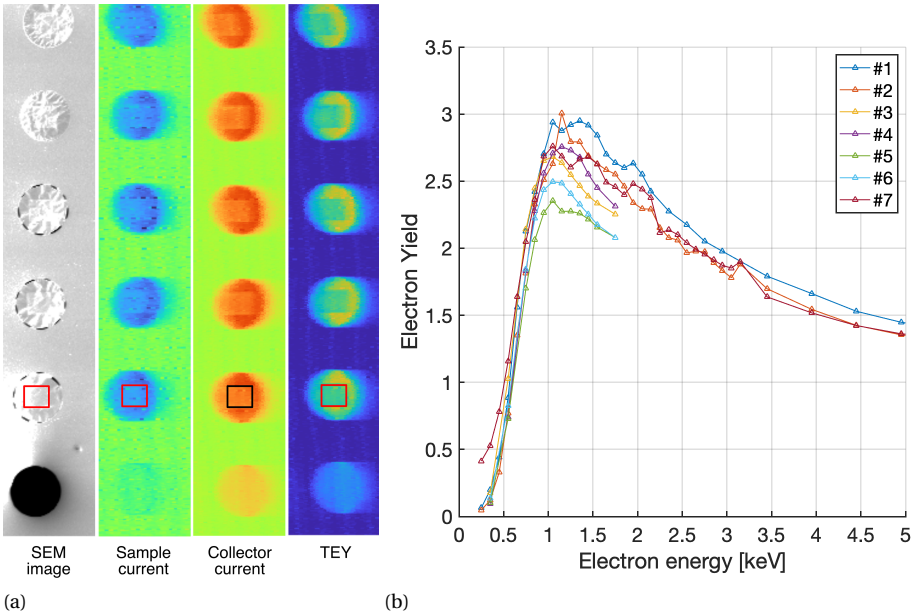

(a) (b)

Figure 3.8: The effect of prolonged electron irradiation on the TEY. (a) A close-up of the first column of the array in figure 3.7. The first column was subjected to a series of measurements using a different measurement method, which left imprints on the membranes. Individual membranes were irradiated with a scanning electron beam. The irradiated surfaces coincide with the rectangular discolorations in the centers of the membranes. The time between this series of measurement and the SEM image is 16 days, so the imprints on the membranes seem to be permanent as well as their reductions in TEYs. A more extensive description of the method can be found in chapter 2 [7]. (b) The TEY curves of 7 individual membranes that were obtained using the method described in chapter 2 [7]. The TEY curves are non-smooth, which can be due to charge accumulation or electron beam induced contamination. Both effects can change the electron emission properties of the membrane during the measurement, which result in artifacts in the TEY curves.

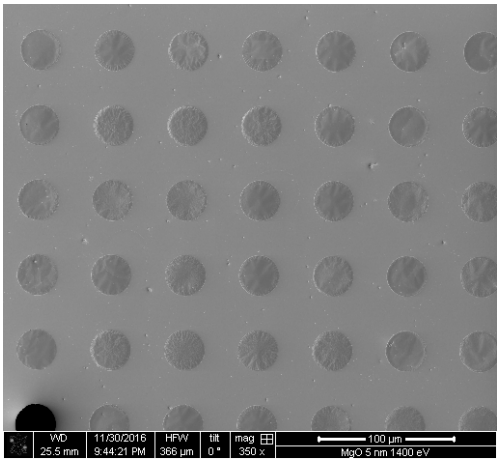

(a)

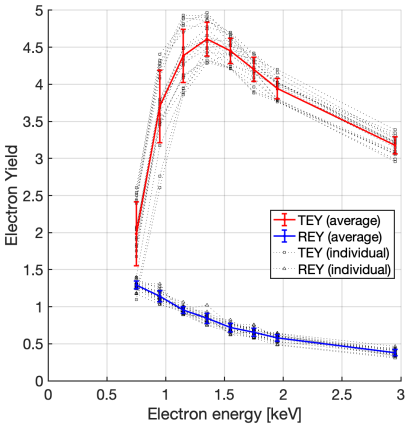

(b) $d = 5\,\text{nm}$; $\varnothing = 30\,\mu\text{m}$; $k = 20$

Figure 3.9: The averaged TEY curve of multiple membranes. (a) A SEM image of membranes with a thickness of 5 nm and a diameter of 30 µm acquired with 1.4-keV-electrons. (b) A set of $k = 20$ TEY curves is determined for individual membranes in the SEM image. The spread in TEY is the largest for low electron beam energy. The onset of the TEY curve depends on the membrane thickness, which can vary across the array due to the fabrication processes. The spread in REY is smaller, since the membrane thickness does not affect reflection SEE as much.

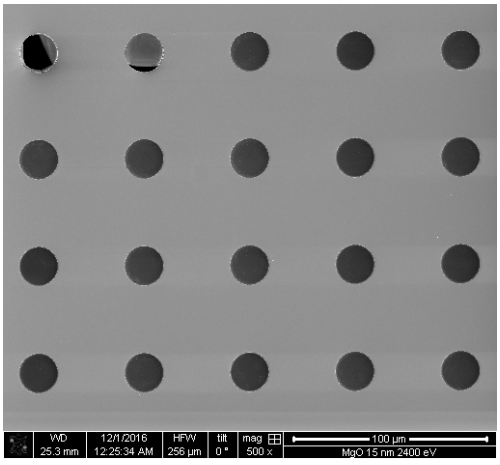

(a)

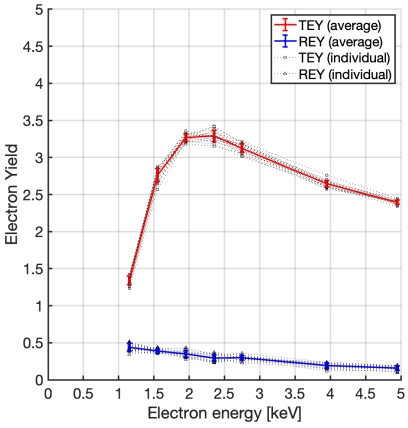

(b) $d = 15\,\text{nm}$; $\varnothing = 20\,\mu\text{m}$; $k = 18$

Figure 3.10: The averaged TEY curve of multiple membranes. (a) A SEM image of membranes with a thickness of 15 nm and a diameter of 20 µm acquired with 2.4-keV-electrons. (b) A set of $k = 18$ TEY curves is determined for the individual membranes in the SEM image. The spread in TEY of the 15 nm membranes is smaller compared to the 5 nm membranes. The small variations in the thickness due to the fabrication processes play a relatively smaller role for thicker membranes.

tensively for reflective SEE: the experimental conditions and surface termination on the material affect SEE. As such, the reported REY of many materials can vary a lot. In our case, electron induced contamination can occur when the sample is examined within the SEM. Also, the handling of the sample in ambient conditions might affect the surface condition. The second factor, the small variations in film thickness, is due to the minute differences in etch and deposition rates in the fabrication process due to surface topography. Particularly, the post-process deposition of TiN on the released membranes might result in a less uniform coverage due to the topography of the surface (figure 3.3h).

For the membranes with $d = 5\,\text{nm}$, there is a large variance in TEY between the membranes, especially for lower primary beam energies (figure 3.9b). These energies coincide with the onset of transmission (secondary) electron emission, which occurs when PEs deposit energy near the exit surface of the membrane. A small increase in the thickness would require a slightly higher PE energy to reach the exit the surface. Therefore, small variations in thickness would lead to a large variance in the TEY. For higher PE energy, the majority of the PEs will be transmitted through the membrane. Their energy loss profiles would be similar regardless of the thickness of the membrane. For the membranes with $d = 15\,\text{nm}$, the variance in TEY is much smaller (figure 3.10b). The TEY curves rise more gradually for thicker membranes. A small variation in thickness due to the TiN deposition contributes relatively less to the overall thickness of the membrane. A shift of the onset of the TEY curve will be less apparent in this case. Further, the variance in the REY is small regardless of the membrane thickness. For reflection SEE, only PE interactions at a shallow depth contribute. The energy loss profile near the surface will be similar regardless of small variations in thickness.

3.4.4. EXTRACTION FIELD-ENHANCED YIELD

The proximity of the emission surface of a tynode to the collector seems to improve the TEY. The electric field is estimated to be $2 \times 10^6\,\text{V/m}$, which can be increased by using a higher bias voltage between the sample and collector. In figure 3.11a, the bias voltage is increased to 100 and 200 V. There is a small improvement in TEY in both cases. However, the effect seems to level off. A similar effect was observed in figure 3.11b for the membrane with $d = 15\,\text{nm}$. A strong electric field near the emission surface of a tynode can have several effects on the (secondary) electron emission: Schottky barrier lowering, field-enhanced electron emission or field emission. The latter two effects require relatively large electric fields and are unlikely to occur in this experiment. Field-enhanced SEE is observed for electric field strength between $6.6 \times 10^7\,\text{V/m}$ and $2.5 \times 10^8\,\text{V/m}$; a PE is needed to initiate SE emission, but the number of SEs is significantly larger than unassisted SE emission [17]. Above $2.5 \times 10^8\,\text{V/m}$, field emission occurs at which electrons are extracted without the need of PEs. The Schottky effect is known to lower the work function of cathodes due to the presence of a strong electric field. For dielectrics, Schottky barrier lowering is given by:

$$\Delta\chi = -q\sqrt{\frac{qKF_e}{\epsilon_0}} \quad \text{with} \quad K = \frac{\epsilon_r + 1}{\epsilon_r - 1} \tag{3.4}$$

where q is the charge in C, F_e the electric field in V/m, ϵ_0 the permittivity in vacuum and ϵ_r the dielectric constant [19]. In figure 3.12, the change in the electron affinity is

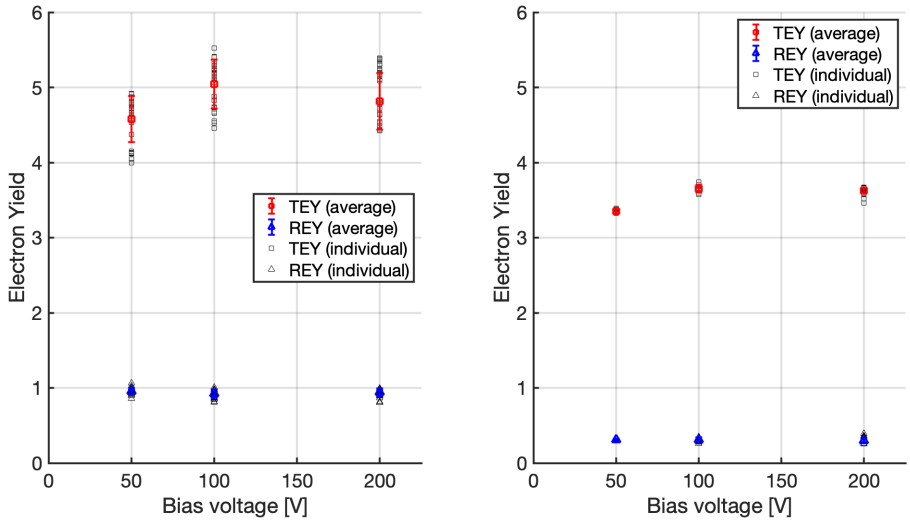

(a) $E_0 = 1.4\,\text{keV}$; $d = 5\,\text{nm}$; $\varnothing = 30\,\mu\text{m}$; $k = 25$

(b) $E_0 = 2.4\,\text{keV}$; $d = 15\,\text{nm}$; $\varnothing = 20\,\mu\text{m}$; $k = 9$

Figure 3.11: The effect of the electric field on the TEY. The electric potential between the sample and collector is increased by setting the collector potential at 0, +50 and +150 V for three subsequent measurements, while keeping the sample potential at -50 V. The averaged TEY was determined for two tynodes with $d = 5\,\text{nm}$ and $d = 15\,\text{nm}$ using their optimal PE energy E_0.

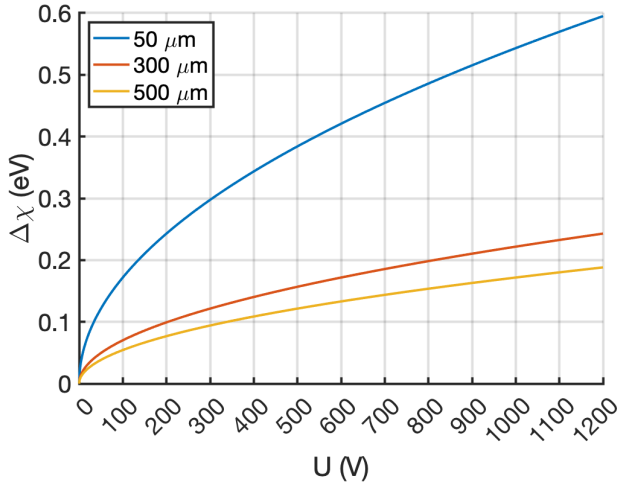

Figure 3.12: Schottky effect on dielectrics. A dielectric constant ϵ_r of 9.8 is used for MgO. In the measurement setup, the distance l between the emission surface of the tynode and the collector is 50 µm and the bias voltage is 50 - 200 V. In TiPC, the distance l between two tynodes is approximately 500 µm and the operating voltage is 1000 V. The electric field is in the same order of magnitude in both cases.

shown as a function of the bias voltage U. The electric field depends on the distance l and bias voltage: $F_e = U/l$. In this work, the gap is 50 µm between the sample and collector. In TiPC, the distance between two tynodes is approximately 500 µm, albeit operated with a higher bias voltage. The electric field in both cases is in the same order of magnitude. The effect of electron affinity lowering on SEE have been estimated by Cazaux [20]. He attributed the discrepancies in (reflection) secondary electron yield data of common materials, such as silicon and aluminum, to differences in work function or electron affinity of the samples due to oxidation and/or contamination. The relative change in the escape probability of SEs due to a change in electron affinity is given by

$$A \sim A_1(\chi/\chi_1)^{-p_{\mathrm{EA}}} \tag{3.5}$$

where A_1 is the initial escape probability, χ_1 the initial electron affinity, χ the altered electron affinity and p_{EA} a material dependent constant. An increase in the escape probability of SEs will result in a proportional increase in the SE yield. Unfortunately, p_{EA} have not been reported for magnesium oxide, so the relative change in TEY cannot be estimated and compared to our results. It does show that the escape probability of SEs increases exponentially as the electron affinity is being lowered. However, this contradicts with our results as the effect seems to level off when the bias voltage is increased from 100 to 200 V.

3.5. CONCLUSION & OUTLOOK

We have developed a new surface scan method that requires a lower electron dose, which minimizes charge-up and/or contamination effects. In addition, the method allows us to investigate multiple membranes on a tynode. We have also demonstrated that ALD MgO is a viable membrane material for tynodes. Membranes that consists of TiN/MgO layers with layer thicknesses of 2 and 5 nm, respectively, provide an averaged maximum TEY of 4.6 ± 0.2 (1.35 keV). If we limit the operating voltage between two tynodes to 1 kV, then a TEY of 3.7 is still achievable. With a TEY of 3.7, a stack of 6 tynodes would be sufficient to trigger a pixel on a TimePix chip and allow for single photon detection.

The strong electric field between the tynodes in a stack is beneficial to the TEY due to the Schottky effect, which lowers the electron affinity on the emission surface. The averaged maximum TEY improved from 4.6 ± 0.2 to 5.0 ± 0.3. In future designs, there is room to benefit more from this effect by either reducing the substrate thickness and/or applying a higher bias voltage between the tynodes. Also, an outlier with a TEY of 5.5 was measured on one individual membrane. Thus, improving the fabrication process to ideal conditions can increase the averaged maximum TEY of a tynode.

The variance in TEYs of the membranes across the array can be reduced by incorporating the TiN deposition earlier in the fabrication process rather than as a post-process at the end. In chapter 2 [7], we have demonstrated that the TiN layer can be encapsulated by two layers of ALD Al_2O_3, which were the electron emission layers in that design. The surface on which the TiN was sputtered was relatively flat, which gave a more uniform layer in comparison with a post-process deposition. As an alternative, TiN can be deposited by ALD, which is even more uniform and allows for a precise controlled depo-

sition rate. We will demonstrate that ALD TiN can be applied as the conduction layer in corrugated films in chapter 4 [21].

The aging mechanism of the MgO membranes needs to be investigated further. It is not yet clear what the mechanisms are that lower the TEY. The tynodes are exposed and kept in ambient conditions, which can change their composition over time. Also, electron-induced contamination was observed after prolonged irradiation. Literature on electron induced contamination has shown that the vacuum level determines the deposition rate of contaminants. The SEM chamber that is used for the measurements presented in this work has a vacuum level of 10^{-5} mbar, which is not ideal. The TiPC detector will be operated at ultra-high vacuum (UHV) levels (10^{-9} mbar) at which electron induced contamination is minimized.

The next step in the development of TiPC is the assemblage of a tynode stack with 5 or 6 tynodes. There are two technical challenges that need to be addressed: alignment and SE focusing. First, the arrays of each stage need to be aligned, so that an amplification 'channel' is formed above each pixel pad of a TimePix chip. Alignment grooves are proposed to self-align multiple tynodes [18]. Second, some SE focusing is required to ensure that all transmission SEs are directed to the active membrane surface of the next amplification stage. Dome-shaped tynodes have been proposed as a solution. In chapter 4 [21], we will present corrugated membranes that have a near 100% active surface. The 3D-structure of the membrane will have a focusing effect as well. The fabrication process of both designs can be adapted to replace ALD Al_2O_3 by ALD MgO.

Once the tynode stack is assembled, it can be mounted in a prototype TiPC: the TyTest setup [22]. The setup consists of an electron gun as electron source, a mount to hold a tynode (stack) and a TimePix Chip as read-out. The vacuum chamber can be modified to allow for more high voltage connections, which are needed for a multi-layer stack. Also, the chamber operates at a higher vacuum level in the order of 1×10^{-8} mbar, which can prevent contamination that was observed in this work. The setup was used as an alternative method to determine the TEY of a (single) tynode using a TimePix chip. The results were in agreement with the results obtained with a SEM-based method (see chapter 4 [21]).

REFERENCES

[1] H. Chan, V. Prodanović, A. Theulings, S. Tao, J. Smedley, C. Hagen *et al.*, "The construction and characterization of MgO transmission dynodes," *Journal of Instrumentation*, vol. 18, p. P06028, 6 2023.

[2] T. Hakamata, Ed., *Photomultiplier tubes*, 3rd ed. Hamamatsu Photonics K.K., 2007.

[3] H. van der Graaf, H. Akhtar, N. Budko, H. W. Chan, C. W. Hagen, C. C. Hansson *et al.*, "The Tynode: A new vacuum electron multiplier," *Nuclear Instruments and Methods in Physics Research Section A: Accelerators, Spectrometers, Detectors and Associated Equipment*, vol. 847, pp. 148–161, 3 2017.

[4] K. Kanaya and H. Kawakatsu, "Secondary electron emission due to primary and backscattered electrons," *Journal of Physics D: Applied Physics*, vol. 5, p. 330, 9 1972.

[5] H.-J. Fitting, "Transmission, energy distribution, and SE excitation of fast electrons in thin solid films," *Physica Status Solidi (a)*, vol. 26, pp. 525–535, 12 1974.

[6] X. Llopart, R. Ballabriga, M. Campbell, L. Tlustos, and W. Wong, "Timepix, a 65k programmable pixel readout chip for arrival time, energy and/or photon counting measurements," *Nuclear Instruments and Methods in Physics Research Section A: Accelerators, Spectrometers, Detectors and Associated Equipment*, vol. 581, pp. 485–494, 10 2007.

[7] H. Chan, V. Prodanovć, A. Theulings, C. Hagen, P. Sarro, and H. Graaf, "Secondary electron emission from multi-layered TiN/Al_2O_3 transmission dynodes," *Journal of Instrumentation*, vol. 16, p. P07024, 7 2021.

[8] E. J. Sternglass and M. M. Wachtel, "Transmission Secondary Electron Multiplication for High-Speed Pulse Counting," *IRE Transactions on Nuclear Science*, vol. 3, pp. 29–32, 11 1956.

[9] S. X. Tao, H. W. Chan, and H. van der Graaf, "Secondary Electron Emission Materials for Transmission Dynodes in Novel Photomultipliers: A Review," *Materials*, vol. 9, p. 1017, 12 2016.

[10] J. F. Creemer, S. Helveg, P. J. Kooyman, A. M. Molenbroek, H. W. Zandbergen, and P. M. Sarro, "A MEMS Reactor for Atomic-Scale Microscopy of Nanomaterials Under Industrially Relevant Conditions," *Journal of Microelectromechanical Systems*, vol. 19, pp. 254–264, 4 2010.

[11] V. Prodanović, H. W. Chan, H. van der Graaf, and P. M. Sarro, "Ultra-thin alumina and silicon nitride MEMS fabricated membranes for the electron multiplication," *Nanotechnology*, vol. 29, p. 155703, 4 2018.

[12] N. R. Whetten and A. B. Laponsky, "Secondary Electron Emission of Single Crystals of MgO," *Journal of Applied Physics*, vol. 28, pp. 515–516, 4 1957.

[13] P. H. Dawson, "Secondary Electron Emission Yields of some Ceramics," *Journal of Applied Physics*, vol. 37, pp. 3644–3645, 8 1966.

[14] V. Prodanović, H. W. Chan, A. U. Mane, J. W. Elam, M. M. Minjauw, C. Detavernier *et al.*, "Effect of thermal annealing and chemical treatments on secondary electron emission properties of atomic layer deposited MgO," *Journal of Vacuum Science & Technology A: Vacuum, Surfaces, and Films*, vol. 36, p. 06A102, 11 2018.

[15] V. Prodanović, H. W. Chan, A. U. Mane, J. W. Elam, H. van der Graaf, and P. M. Sarro, "Ultra-thin ALD MgO membranes as MEMS transmission dynodes in a timed photon counter." presented at the IEEE 30th Intern. Conf. on Micro Electro Mechanical Systems (MEMS), Las Vegas, US, jan. 2017, pp. 740–743.

[16] F. O. Arntz and K. M. V. Vliet, "Secondary Emission of Thin Self-Supported Films of MgO," *Journal of Applied Physics*, vol. 33, pp. 1563–1566, 4 1962.

[17] H. Qin, R. Tan, J. Park, H.-S. Kim, and R. H. Blick, "Direct observation of sub-threshold field emission from silicon nanomembranes," *Journal of Applied Physics*, vol. 109, p. 124504, 6 2011.

[18] V. Prodanović, "Ultra-thin MEMS fabricated tynodes for electron multiplication," Ph.D. dissertation, EEMCS, TU Delft, The Netherlands, 2019.

[19] J. Cazaux, "Some considerations on the secondary electron emission, δ, from e-irradiated insulators," *Journal of Applied Physics*, vol. 85, pp. 1137–1147, 1 1999.

[20] J. Cazaux, "Calculated effects of work function changes on the dispersion of secondary electron emission data: Application for Al and Si and related elements," *Journal of Applied Physics*, vol. 110, pp. 0–15, 7 2011.

[21] H. Chan, V. Prodanović, A. Theulings, T. ten Bruggencate, C. Hagen, P. Sarro *et al.*, "Ultra-thin corrugated metamaterial film as large-area transmission dynode," *Journal of Instrumentation*, vol. 17, p. P09027, 9 2022.

[22] T. van der Reep, B. Looman, H. Chan, C. Hagen, and H. van der Graaf, "Measurement of the transmission secondary electron yield of nanometer-thick films in a prototype Timed Photon Counter," *Journal of Instrumentation*, vol. 15, pp. P10 022–P10 022, 10 2020.

4

ULTRA-THIN CORRUGATED METAMATERIAL FILM AS LARGE-AREA TRANSMISSION DYNODE

My Origami creations, in accordance with the law of nature,
require the use of geometry, science and physics.
They also encompass religion, philosophy, and biochemistry.
Overall, I want you to discover the joy of creation by your own hand
the possibility of creation from paper is infinite.

Akira Yoshizawa

Large-area transmission dynodes (tynodes) were fabricated by depositing an ultra-thin continuous film on a silicon wafer with a 3-dimensional pattern. After removing the silicon, a corrugated membrane with enhanced mechanical properties was formed. Mechanical metamaterials, such as this corrugated membrane, are engineered to improve its strength and robustness, which allows it to span a larger surface in comparison to flat membranes while the film thickness remains constant. The ultra-thin film consists of three layers (Al_2O_3/TiN/Al_2O_3) and is deposited by Atomic Layer Deposition (ALD). The encapsulated TiN layer provides in-plane conductivity, which is needed to sustain secondary electron emission (SEE). Two types of corrugated membranes were fabricated: a hexagonal honeycomb and an octagonal pattern. The latter was designed to match the square pitch of a CMOS pixel chip. The transmission secondary electron yield (TSEY) was determined with a collector-based method using a scanning electron microscope. The highest

This chapter has been published in the Journal of Instrumentation **17**, 9 (2022) [1].

(total) transmission electron yield (TEY) was measured on a membrane with an octagonal pattern. A yield of 2.15 was achieved for 3.15 keV *incident electrons for an* $Al_2O_3/TiN/Al_2O_3$ *tri-layer film with layer thicknesses of 10/5/*15 nm. *The variation in yield across the surface of the corrugated membrane was determined by constructing a yield map. The active surface for transmission SEE is near 100%, i.e. a primary electron (PE) generates transmission secondary electrons (TSEs) regardless of the point of impact on the corrugated membrane.*

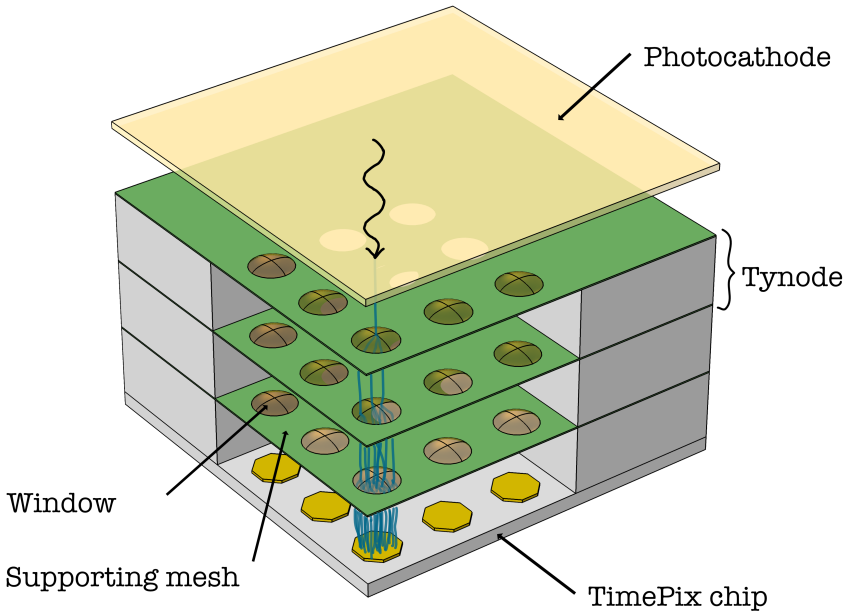

Figure 4.1: Schematic drawing of Timed Photon Counter (TiPC) with tynodes comprising ultra-thin circular membranes suspended in a supporting mesh. A photon is converted to a photoelectron at the photocathode. Due to the electric field between each stage, the photoelectron will gain sufficient energy to induce transmission SEE at each tynode. After several multiplication stages, an avalanche of electrons will be collected by the pixel pads. The active membranes are suspended in small circular windows arranged in a 64-by-64 array with a pitch of 55 µm, which matches the pixel pitch of a TimePix chip.

4.1. INTRODUCTION

THE TiPC is a novel vacuum electron multiplier that has ultra-thin transmission dynodes (tynodes) as multiplication stages [2]. The detection principle is similar to a PhotoMultiplier Tube (PMT), i.e. photoemission from a photocathode and subsequent (secondary) electron multiplication in vacuum. In a PMT, a photoelectron is multiplied within a series of (reflective) dynodes [3]. The dynodes are carefully aligned in a sequence, where the electric potential is step-wisely increased between each dynode. Under influence of the electric field, the secondary electrons (SEs) are accelerated and directed from dynode to dynode. On each impact, their number is multiplied. Eventually, the avalanche of electrons is collected by the anode, which provides an output signal.

PMTs are widely used as photodetector in low-light applications due to its high gain, low noise and large sensing area. Their spectral response can be tailored to a certain part of the spectrum, ranging from ultraviolet to near-infrared, by choosing a window material with high transparency and a photocathode material with high sensitivity to the selected region [3]. However, the design of PMTs has some drawbacks due to the complex arrangement of the (reflective) dynodes. First, the non-uniform electron paths between each dynode limit the time resolution in the order of nanoseconds. Second, the electron paths are easily perturbed by magnetic fields, which precludes PMTs to be used in applications with strong magnets. Last, the device is voluminous, fragile and expensive to manufacture.

TiPC will improve upon PMTs in terms of time and spatial resolution. The core innovation is the use of tynodes as multiplication stages and a Complementary metal-oxide semiconductor (CMOS) pixel chip as read-out. A tynode is an ultra-thin membrane that is optimized for transmission secondary electron emission (SEE). An incoming primary electron (PE) will generate multiple transmission secondary electrons (TSEs) within the membrane as the PE transmits through it. This allows tynodes to be closely stacked on top of each other. This design/configuration has many benefits. First, the electric fields between the planar tynodes are more uniform and stronger. The electron paths are more uniform, which reduces the electron transit time spread (TTS) and improves the overall time resolution. Second, the increased electric field strength makes TSEs less susceptible to external magnetic fields. Third, 2D spatial information can be acquired using a CMOS pixel chip as read out. Last, TiPC is a compact planar photodetector.

The SEE process can be divided in three steps: *generation*, *transport* and *escape* of internal SEs [4]. The first step describes the interaction of PEs within matter. PEs that enter matter will scatter and lose energy. Some of the energy is used to generate internal SEs. The second step models the transport of these internal SEs. The distance that an internal SE can travel depends on the material. Often the band gap model is used to describe the difference in transport in metal, semiconductors and dielectrics. In general, wide band gap materials allow internal SEs to travel a greater distance before they can either escape or be reabsorbed. The third step describes the escape process: internal SEs that reach the surface will encounter a barrier and need sufficient energy to cross it. The amount of energy that is needed is determined by the work function (metals) or the electron affinity (EA) (semiconductors and dielectrics) of the material.

Thus, the amplification of a tynode depends on the material of the tynode and its surface condition. The performance of a tynode is characterized by the maximum (to-

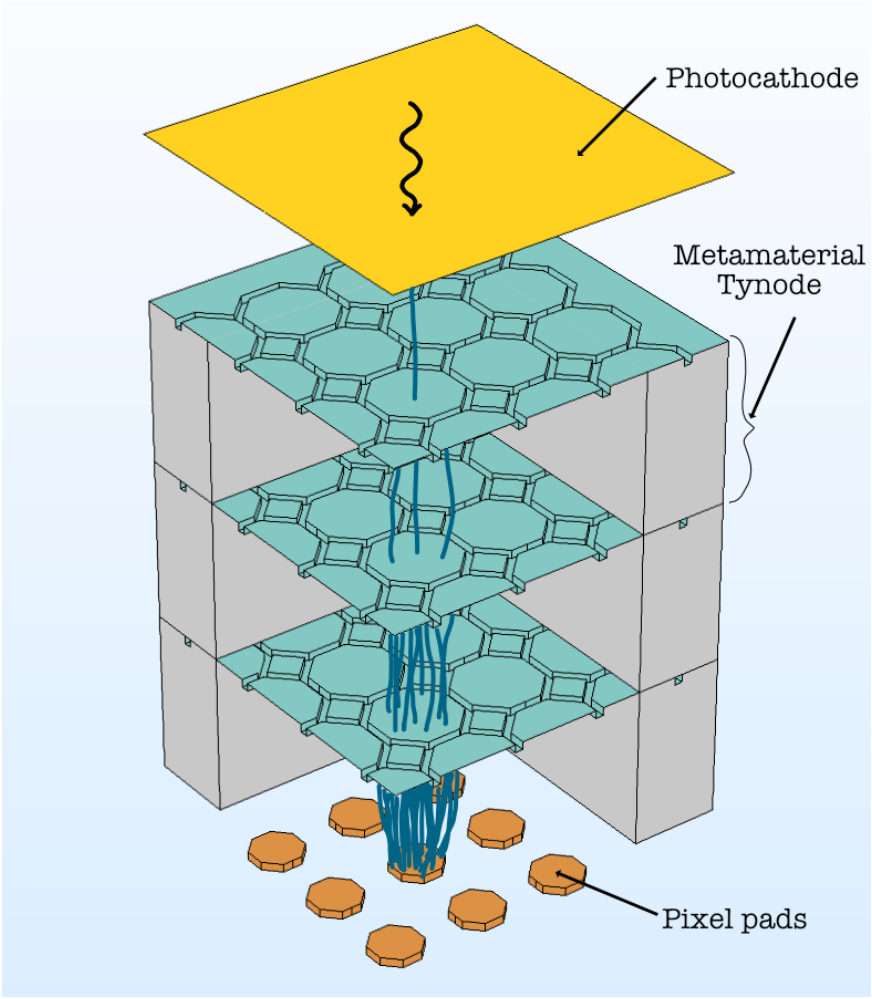

Figure 4.2: Schematic drawing of TiPC with metamaterial tynodes. The metamaterial tynode consists of an ultra-thin corrugated membrane with uniform thickness. An incoming electron with sufficient energy can generate TSEs regardless of the point of impact. However, the avalanche should be collected by the pixel pad in order for the photon/photoelectron to be detected.

tal) transmission electron yield (TEY) $\sigma_T^{\max}$ obtained with PEs with energy $E_T^{\max}$; or in a more compact notation: $\sigma_T^{\max}(E_T^{\max})$. In a detector with multiple tynodes, the maximum TEY determines the overall gain, while the required PE energy determines the operating voltage of the detector. The PE energy $E_T^{\max}$ is determined by the film thickness and the range of the electron in the film. Only SEs that are generated near the exit surface of the film have a chance to escape. Therefore, the film thickness is a parameter that needs to be optimized. In the past, several types of transmission dynodes with high TEY have been reported [5]. Unfortunately, the maximum TEY was only achieved with PEs with very high energy. For instance, a TEY of 27(9 keV) was reported for a cesium-activated CsI film deposited on an aluminum (Al)/aluminum oxide (Al_2O_3) film by Hagino et al.[6].

Hence, we used Micro-ElectroMechanical System (MEMS) technology to fabricate ultra-thin membranes, which were suspended within a supporting mesh with circular windows with a diameter of 30 µm [7]. In figure 4.1, a schematic drawing of TiPC with these tynodes is shown. The windows are arranged in a 64x64 array with a pitch of 55 µm to match the spacing of the pixel pads on a TimePix chip [8]. An aligned tynode stack will form 'channels' in which electron multiplication will take place and be read out by the individual pixels. Two types of material were used to form the ultra-thin membrane: low-pressure chemical vapor deposition (LPCVD) silicon nitride (SiN) and ALD Al_2O_3. The former has a TEY of 1.6 (2.85 keV) for a membrane with a thickness $d = 40$ nm, while the latter has a TEY of 2.6 (1.45 keV) for a membrane with $d = 10$ nm. On both tynodes, a titanium nitride (TiN) layer was deposited on the PE entrance side to provide in-plane conductivity. In a different process, the TiN layer was encapsulated within two layers of Al_2O_3 to improve the reliability of the fabrication process (see chapter 2 [9]). This tri-layer film had a TEY of 3.1 (1.55 keV). The film layer was deposited on a flat substrate.

The supporting mesh is a necessity in the design of the tynode array due to the fragility of ultra-thin films. However, there are some drawbacks as well. First of all, it reduces the sensing area of the detector: photoelectrons that land on the supporting mesh will not be detected. The collection efficiency of TiPC can be estimated by using the ratio of the surface area of the windows and the mesh. For an array of windows with a diameter of 30 µm and a pitch of 55 µm, the active surface area is only 23.4%. Second, the collection efficiency also depends on the alignment of the windows. Misalignment can potentially result in loss of SEs in the tynode stack. Last, SEs can be trapped within the dielectric material (silicon nitride) of the mesh. During prolonged irradiation, charge can accumulate on the exposed surface of the dielectric mesh and cause distortions in the electric field.

Therefore, new tynodes have been made with some improvements, such as increased window size, dome-shaped membranes, alignment grooves and a metal mesh cover [10]. First, the window diameter can be increased to 45 µm, which improves the active surface area to 52.6%. Second, the dome-shaped membranes have a focusing effect on SEs: they are directed to the center of the next dome. This ensures that SEs are contained within their 'channel' above the corresponding pixel pad. The dome shapes are created by etching and smoothing circular pillars into bumps on the silicon substrate before depositing the film layer. Third, alignment grooves are etched in the silicon frame of the tynode, which are used to align two tynodes by placing glass quartz wires between them. This 'self-alignment process' improves the accuracy of the alignment. Last, the dielectric

mesh can be covered with a metal layer, which will prevent electrons to be trapped. Although, these new features alleviate some of the concerns, it increases the complexity of the fabrication process.

In this paper, we present an entirely different tynode design, which eliminates the need of a supporting mesh by forming a corrugated membrane of ultra-thin films. In a recent paper, a new class of nanoscale mechanical metamaterials with enhanced robustness, flexibility, rigidity and strength was reported by Davani et al. [11]. They formed corrugated plates by ALD of an ultra-thin Al_2O_3 film on a patterned silicon wafer, which acted as a mold and was removed afterwards. Their plate metamaterials were extremely flat, ultra-light and had shape-recovering properties. By using a corrugated membrane, the mechanical strength is enhanced compared to a flat membrane, while the membrane thickness is constant throughout the entire structure. The corrugated Al_2O_3 film can be functionalized as a tynode by adding a conductive layer, such as TiN [7, 9].

This design has many advantages. First, the effective area of these films is nearly 100%: an incoming electron can generate TSEs on any part of this ultra-thin corrugated membrane. Second, alignment precision is less stringent in this case, so the inclusion of alignment grooves becomes optional. Third, the honeycomb-shaped domes can be tailored to have a focusing effect, which is still needed to direct SEs onto the pixel pads. Fourth, the risk of charge accumulation within the tynode stack is eliminated, since the thick dielectric mesh is no longer present. Last, the fabrication process is less complex in comparison.

A metamaterial is defined as a material engineered to have properties that does not naturally occur. The corrugated membrane presented in this work is categorized as a mechanical metamaterial, but the multi-layered film is also engineered to sustain SEE. In this paper, we will refer to 'metamaterial' as a material with enhanced mechanical strength and improved SEE properties. The corrugated membranes of multi-layered Al_2O_3/TiN/Al_2O_3 films are referred to as 'metamaterial tynodes'. In figure 4.2, a schematic drawing of a TiPC detector with metamaterial tynodes is drawn, which has a continuous surface for electron multiplication. In this paper, metamaterials with two different patterns are presented: one with a hexagonal/honeycomb pattern and one with an octagonal pattern. The latter is designed to match the pitch of the pixel pads of a TimePix chip. The electron emission yield of these metamaterial tynodes will be determined within a scanning electron microscope (SEM) using the collector-based method reported in chapter 2 [9].

4.2. DESIGN

THE mechanical plate metamaterial reported by Davani et al. has unique mechanical properties: enhanced robustness, flexibility, bending stiffness and flatness [11]. The enhanced robustness stems from the hexagonal honeycomb pattern. A failure mode of flat membranes due to stress is the formation of cracks, which propagate in straight lines. The triangular lattice of the honeycombs prevents this and localizes defects. Therefore, the chance of rupture is reduced. The enhanced bending stiffness and rigidity is provided by the intersections of the vertical walls and the horizontal segments, which resist deformation, although at the same time the flexibility is enhanced due to the non-

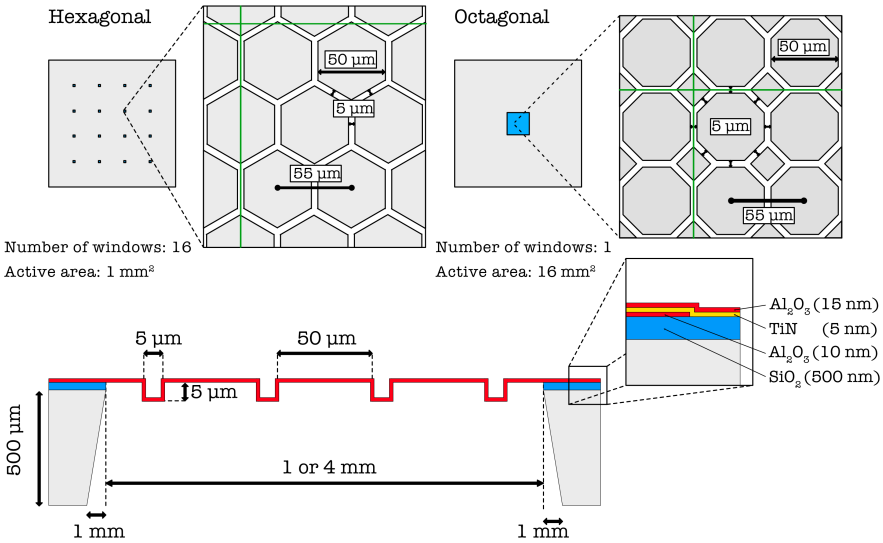

Figure 4.3: The corrugated membranes are suspended within a silicon frame with a dimension of 20 mm by 20 mm. For the hexagonal pattern, 16 square windows are opened in the silicon frame. Each corrugated membrane has an active area of ~ 1 mm^2. For the octagonal pattern, the silicon frame has a single window in which a membrane with an active area of ~ 16 mm^2 is suspended. Both patterns meet the design requirement that any perpendicular plane (green lines) is intersected by a vertical wall (black lines).

continuous top and bottom surface, which allow the plates to be folded (figure 4.3). The combination of enhanced bending stiffness and flexibility leads to the shape-recovery property of the plates after extreme deformation.

Davami et al. also discussed design rules for their plate metamaterial [11]. First, a periodic pattern must be chosen, which for any plane perpendicular to the plate intersects with a vertical wall (figure 4.3). Otherwise, the plate will bend along a line that only contains horizontal elements. Second, the enhancement factor of the bending stiffness depends on the diameter of the cell, rib width and rib height. Although, the bending stiffness saturates for heights above 1 µm. The highest bending stiffness can be achieved by minimizing the rib width w and maximizing the cell diameter D. In that case, the enhancement factor EF is given by $EF_{\max} \approx (\frac{D}{w})^2$. Although, a large cell diameter will reduce the robustness of the plate due to the increased risk of crack propagation on the cell surface.

With these design rules in mind, two patterns are considered for the metamaterial tynodes: hexagonal honeycomb and octagonal. The hexagonal pattern fulfills the design criteria and has the desired properties, but the triangular lattice does not match the square spacing of pixels on a TimePix chip. Therefore, the octagonal pattern is designed to be compatible with a TimePix chip. First, the square lattice of the pattern matches the pitch/displacement of the pixel pads. Second, the octagonal-shaped cups have a focusing effect on SEs, which concentrate and bundle SEs above the individual pixel pads. The focusing effect of these octagonal-shaped cells has been simulated with COMSOL (figure

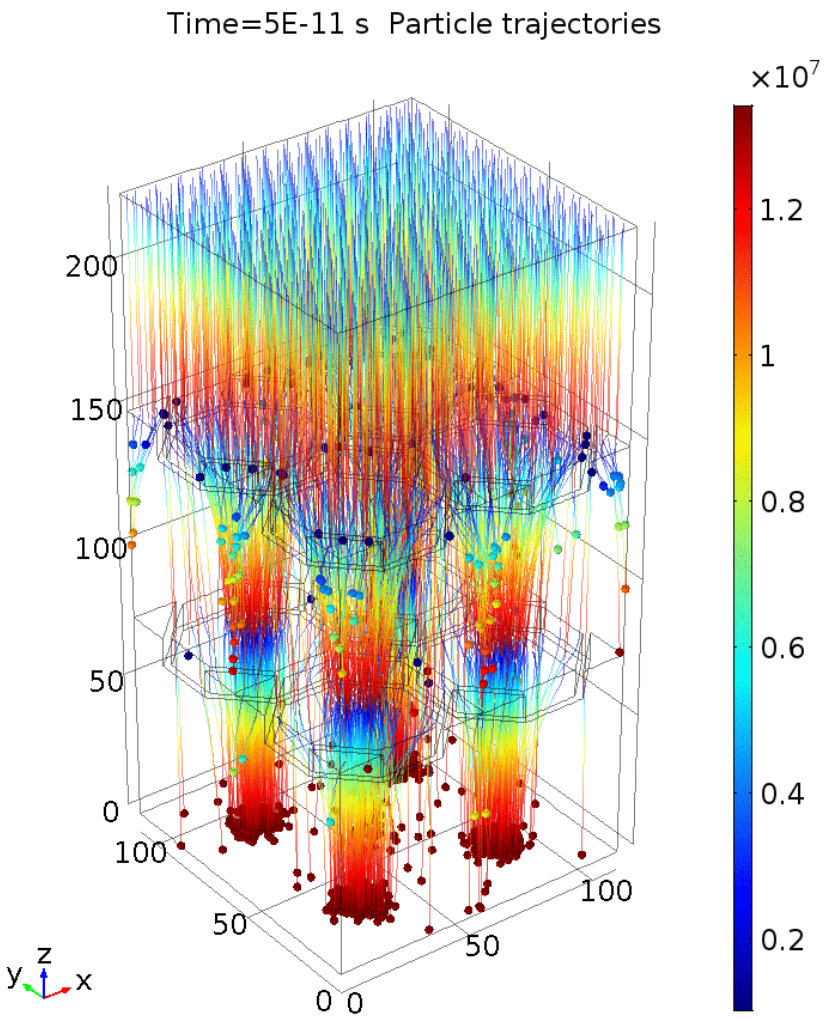

Figure 4.4: COMSOL simulation of a TiPC detector with two tynode stages. For the simulation, two modules of COMSOL were used: AC/DC and Charges Particle Tracing (CPT). The first module is used to simulate the static electric field. The potential difference ΔV between each stage is 1000 V. The second module is used to simulate transmission SEE from the two tynode stages. Photoelectrons are released uniformly from the photocathode. Each incoming electron generates one TSE on each tynode. Each PE and the SEs that they generate on each tynode will form a 'path', enabling us to estimate the collection efficiency of a TiPC detector.

4.4). A cell with a height of 5 µm is already sufficient to focus SEs, but the focusing point can be tailored by varying the height of the unit cells and/or the potential difference between the multiplication stages. Although, the latter is often attuned to the required electron energy to obtain the highest TEY for a given film thickness and is therefore a less flexible design parameter. The simulation also shows that PEs and SEs that enter the small square cups in the corner of each octagonal tend to land next to the pixel pads. This needs to be taken into consideration when estimating the collection efficiency.

The die size of the samples is 2 by 2 cm in which windows are opened by Deep-Reactive Ion Etching (DRIE) as shown in figure 4.3. For the hexagonal honeycomb pattern, there are 16 square windows with a width of 1.25 mm. For the octagonal pattern, there is a single square window with a width of 4.2 mm. These window sizes are defined on the back side of the silicon wafer, but will be approximately 0.2 mm smaller on the front side after etching since the DRIE process is not entirely anisotropic. The active surfaces are approximately 1 mm^2 and 16 mm^2, for the hexagonal and octagonal pattern respectively. Each unit cell in the corrugated membrane has a rib height and width of 5 µm, which is relatively shallow and open. Incoming electrons can still reach the bottom of the rib and contribute to electron multiplication. The ratio of 1:1 is ideal, since increasing the height further would create deep trenches for which it is more difficult for electrons to reach the bottom, i.e. the angle of incidence becomes smaller. Also, the height is sufficient in this case for focussing. The cell diameter is 50 µm and has a pitch of 55 µm, which is the same pitch between pixels on a TimePix chip. The film is a tri-layer Al_2O_3/TiN/Al_2O_3 composite with a thickness of 10/5/15 nm. This multilayered film is engineered as a membrane for electron multiplication by encapsulating a TiN layer, which provides in-plane conductivity that is needed to sustain electron emission (see chapter 2 [9]).

4.3. FABRICATION

WAFERS (4-inch, p-type with 5-10 Ω cm) with a thickness of 500 ± 15 µm are used as a substrate. The wafers are cleaned with a standard cleaning procedure before alignment markers are etched on the wafers for contact alignment. The sequence of the cleaning procedure is as follows: a plasma oxygen etch, a HNO_3 100% bath for 10 min, a demineralized water rinse for 5 min, a HNO_3 65% bath at 110 °C for 10 min and another water rinse.

The process can be divided in three parts. In the first part, a 3D mold is etched within the silicon substrate (figure 4.5a). A 3-µm-thick photoresist (PR) layer is used as a masking layer for DRIE in a Rapier Omega i2L DRIE etcher. The hexagon/octagon pattern is transferred to the PR and trenches with a depth of 5 µm are etched into the silicon substrate. The wafers are then cleaned with oxygen plasma to remove residual polymers from the DRIE process followed by a standard cleaning procedure. Afterwards, the wafers are put in an oven at 1100 °C to wet thermally grow a SiO2 layer with a thickness of 500 nm. This layer will act as a sacrificial and stopping layer.

In the second part, the tri-layer film material is deposited conformally on the mold (figure 4.5b). First, a layer of Al_2O_3 is deposited by ALD in a thermal ALD ASM F-120 reactor at 300 °C using trimethyl-aluminum (TMA) and water as a precursor and reactant, respectively. A strip of the newly deposited layer is removed from the edge of each die to

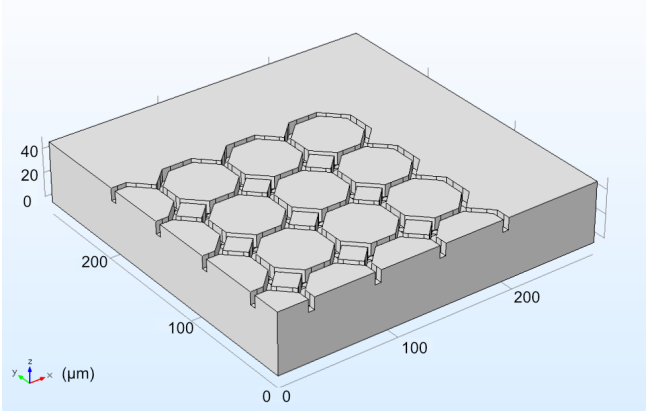

(a) Silicon mold. A 3D pattern is etched on the front side of a silicon wafer by DRIE.

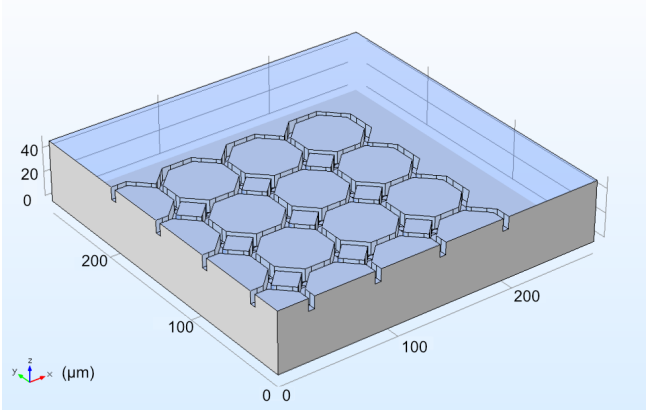

(b) ALD of a tri-layer film. The Al_2O_3/TiN/Al_2O_3 film is deposited uniformly on the 3D pattern.

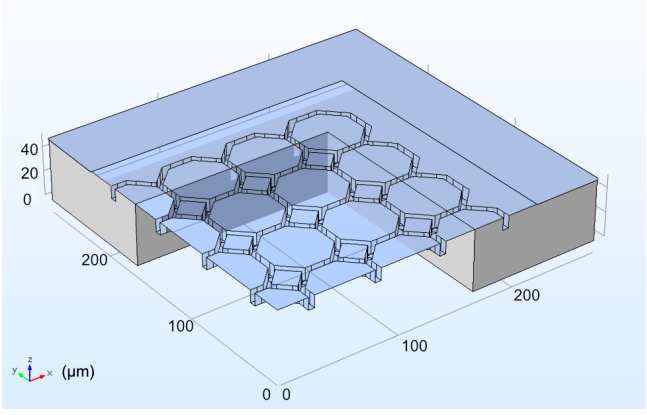

(c) Release of the metamaterial film. On the backside of the wafer, square windows are etched into the silicon substrate by DRIE. The landing layer is a silicon dioxide (SiO_2) film, which is removed by hydrofluoric (HF) vapor etching afterwards.

Figure 4.5: Overview of the fabrication process

create a contact point for the next layer to the silicon substrate. First, the Al_2O_3 layer is plasma etched in an Omega Trikon plasma etcher. Then, the SiO2 layer is removed with a plasma etch in a Drytek plasma etcher. The wafers are cleaned afterwards using a new cleaning procedure that omits the 'fuming' HNO_3 65% bath step. Next, a layer of ALD TiN is deposited in an Ultratech Fiji G2 using titanium chloride ($TiCl_4$) as precursor and nitrogen plasma as reactant at 250 °C. The third layer of Al_2O_3 is then deposited with the same process parameters as the first layer in the same reactor.

In the third part, the corrugated membrane will be released by opening windows in the silicon substrate (figure 4.5c). First, a plasma-enhanced chemical vapor deposition (PECVD) oxide layer with a thickness of 1 µm is deposited on the front side of the wafer in a Novellus Concept One system. This oxide layer protects the tri-layer film from mechanical damages, since the wafers are placed upside down in the subsequent steps. The backside of the wafer is stripped by using two plasma etches: the ALD TiN and ALD Al_2O_3 layers are stripped in an Omega Trikon plasma etcher, while the thermal oxide is removed in a Drytek plasma etcher. Once the backside is stripped and cleaned, a PECVD oxide layer with a thickness of 5 µm is deposited on the backside of the wafer in a Novellus Concept One system. This PECVD oxide layer is the masking layer for DRIE. The pattern of the window openings and scribe lines are transferred to the backside of the wafer using PR with a thickness of 3.1 µm. This pattern is then plasma etched into the PECVD oxide masking layer in a Drytek plasma etcher. The wafers are now ready for the final release using a Rapier Omega i2L DRIE etcher. First, a fast DRIE recipe is used to etch approximately 495 µm into the silicon substrate until the rib pattern of the corrugated film becomes visible. This is one of the critical steps in this process, since over-etching can damage the structure of the ribs of the corrugated membrane. The protective PECVD oxide on the front side is then removed in a HF vapor etch chamber using 4 etching cycles of HF and ethanol with a flow of 190 sccm and 220 sccm, respectively, for a duration of 10 min per cycle. If this oxide layer is not removed before the final release steps, it will be the main contributor to the stress within the film and can cause ruptures. The wafer is then cleaved along the scribe lines. The individual dies are transferred to a carrier wafer with pockets to hold them. The remaining 5 µm of silicon is removed with a slower DRIE recipe within the Rapier. At this point, the dies become fragile and should be handled with care. The dies are then cleaned with oxygen plasma in a TEPLA plasma cleaner to remove any residual polymers from the DRIE process. The final and critical step is the removal of the thermal oxide layer in a HF vapor etch chamber using the same recipe as before. This step is repeated until the ultra-thin membranes are released. For the samples presented in this work, the recipe was repeated 3 times before the membranes were successfully released. The optimal etch time for these dies was 4×10 min. After the final release, the membranes are fragile (but still relatively strong considering their thinness) and should be transported with care.

4.4. EXPERIMENTAL SETUP

4.4.1. TRANSMISSION SECONDARY ELECTRON YIELD

THE transmission (secondary) electron yield is measured with a hemispherical collector system in SEM as shown in figure 4.6a. A more extensive description of the method is given in chapter 2 [9]. The system is mounted on the moving stage of a Thermo Fisher NovaNanoLab 650 Dual Beam SEM, which allows us to use all functions of the SEM while performing TEY measurements. The sample holder, mesh grid and collector are connected to Keithley 2450 source meters via a feedthrough into the vacuum chamber. Before the measurements, the electron beam current is measured using a Faraday cup that is placed next to the sample. The PE energy ranged from 0.3 – 10 keV with a beam current from 0.06 to 0.54 nA. The beam current I_0 depends on the PE energy and is measured for each energy.

The measurement is performed with a scanning electron beam by using the image acquisition mode of the SEM. The raster pattern distributes the electrons over a larger surface and lowers the electron dose. This mitigates charge-up effects and/or the build-up of surface contamination. The following SEM settings are used during the measurement: dwell time of 1 µs, magnification of 50X, horizontal field width of 2.56 mm and a resolution of 1024 x 884. The dwell time is defined as the average time that the electron beam is irradiating the specimen to acquire one pixel in a SEM image. Using these settings, the area of the irradiated surface can be estimated, which in this case is 5.66 mm^2. The measured yields are averaged over the surface and over time, i.e. the yield is calculated from multiple frames. For the measurement of the smaller membranes with the hexagonal pattern, a horizontal field width of 0.640 mm is used.

primary electrons (PEs) can generate backscattered electrons (BSEs), reflection secondary electrons (RSEs), forward-scattered electrons (FSEs) and transmission secondary electrons (TSEs) from a tynode (figure 4.6a). The transmission currents are measured directly within the collector, while the reflection currents are determined indirectly using the sample current. The fast electrons (BSEs and FSEs) can be separated from the slow electrons (RSEs and TSEs) by performing a measurement with a negative sample bias (−50 V) and a measurement with a positive sample bias (+50 V). The Keithley 2450 sourcemeters can perform current measurements while simultaneously applying different biases to the electrodes. When a negative bias is applied to the sample, the sample holder, retarding grid and collector are biased at -50, 0, −50 V, respectively. When a positive bias is applied to the sample, they are at +50, 0, 50 V. In the first case, both fast and slow electrons are repelled from the tynode. The (total) transmission electron yield (TEY) $\sigma_T(E_0)$ is given by

$$\sigma_T(E_0) = \frac{I_{RG-} + I_{C-}}{I_0} \tag{4.1}$$

where E_0 is the electron energy of the electron beam, I_0 is the beam current, I_{RG-} is the retarding grid current and I_{C-} is the collector current. The subscript '-' indicates that the currents are measured with a negatively biased sample. The total emission yield is given by: $\sigma(E_0) = (I_0 - I_{S-})/I_0$. It is the sum of the (total) reflection electron yield (REY) and TEY: $\sigma(E_0) = \sigma_T(E_0) + \sigma_R(E_0)$. Therefore, the REY $\sigma_R(E_0)$ is given

$$\sigma_R(E_0) = \frac{I_0 - I_{S-} - I_{RG-} - I_{C-}}{I_0} \tag{4.2}$$

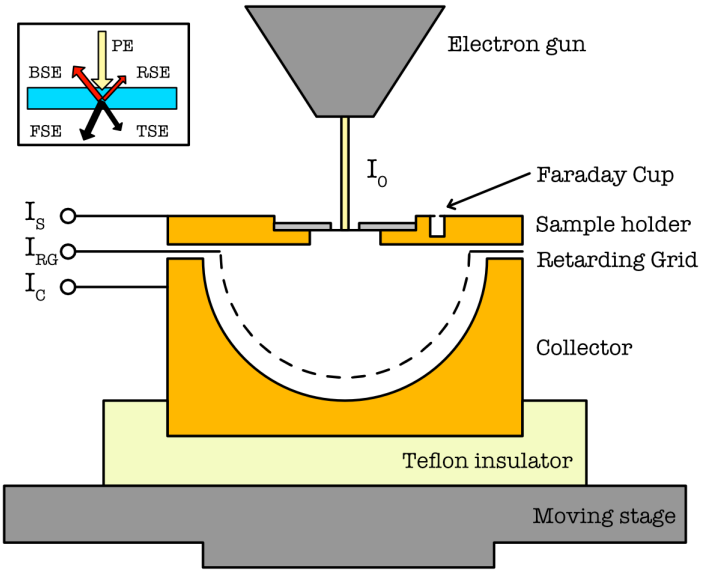

(a)

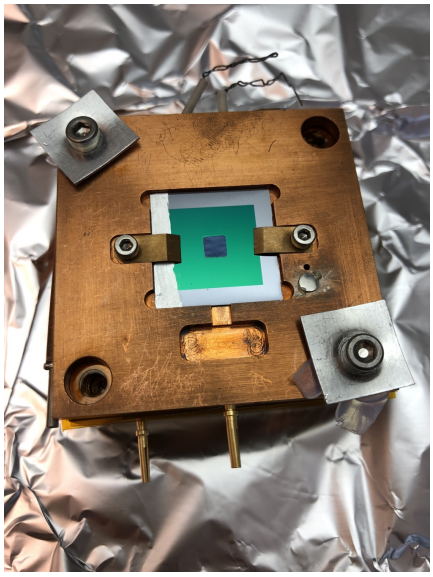

(b)

Figure 4.6: Experimental setup. (a) schematic drawing of the collector system. The forward-scattered electrons (FSEs) and TSEs are collected by the retarding grid and/or collector. By measuring the retarding grid current I_{RG} and the collector current I_C, the forward-scattered electron yield (FSEY) and transmission secondary electron yield (TSEY) can be determined. The backscattered electron yield (BSEY) and reflection secondary electron yield (RSEY) are determined indirectly by measuring the sample current I_S. (b) The collector system with one of the octagonal metamaterial membrane mounted in the sample holder.

where I_{S-} is the sample current. In the second case, the sample is positively biased and only fast electrons are measured. The forward-scattered electron yield (FSEY) $\eta_T(E_0)$ and the backscattered electron yield (BSEY) $\eta_R(E_0)$ are respectively given by

$$\eta_T(E_0) = \frac{I_{RG+} + I_{C+}}{I_0} \tag{4.3}$$

and

$$\eta_R(E_0) = \frac{I_0 - I_{S+} - I_{RG+} - I_{C+}}{I_0} \tag{4.4}$$

where I_{S+} is the sample current, I_{RG+} is the retarding grid current and I_{C+} is the collector current. The subscript '+' indicates that the currents are measured with a positively biased sample. By subtracting the contribution of the fast electrons from the total emission yield, the transmission secondary electron yield (TSEY) can be determined

$$\delta_T(E_0) = \frac{I_{RG-} - I_{C-}}{I_0} - \frac{I_{RG+} + I_{C+}}{I_0} \tag{4.5}$$

and the reflection secondary electron yield (RSEY)

$$\delta_R(E_0) = \frac{I_0 - I_{S-} - I_{RG-} - I_{C-}}{I_0} - \frac{I_0 - I_{S+} - I_{RG+} - I_{C+}}{I_0} \tag{4.6}$$

4.4.2. SURFACE SCAN & YIELD MAPS

A TSEY map can be constructed by measuring the transmission current as a function of time. The TSEY is calculated by using equation 4.5 and is mapped to the coordinate of the electron beam during image acquisition. When a (single) SEM image is taken, the (transmission) emission current will vary across the surface of the sample. A yield map will show the difference in electron emission and can be compared to the SEM image. The method is described in appendix C and operates on the same principles as SEM image construction. The SEM settings are chosen such that the Keithley 2450 sourcemeters are able to map the measured current (as a function of time) to the pixels in the SEM image. This method requires a much slower scan speed than the method presented in section 4.4.1. Also, only one image frame is acquired. A dwell time of 1 ms is used, which is a compromise between speed and accuracy. A larger dwell time might cause charge-up effects and/or surface contamination. The resolution of the image is 512 x 442 acquired with a dwell-, line- and frame time of 1 ms, 560 ms and 4.2 min respectively. The electron beam energy used to acquire the image is 3.2 keV with a current of 0.29 nA, which yields the highest TEY for the membranes considered in this paper. The magnification is 500X or 1000X, which shows the difference in yield across the 3D structure of the corrugated membrane more clearly.

4.5. RESULTS & DISCUSSION

4.5.1. FABRICATION

In figure 4.7, SEM images of the front- and backside of a metamaterial tynode with a hexagonal pattern are shown. The contrast in the image is due to the 3D structure of the film. In figure 4.6a, the ribs extrude into the plane and behave as trenches from which it is difficult for SEs to escape, therefore the ribs are dark in the image. In figure 4.7a, the backside of the film is shown. In this case, the ribs protrude out of the plane and are brighter than the film. The difference between both sides is more apparent in figure 4.8, which shows a broken film that curled up after release.

In figure 4.9, SEM images of a metamaterial tynode with an octagonal pattern are shown. The black dots on the surface are residues from the fabrication process. On a different sample, a close-up of a broken film shows flakey residues on the film and the ribs (figure 4.10). These are residues of the HF vapor etch. In figure 4.10b, the etch lines of the DRIE process are visible as indentations in the ribs, which are due to the cyclic process of etching and passivation. For the samples in this paper, 8 cycles were used to etch 5.1 µm into the silicon wafer.

There are two critical steps in the fabrication process of these metamaterial tynodes. First, the DRIE process used to open the windows from the backside of the wafer requires careful monitoring. Although the thermal oxide layer acts as a landing layer, the etch rate is different for windows with different widths. In general, more open features are etched faster. As such, there is a chance of over etching, which can damage the ribs of the metamaterial film. Second, the metamaterial membranes are fragile after the final release step in the HF vapor chamber. They are prone to breakage due to air pressure differences and/or electrostatic forces.

The largest window has a surface of ~ 16 mm^2 corresponding to 72 by 72 pixels, while a TimePix chip has 256 by 256 pixels. To span the entire chip, the window size should increase. However, the larger membranes will be more fragile. This can be remedied by making smaller windows and including a silicon frame. For instance, by sacrificing a row/column of 4 pixels (or a width of 0.22 mm), the surface of a TimePix chip can be covered by having 8x8 windows each accommodating 30x30 pixels. However, this solution decreases the collection efficiency.

4.5.2. TRANSMISSION SECONDARY ELECTRON YIELD

In figure 4.11 and 4.12, full sets of yields are given for the membranes with the octagonal and hexagonal pattern, respectively. A full set of yields consists of the BSEY (η_R), the RSEY (δ_R), the FSEY (η_T) and the TSEY (δ_T). The TEY (σ_T) is the sum of the FSEY and the TSEY. It is the metric to compare the performance of tynodes.

In figure 4.11a and 4.12a, the yield curves were determined on tynodes that were placed in the default orientation with the window (in the silicon substrate) and the unit cell cups facing downwards. In this orientation, the TSEs are expected to be focused to the center as shown before in figure 4.4. The extruded ribs have the same electric potential as the center part of the hexa- and octagon, so the electric field would focus TSEs to the center of the unit cell of the next tynode. In figure 4.11b and 4.12b, the yield curves were determined on tynodes that were placed upside down. The unit cell cups are facing

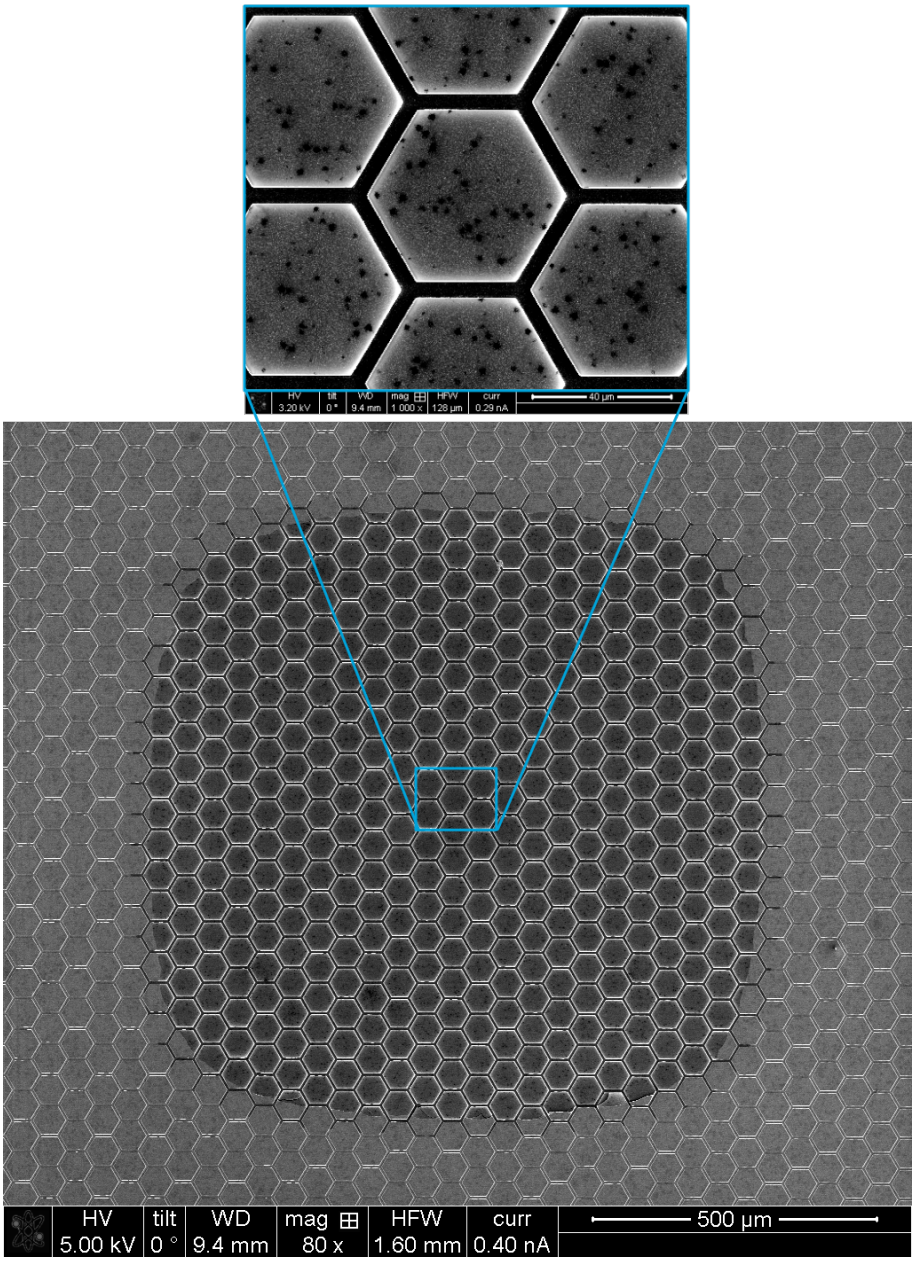

(a) Front. Unit cells facing downwards ↓

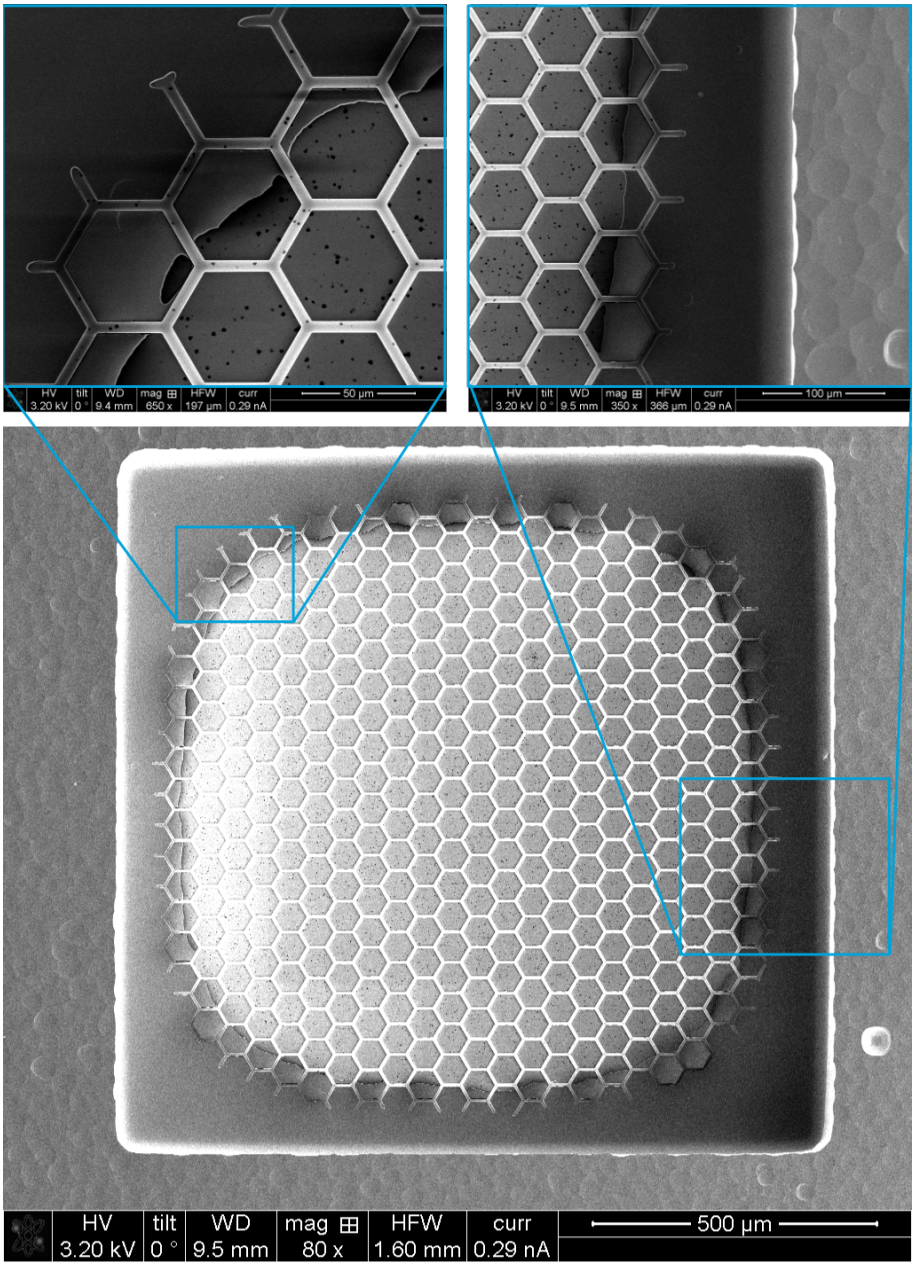

(a) Back. Unit cells facing upwards ↑

Figure 4.7: SEM images of a metamaterial film with a hexagonal pattern. (a) The contrast between the active area and the window frame is due to the transparency of the film for 5 keV electrons. (a) On the backside, the ribs protrude outwards and appear brighter since also SEs emitted from the top and the sidewalls of the ribs can more easily reach the detector of the SEM. On the edge, the ribs disappear into the silicon substrate.

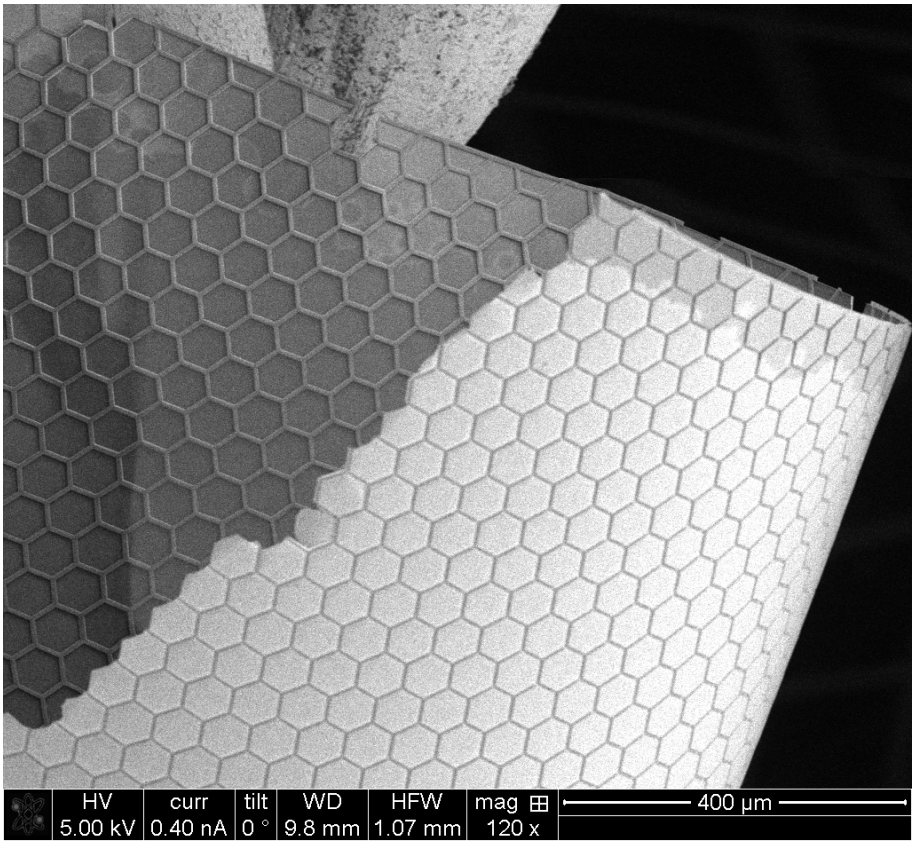

Figure 4.8: A SEM image of a broken film curled up after release. It clearly shows the ribs of the honeycombs on the front- and backside.

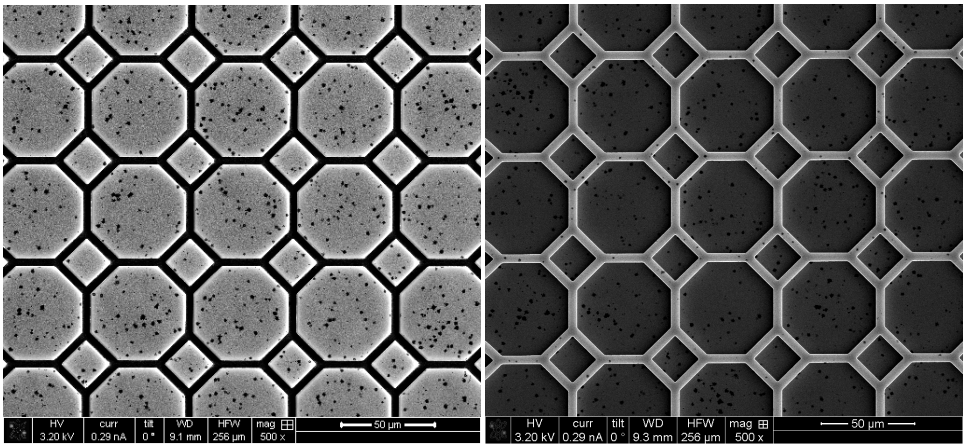

(a) Front. Unit cells facing downwards ↓ (b) Back. Unit cells facing upwards ↑

Figure 4.9: SEM images of a metamaterial film with an octagonal pattern.

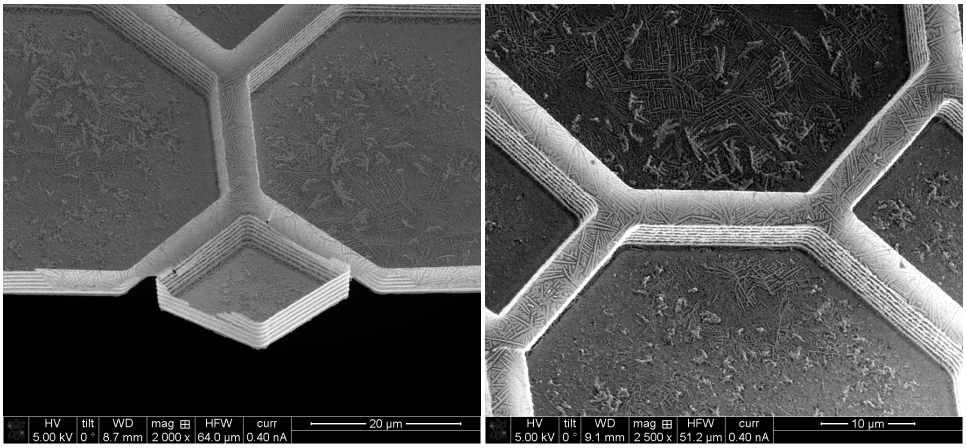

(a) (b)

Figure 4.10: Close-up of a broken metamaterial film with an octagonal pattern with the unit cells facing upwards ↑. The etch lines of the DRIE process are visible on the ribs.

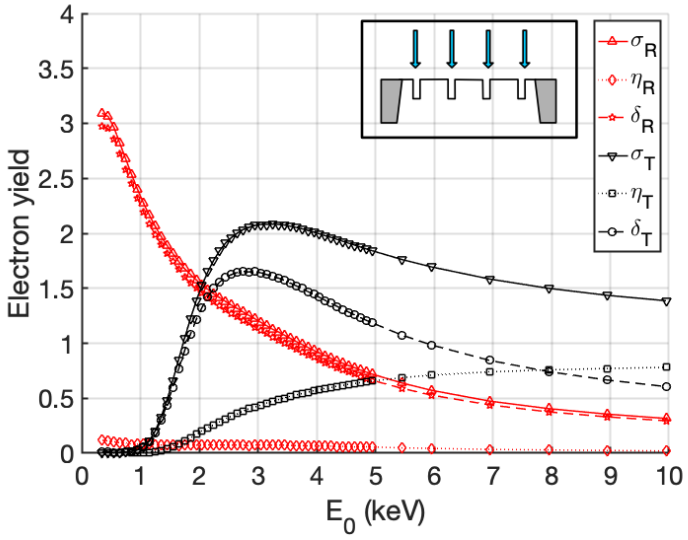

(a) Front. Unit cells facing downwards ↓

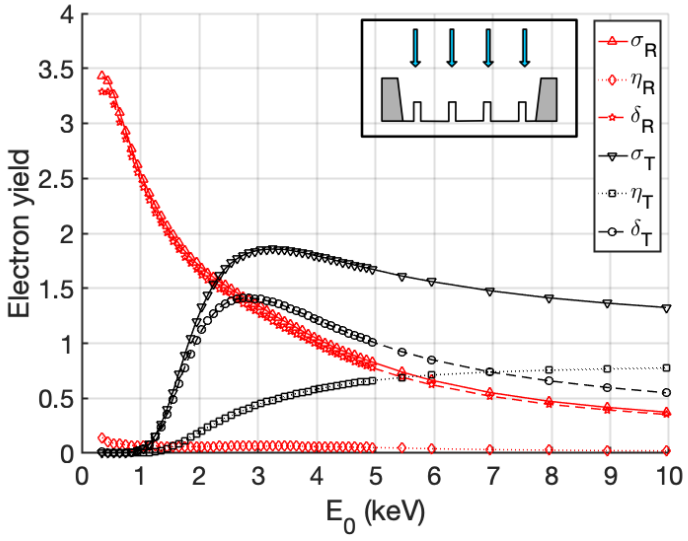

(b) Back. Unit cells facing upwards ↑

Figure 4.11: Electron yield curves of an octagonal metamaterial film with a thickness of 15/5/10 nm. For each PE energy E_0, a surface with an area of 5.75 mm^2 is irradiated by the electron beam and the average yield is calculated. Therefore, the variation in yield due to the microstructure of the corrugated film is averaged out. The resulting smooth yield curves are similar to the yield curves measured on flat membranes (see chapter 2 [9]).

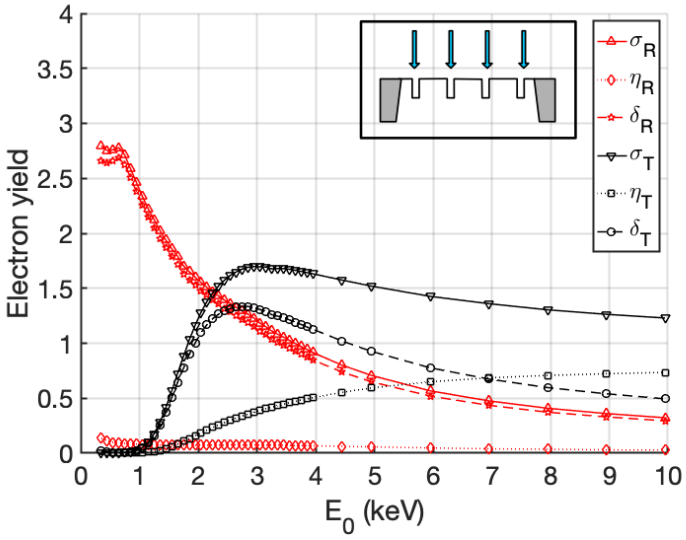

(a) Front. Unit cells facing downwards ↓

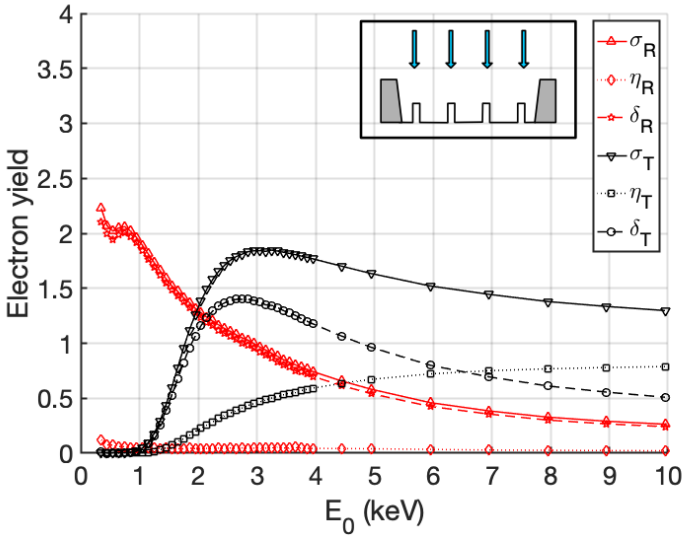

(b) Back. Unit cells facing upwards ↑

Figure 4.12: Electron yield curves of an hexagonal metamaterial film with a thickness of 15/5/10 nm. For each PE energy E_0, a surface with an area of 0.35 mm^2 is irradiated by the electron beam and the average yield is calculated. The window in which the hexagonal metamaterial film is suspended is smaller (see figure 4.3).

upwards in this case. In this orientation as shown figure 4.13, the corrugated membrane is relatively flat on the transmission side and focusing effect is not to be expected. Depending on the application, one might prefer one placement over the other.

The TSEY and FSEY curves in figure 4.11 and 4.12 are typical for tynodes. They are similar to the curves that were reported in chapter 2 [9] for flat $Al_2O_3/TiN/Al_2O_3$ tynodes. A TSEY curve has two distinct features: the threshold energy and the maximum TSEY. The threshold energy E_c coincides with the onset of the TSEY curve and is defined as the required PE energy to generate TSEs, which depends on the thickness and the material of the film. The maximum TSEY $\delta_T^{\max}$ is achieved by using the optimal PE energy, at which the PE is relatively efficient in transferring energy near the exit surface of the film to generate TSEs. When the PE energy is further increased, the film will become electron transparant ($\eta_T \to 1$), which results in a lower energy transfer and TSEY. The FSEY curve also has an onset, which depends on the film thickness and the required energy for a PE to penetrate the film. For higher energies, the film becomes electron transparent and the curve approaches 1. As a consequence, the amount of energy that a PE can transfer before it pass through a tynode is lower.

The octagon pattern has a maximum TEY $\sigma_T^{\max}$ of 2.15(3.15 keV) and 1.85(3.15 keV) when its cells face down- and upwards, respectively. For both measurement, the critical energy E_c is ~ 1.15 keV. The critical energy is the PE energy for which the first TSEs are generated and is correlated to the membrane thickness. The difference in $\sigma_T^{\max}$ for the same membrane is solely due to the 3D structure of the corrugated membrane (figure 4.13). PEs are directional and are expected to hit the membrane perpendicularly. When the cells are facing downwards, the PEs can enter the ribs and generate TSEs from the walls and at the bottom. When the cells are facing upwards, a PE can generate TSEs at the top of the rib and on the walls, but since the angular distribution of (transmission) SEE is a cosine distribution, TSE are more likely to be recaptured.

The hexagon honeycomb pattern has a maximum TEY $\sigma_T^{\max}$ of 1.7(3.05 keV) and 1.85 (3.05 keV) when placed upside down. For both measurements, the critical energy is again ~ 1.15 keV. In this case, the yield is lower when the unit cells are facing downwards. This is in contradiction with the mechanism shown in figure 4.13. However, the reduction in TEY can be explained by the window size of the silicon frame, which, for the hexagonal pattern, has a width of 1.25 mm and SEs are more likely to be recaptured by the silicon frame. In comparison, the window of the membrane with the octagon pattern has a width of 4.2 mm, so recapture by the silicon frame is minimal in this case.

The maximum TEY of multi-layered membranes have been measured on flat membranes with similar thicknesses in chapter 2 [9] and are summarized in table 4.1. A bi-layer TiN/Al_2O_3 film with a thickness of 5.7 + 25 nm had a $\sigma_T^{\max}$ of 2.1(2.55 keV) and E_c of 1 keV. A tri-layer $Al_2O_3/TiN/Al_2O_3$ film with a thickness of 12.5 + 5.7 + 12.5 nm had a $\sigma_T^{\max}$ of 2.7(2.75 keV) and E_c of 1 keV. The tri-layer film is similar to the tri-layer film presented in this paper. However, the TiN layer is deposited by sputtering for the former, while ALD is used in the latter. The slight shift in critical energy E_c of 200 eV and the shift of the max peak by 400 to 600 eV indicates that the films presented in this paper are thicker in comparison. The difference in thickness can be due to the different deposition techniques of the TiN layer, but also due to residues from the process as seen in figure 4.9a (black dots) and 4.10b (flakes). Also, the lower $\sigma_T^{\max}$ for the membranes presented in this work might

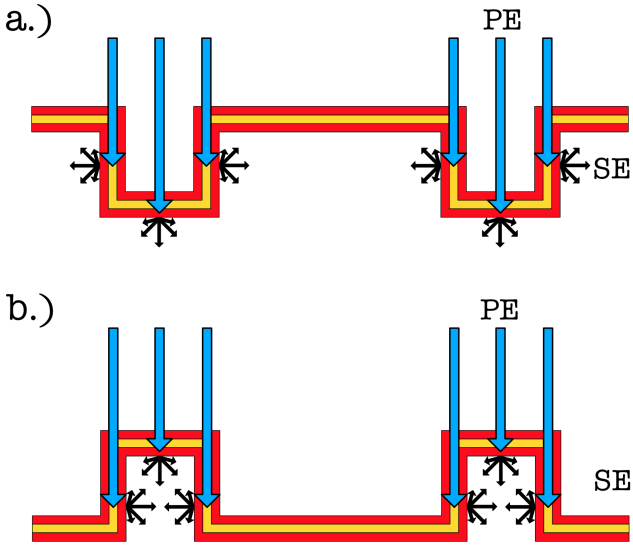

Figure 4.13: The hexagon/octagon unit cell cups facing: a. downwards. TSEs escape into the unit cell cups and are focused to the next tynode. b. upwards. TSEs are recaptured within the rib.

Table 4.1: Comparison between flat multi-layered membranes and corrugated membranes with similar thicknesses. The arrows ↓,↑ indicates the direction the unit cells are facing.

Type	$d_{Al_2O_3}$ (nm)	d_{TiN} (nm)	$d_{Al_2O_3}$ (nm)	$\sigma_T^{\max}$	$E_T^{\max}$ (keV)	E_c (keV)	Reference
Bi-layer	-	5.7	25	2.1	2.55	0.95	[9]
Tri-layer	12.5	5.7	12.5	2.7	2.75	0.95	[9]
Octagon ↓	10	5	15	2.15	3.15	1.15	this work
Octagon ↑	10	5	15	1.85	3.15	1.15	this work
Hexagon ↓	10	5	15	1.7	3.05	1.15	this work
Hexagon ↑	10	5	15	1.85	3.05	1.15	this work

be caused by the residues on the membrane surface.

The TEY of a metamaterial tynode with the hexagonal pattern has also been determined in a different setup: the tynode test setup (Tytest) [12]. The Tytest is a rudimentary TiPC assembled in a dedicated vacuum system, which consists of a single multiplication stage (tynode), an e-gun as electron source and a TimePix chip as read-out. The TEY is in good agreement for PEs with energy of 1.2 - 1.6 keV, but has a bigger spread for PEs with energies of 1.7 and 1.8 keV.

4.5.3. ACTIVE AREA & COLLECTION EFFICIENCY

The active area of a tynode can be determined by measuring TEY as a function of the coordinates on the surface of a tynode. In figure 4.14b, the yield map is given for a tynode with an octagon pattern. The TEY is higher than one on the entire surface. The active surface is thus also near 100%. However, there is some variation in yield across the surface of the corrugated membrane. The 'hotspots' on the yield map are near the perpendicular walls of the unit cell cups. A PE transmitting through a membrane is expected to lose energy, but will still have sufficient energy to induce reflection SEE on the walls if the PE is redirected towards it. PEs in bulk retain 30 to 40% of their initial energy E_0 at the depth of their range $R(E_0)$ [13]. The probability that this second emission process occurs increases as the point of entry of the PE is closer to the walls of the cups.

When the membrane is placed with the ribs facing upwards (4.15a), the situation is slightly different. There is no focusing effect within the unit cells and TSEs that are generated within the ribs at the top are more likely to be recaptured (figure 4.13). The TEY map is more uniform in this case (figure 4.15b), but the ribs are more pronounced in reflection as can be seen in the SEM image (figure 4.15a) and reflection yield map. In this case, BSEs can induce a second emission process on the wall of the cups and increase the RSEY.

The collection efficiency of a detector is defined as the ratio of the total number of photoelectrons that are emitted from the photocathode and the number of electrons that are able to trigger a signal in the detector. The active area of the tynodes is near 100% in both cases, which improves the collection efficiency of TiPC. Unfortunately, the hexagonal honeycomb membranes have a triangular lattice that does not match the square lattice of a pixel chip. They are therefore less suitable for TiPC. The octagonal pattern has the same lattice spacing as the pixel pads of a TimePix chip. When the octagons are aligned, the focussing effect of each tynode will bundle the electron avalanche in columns above each pixel (figure 4.4). It can be argued that photoelectrons that are generated above the ribs or the squares in the corner of each unit cell will not be focused. They end up next to the pixel pads and will not trigger a pixel. If only the surface area of the octagon is taken, then the collection efficiency is 68%. If we assume that the SEs generated within the ribs might contribute as well, then it is 82%. The remaining 18% of the surface are the squares.

The collection efficiency can be improved by using a different corrugated pattern for the first tynode, which directs the TSEs away from the squares. Also, the collection efficiency can increase when the ribs are shaped differently by using a U- or V-shape. TSEs generated at the bottom of each rib will be forced into one of the octagonal cells in this case. This can be achieved by using different etching recipes for DRIE or using wet

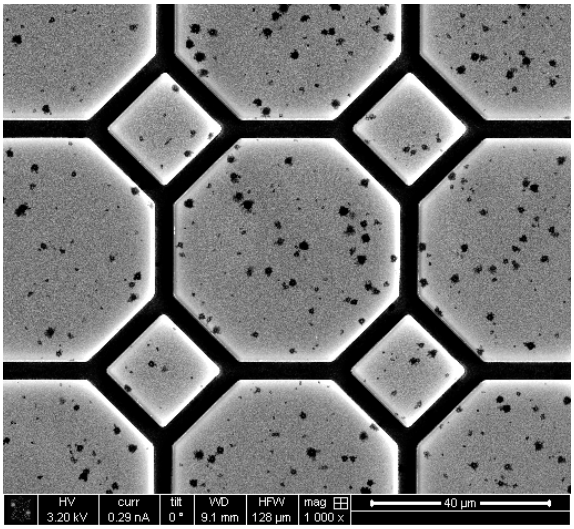

(a)

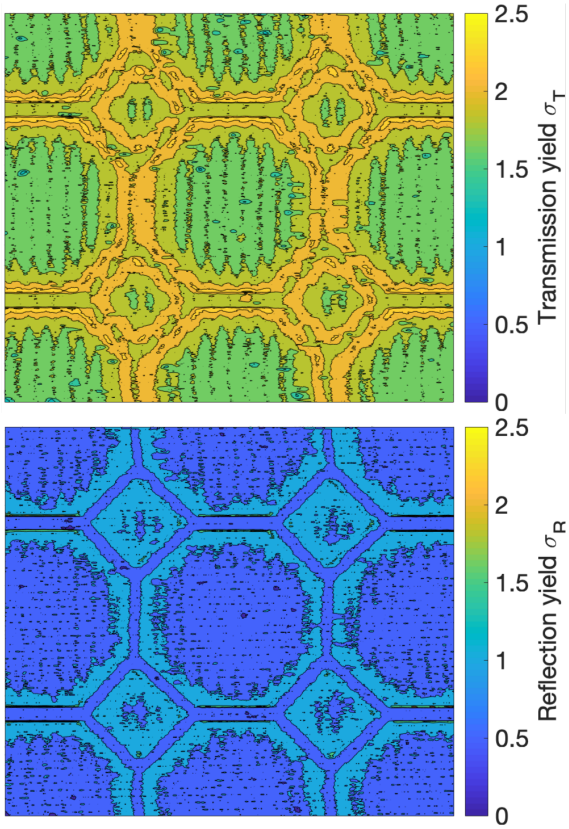

(b)

Figure 4.14: Yield map of an octagon tynode with ribs facing downwards. The reflection yield map matches the SEM image. The former is determined from the sample current, while the latter is determined from SEE from the sample. The glow near the edge of the octagon/square is visible on both pictures. The TEY near the vertical walls is higher due to FSEs that both generate SEs from the bottom of the cups as well from the walls.

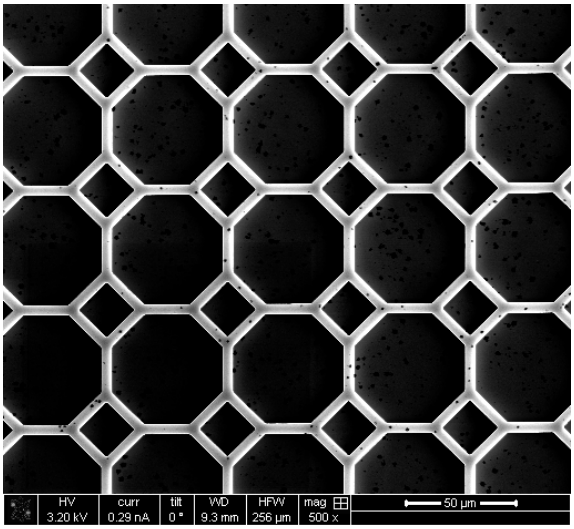

(a)

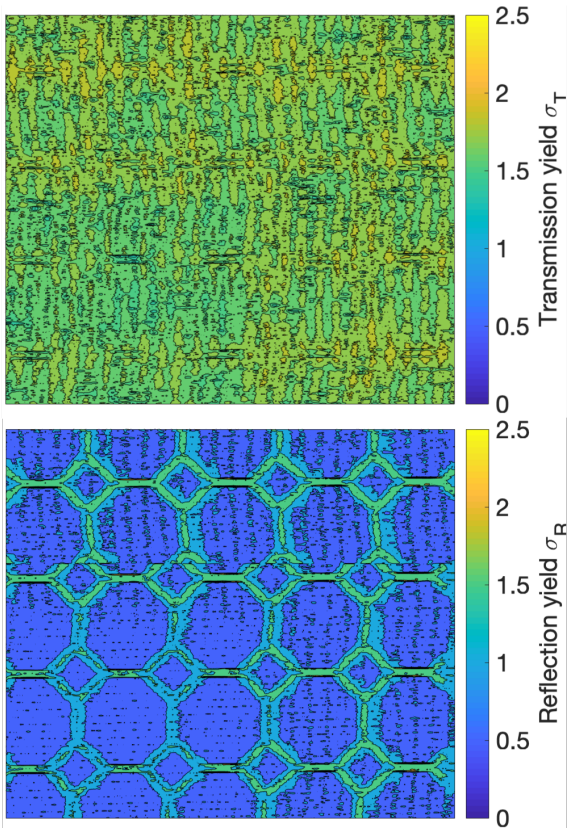

(b)

Figure 4.15: Yield map of an octagon tynode with ribs facing upwards. The TEY map is more uniform. In reflection, the vertical walls of the ribs generate a lot more RSEs compared to the cups, since the probability of recapture is lower.

chemical etching with KOH for anisotropic patterns.

4.6. CONCLUSION & OUTLOOK

WE have shown that the active surface of tynodes can be increased by forming corrugated membranes, which have enhanced mechanical properties. The collection efficiency of TiPC can be improved by using these metamaterial tynodes. The corrugated pattern is formed by conformally depositing a multi-layered Al_2O_3/TiN/Al_2O_3 film on a 3D silicon mold. The film is functionalized as a tynode by encapsulating a TiN layer to provide in-plane conductivity. The performance of the metamaterial tynode in terms of TEY is lower compared to flat membranes with similar composition. However, by optimizing the thickness of the ALD TiN layer in this process, the performance can be improved.

For TiPC, the TEY of the tynodes needs to be improved to 4 or higher. One way to achieve this is to consider a different SEE material, such as ALD magnesium oxide (MgO), which has a reflection secondary electron yield of 4.8 as we have reported in ref. [14]. In addition, thermal annealing (up to 1100 °C) and chemical treatments further improved the reflection secondary electron yield of ALD MgO to 7.2 and 6.8, respectively. We have also shown that it is feasible to fabricate ALD MgO tynodes in ref. [15] and in chapter 3 [16]. A transmission SEY of 2.9 was measured on a tynode with a thickness of 5 nm. The fabrication process presented in this work can be adapted to replace ALD Al_2O_3 with ALD MgO. Thermal and/or chemical treatments can be considered as well.

Improvements can be made to the design of the metamaterial tynode. The ribs can be improved by rounding the cross section into U- or V-shape, which will enhance the focusing effect: SEs that are generated within the walls of these ribs will be directed to the center of the unit cell and effectively increase the active surface. The number of pixels that the tynode covers can be increased to 256x256 by sacrificing a few rows of pixels to accommodate a silicon frame and divide the surface in smaller sections. Furthermore, the mechanical properties of the metamaterial tynode can be improved by altering the dimensions of the unit cells and or by including vertical side walls [11]. For instance, the spring constant scales quadratically with the height of the plate, which is a design parameter that can be optimized.

REFERENCES

[1] H. Chan, V. Prodanović, A. Theulings, T. ten Bruggencate, C. Hagen, P. Sarro *et al.*, "Ultra-thin corrugated metamaterial film as large-area transmission dynode," *Journal of Instrumentation*, vol. 17, p. P09027, 9 2022.

[2] H. van der Graaf, H. Akhtar, N. Budko, H. W. Chan, C. W. Hagen, C. C. Hansson *et al.*, "The Tynode: A new vacuum electron multiplier," *Nuclear Instruments and Methods in Physics Research Section A: Accelerators, Spectrometers, Detectors and Associated Equipment*, vol. 847, pp. 148–161, 3 2017.

[3] T. Hakamata, Ed., *Photomultiplier tubes*, 3rd ed. Hamamatsu Photonics K.K., 2007.

[4] H. Bruining, *Physics and Applications of Secondary Electron Emission*, 1st ed. McGraw-Hill Book Company, 1954.

[5] S. X. Tao, H. W. Chan, and H. van der Graaf, "Secondary Electron Emission Materials for Transmission Dynodes in Novel Photomultipliers: A Review," *Materials*, vol. 9, p. 1017, 12 2016.

[6] M. Hagino, S. Yoshizaki, M. Kinoshita, and R. Nishida, *Caesium Activated CsI Transmission-type Secondary Emission Dynode*, 1972, pp. 469–482.

[7] V. Prodanović, H. W. Chan, H. van der Graaf, and P. M. Sarro, "Ultra-thin alumina and silicon nitride MEMS fabricated membranes for the electron multiplication," *Nanotechnology*, vol. 29, p. 155703, 4 2018.

[8] X. Llopart, R. Ballabriga, M. Campbell, L. Tlustos, and W. Wong, "Timepix, a 65k programmable pixel readout chip for arrival time, energy and/or photon counting measurements," *Nuclear Instruments and Methods in Physics Research Section A: Accelerators, Spectrometers, Detectors and Associated Equipment*, vol. 581, pp. 485–494, 10 2007.

[9] H. Chan, V. Prodanovć, A. Theulings, C. Hagen, P. Sarro, and H. Graaf, "Secondary electron emission from multi-layered TiN/Al_2O_3 transmission dynodes," *Journal of Instrumentation*, vol. 16, p. P07024, 7 2021.

[10] V. Prodanović, "Ultra-thin MEMS fabricated tynodes for electron multiplication," Ph.D. dissertation, EEMCS, TU Delft, The Netherlands, 2019.

[11] K. Davami, L. Zhao, E. Lu, J. Cortes, C. Lin, D. E. Lilley *et al.*, "Ultralight shape-recovering plate mechanical metamaterials," *Nature Communications*, vol. 6, p. 10019, 12 2015.

[12] T. van der Reep, B. Looman, H. Chan, C. Hagen, and H. van der Graaf, "Measurement of the transmission secondary electron yield of nanometer-thick films in a prototype Timed Photon Counter," *Journal of Instrumentation*, vol. 15, pp. P10 022–P10 022, 10 2020.

[13] H.-J. Fitting, "Six laws of low-energy electron scattering in solids," *Journal of Electron Spectroscopy and Related Phenomena*, vol. 136, pp. 265–272, 6 2004.

[14] V. Prodanović, H. W. Chan, A. U. Mane, J. W. Elam, M. M. Minjauw, C. Detavernier *et al.*, "Effect of thermal annealing and chemical treatments on secondary electron emission properties of atomic layer deposited MgO," *Journal of Vacuum Science & Technology A: Vacuum, Surfaces, and Films*, vol. 36, p. 06A102, 11 2018.

[15] V. Prodanović, H. W. Chan, A. U. Mane, J. W. Elam, H. van der Graaf, and P. M. Sarro, "Ultra-thin ALD MgO membranes as MEMS transmission dynodes in a timed photon counter." presented at the IEEE 30th Intern. Conf. on Micro Electro Mechanical Systems (MEMS), Las Vegas, US, jan. 2017, pp. 740–743.

[16] H. Chan, V. Prodanović, A. Theulings, S. Tao, J. Smedley, C. Hagen *et al.*, "The construction and characterization of MgO transmission dynodes," *Journal of Instrumentation*, vol. 18, p. P06028, 6 2023.

APPENDIX C: SECONDARY ELECTRON YIELD MAP

A SEM image is constructed by measuring the SEE from a specimen, while an electron beam is scanned over its surface. The speed of a scan is determined by the dwell time, the time the electron beam irradiates a surface area corresponding with a pixel in a SEM image. The line time is the time to acquire one row of the image, which is the number of pixels in the row + additional time to reposition the beam onto the front of the next row. The frame time is the time to acquire the entire image. The resolution is the number of pixels in a row times the number of pixels in a column.

The TEY as a function of the coordinate of a SEM image can be obtained by measuring the transmission current during image acquisition. The background current is measured before the start, while the electron beam is blanked. Image acquisition starts, while the sample, grid and collector currents are measured simultaneously. After acquisition is done, the electron beam is blanked again. The background current is measured afterwards once more. The SEM settings for the measurement are: dwell time = 1 ms, Resolution = 512 x 442, linetime = 560 ms, frametime = 4.2 min.

The yield map reconstruction is performed with the same principle as image reconstruction in a SEM. The current is registered as a function of time. The background current is determined by the first and lasts few seconds. A measurement point as registered by the Keithley source meter can be acquired with a maximum rate of $333\,s^{-1}$ or 3.3 ms per data point. As such, each line only has 163 data points and needs to be stretched/extended into 3.3 pixels. The data points of 'missing' pixels are calculated by taking the average of two neighboring data points. After reconstructing the lines, they are cut into 540 ms sections and rearranged in a 2D matrix. Each line is then matched to the corresponding line in the SEM image.

The difficulty lies in removing artifacts that can arise due to timing delay. There can be a delay in either the SEM or the Keithley in which an extra pause is registered. The image is then distorted. These glitches can be removed manually.

ADDENDUM: CRITICAL STEPS OF THE FABRICATION PROCESS

In section 4.5.1, two critical steps/parts of the fabrication process were briefly discussed. This addendum[1] elaborates on these steps and gives recommendations on how to improve them. Optical microscope images have been included, which can be used to identify these critical steps in the fabrication process. In figure 4.16, a flow chart of the fabrication process is given.

The first critical part of the process is the removal of silicon from the backside of the wafer. First, a fast DRIE recipe was used to etch silicon from the backside as part of the release process (figure 4.16k). The optimal etch time was found by increasing the total etch time incrementally. The backside of the wafer was inspected after each increment under an optical microscope. In figure 4.17a, the first 'breakthrough' of DRIE is shown at which

[1] This addendum has not been published with the journal article, but is an addendum to this chapter.

the ribs of the patterns became visible. The next step was the removal of the protective PECVD oxide on the front side (figure 4.16l). This step was added to the fabrication process after a few unsuccessful release attempts. The PECVD oxide layer was identified as a possible cause for ruptures, since PECVD oxide deposition is non-conformal. This layer did not have the same metamaterial structure that the other remaining layers have. When the remaining silicon was removed, the PECVD oxide layer was the main contributor to the stress in the membrane. Therefore, it was opted to remove it at this stage. Last, a slower DRIE recipe was used to remove the remaining silicon (figure 4.16m). In figure 4.17b, the thermal oxide, which acted as a landing layer, became visible. The gradient in the color of the oxide is due to the DRIE process, which also etches oxide but at a much slower rate. In this case, the center of the cavity was etched for a longer duration, which caused the gradient.

An improvement on the fabrication process would be the replacement of PECVD oxide with LPCVD oxide. The latter is a conformal deposition, which will conform to the metamaterial structure and provide support instead of causing stress. However, the effect of the high temperature of the process on the $Al_2O_3/TiN/Al_2O_3$ film is unknown. The stress within the film can change as well as its SEE properties, although the RSEY of an Al_2O_3 film was shown to improve after thermal treatments [14]. It is thus worthwhile to investigate the use of LPCVD oxide as a replacement.

The second critical part of the process is the final release of the $Al_2O_3/TiN/Al_2O_3$ film by removing the thermal oxide. The etch rate of thermal oxide and PECVD oxide was different. The thermal oxide required more etching cycles to be fully removed, as the recipe was run 3 to 4 times (each consisting of 4 etching cycles for a duration of 10 min). In figure 4.18, a metamaterial membrane is shown after 4, 8, 12 and 16 cycles, respectively. Thermal oxide has a color gradient, whereas the $Al_2O_3/TiN/Al_2O_3$ film has a blueish grey color. It is thus possible to confirm when a metamaterial membrane is fully released using an optical microscope.

In figure 4.19 and 4.20, optical microscope images of fully released metamaterial membranes are shown with the honeycomb and octagonal patterns. In these images, the same residues are visible on the surfaces as were observed in the SEM images (figure 4.8). When the number of etching cycles was increased, the residues did not seem to be affected by it. At this stage of the process, there were limited options to remove the residues as the released membranes were fragile. The metamaterial membranes are relatively strong, but can be damaged if they are subjected to another (plasma) etch. In addition, the extra transport and handling steps of the membranes increase the risks of fracture.

There are two common mistakes that need to be avoided when handling the released samples. First, when the dies are accidentally dropped on a flat surface, the air pressure within the cavity can cause the metamaterial membrane to bulge or even break. Second, if the lid of the storage box is close to the surface of the die, the die can stick to the plastic lid due to electrostatic forces. It is almost impossible to remove the die from the lid once it gets stuck without breaking the membrane. A trick is to place the dies on an uneven surface, such as a piece of cleanroom towel, which prevents a sudden air pressure change when dropped. In addition, it makes it easier to lift the dies out of the box without damaging them.

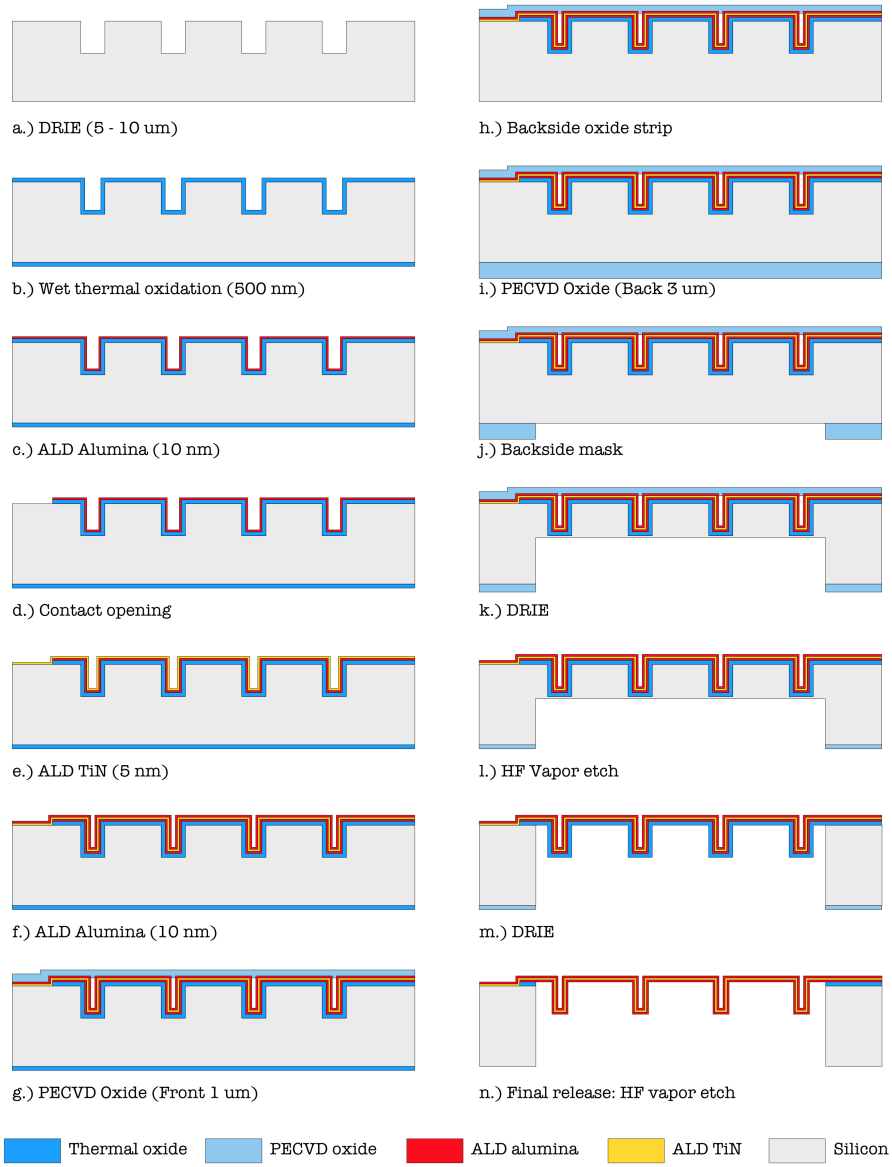

Figure 4.16: Flow chart.

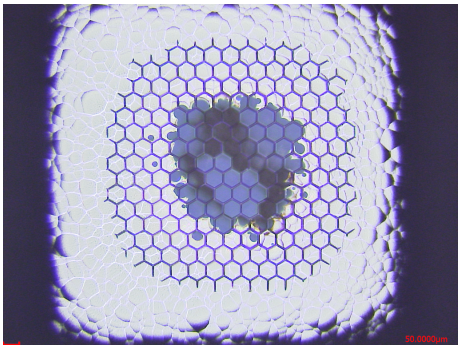

(a) Revealing the ribs of the honeycomb pattern.

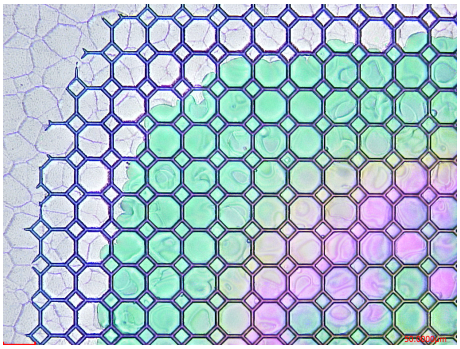

(b) Landing on oxide

Figure 4.17: DRIE

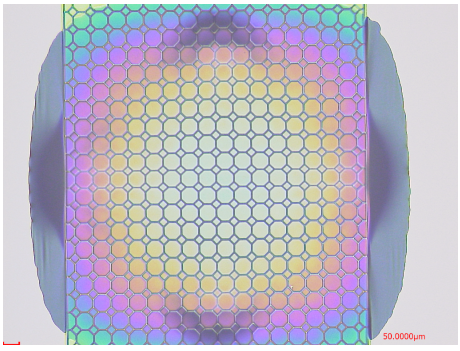

(a) After 4 cycles

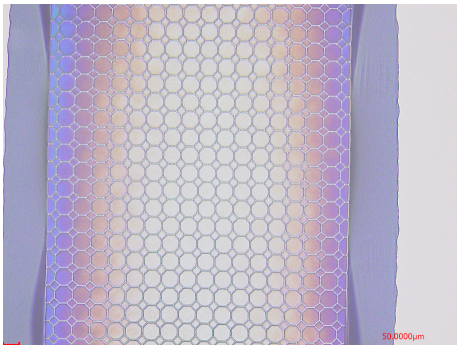

(b) After 8 cycles

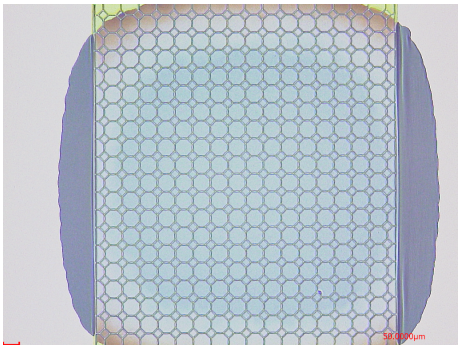

(c) After 12 cycles

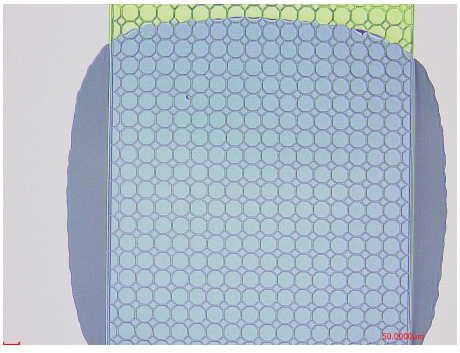

(d) After 16 cycles

Figure 4.18: A metamaterial membrane after 4, 8, 12 and 16 cycles of HF etching. The duration of one etching cycle is 10 min. The metamaterial membrane in these images is designed to be suspended from two sides (top and bottom in these images). However, the left and right side of the metamaterial membrane have not been 'cut', so there is still Al_2O_3/TiN/Al_2O_3 film present and the membrane is still suspended on all sides.

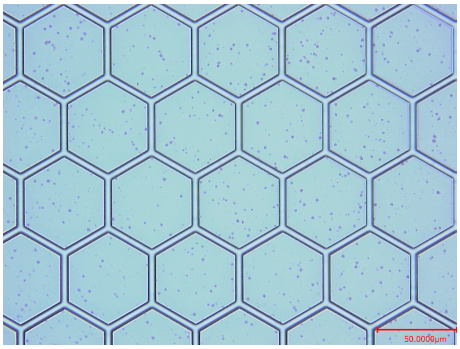

(a)

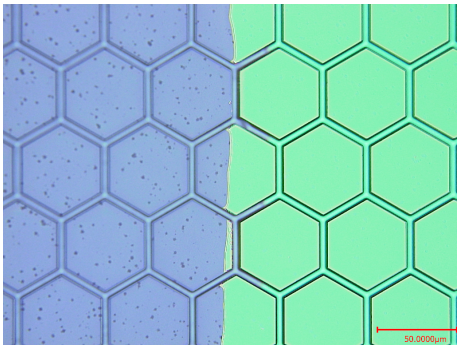

(b)

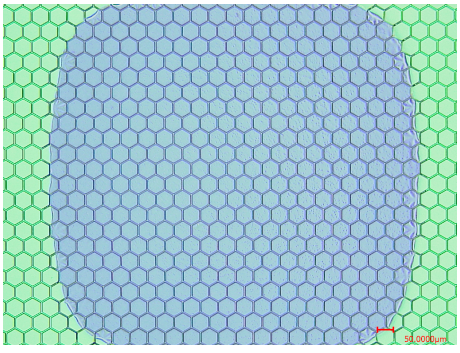

(c)

Figure 4.19: A fully released membrane with a honeycomb pattern.

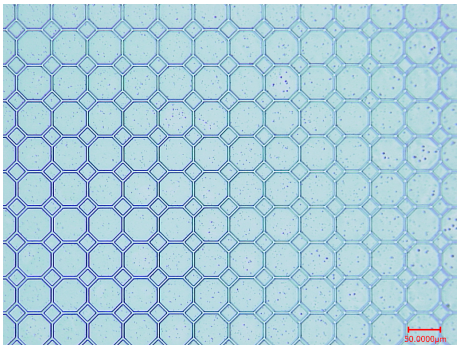

(a)

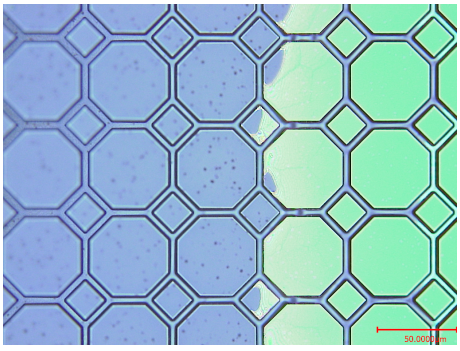

(b)

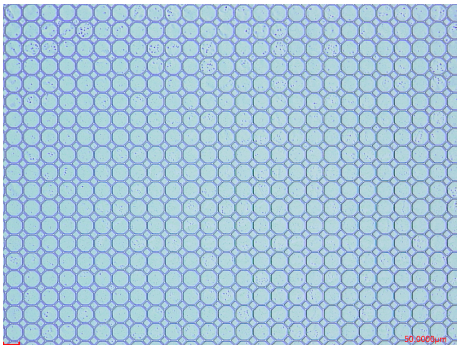

(c)

Figure 4.20: A fully released membrane with an octagonal pattern.

5

CONCLUSION

The main objective of the MEMBrane project is to develop a novel electron multiplier with, as its key components, the transmission dynodes (tynodes). In the introduction, four key challenges were identified in the development of Timed Photon Counter (TiPC). This work focuses on two of them: Micro-ElectroMechanical System (MEMS) fabrication and transmission electron emission measurements of which the main conclusions will be summarized in section 5.1 and 5.2, respectively. In chapter 6, an outlook and recommendations on further developments will be given.

5.1. MEMS FABRICATION

In MEMS fabrication, the number of materials that are cleanroom compatible is limited. Introducing new materials is an option, but precaution would need to be taken to avoid cross contamination. Also, the recipes for new materials need to be optimized and characterized, which can be time consuming. As such, in this work the focus is to explore materials and deposition techniques that are readily available in MEMS fabrication. Atomic Layer Deposition (ALD) is the most suitable and versatile technique to deposit ultra-thin films.

In this work, ALD aluminum oxide (Al_2O_3) and ALD magnesium oxide (MgO) have been successfully implemented as the secondary electron emission (SEE) layer in ultra-thin membranes. Both materials are dielectrics, therefore an additional conductive layer was added to provide lateral conductivity. Titanium nitride (TiN) was deposited by sputtering for the bi-layer membranes at the end of the fabrication process, while for the tri-layer membranes, the TiN layer was sputtered in an earlier stage. For the latter, the TiN layer is encapsulated between two SEE layers. This improves the reliability of the fabrication process, i.e. the TiN layer provides sufficient conductivity to prevent charge-up effects. A similar tri-layered film is used to form a corrugated membrane. In this case, the TiN layer is deposited by ALD as well, since a conformal deposition is required to cover the 3D features on the silicon mold.

Three different types of tynodes have been presented: single-membrane, square-array and corrugated membrane. The single-membrane is designed for the character-

ization of the (transmission) SEE properties of membranes with different thicknesses. These single-membranes are also used to find the limit on the physical dimensions of ultra-thin membranes. Herein, the film thickness is a production parameter. The square-array design is developed to be compatible with TimePix pixel chips. The circular windows in the array have a square pitch of 55 µm, which matches the pixel pad pitch. For these tynodes, good alignment of the stack and the pixel chip is necessary.

The corrugated metamaterial membrane is designed to enlarge the active surface. A corrugated membrane is mechanically stronger in comparison with a flat membrane, but is continuously ultra-thin throughout its structure. The membrane has an active surface of nearly 100%, i.e. electron multiplication occurs regardless of the point of impact. The largest membrane has a surface of about 16 mm^2, which can cover 72 × 72 pixels of a TimePix chip. The advantage of these tynodes over the square-array tynodes is that focusing and alignment are less stringent in comparison. As such, the collection efficiency should be better. In addition, the octagonal cups of the corrugated membrane have a focusing effect as well. They have the same square pitch of 55 µm as the square-array tynode and a TimePix chip. They will perform exceptionally well as the first tynode due to its large active surface and focusing. If we can improve its (total) transmission electron yield (TEY), i.e., higher yield at a lower primary electron (PE) energy, then they can be used in the entire stack.

5.2. TRANSMISSION SECONDARY ELECTRON EMISSION

A method have been developed to investigate the transmission (secondary) electron emission properties of tynodes within a scanning electron microscope (SEM). The collector-based method utilizes the imaging capabilities of the SEM to inspect and locate the ultra-thin membranes on the tynode. During a measurement, the electron beam only targets the active surface, which prevents charge-up effects on the surrounding support structure. The electron dose can be controlled by scanning the electron beam over the surface rather than focusing on one point, which prevents charge-up effects within the ultra-thin membrane and/or the build-up of contamination. It is worth noting, that this method only works for thin-film-on-silicon samples and ultra-thin tynodes with a conductive layer. On thicker dielectric films and dielectric membranes, charge-up effects were observed, which impeded SEE.

A second method is developed to inspect multiple membranes simultaneously in a square-array. It would have been cumbersome to inspect and measure the TEY of each membrane individually. By measuring the sample and transmission currents during an image acquisition, a (total) reflection electron yield (REY) and TEY map are reconstructed that both correspond with the SEM image. The REY and TEY of individual membranes in a part of the array have been measured and their averages have been determined to compare their effectiveness as a tynode. The scan method has also been used on the corrugated membranes to create a TEY map on which the many features of the corrugated membrane is present.

The film thickness was shown to play an important role in transmission SEE. The onset of transmission SEE, the maximum TEY and the TEY curve as a function of PE energy depend on the film thickness. The highest maximum TEY of an Al_2O_3/TiN/Al_2O_3 single-membrane was 3.1(1.55 keV), which has layer thicknesses of 5/2.5/5 nm, respec-

tively. The film thickness is close to the optimal film thickness of 8 nm predicted by Monte-Carlo simulations. However, a direct comparison cannot be made unless the difference in stopping power of Al_2O_3 and TiN is addressed and corrected by calculating an equivalent film thickness for TiN. In this case, the multi-layered membrane has an equivalent film thickness of 13.8 nm if it only consists of Al_2O_3. When the film thickness was increased in the simulation, the maximum TEY was lower and a higher PE energy was needed to achieve it. The same trend is observed in the results of this work. There is thus still room for improvement by reducing the film thickness.

It has been demonstrated that electron multiplication occurs on all the features of a corrugated membrane when it is irradiated by an electron beam, i.e. a TEY of 1 or higher is observed on the entire surface. For this, the surface scan method is used to construct a TEY map. The averaged TEY over a large surface of the corrugated membrane is 2.15(3.15 keV), which is lower compared to a flat tri-layered membrane with similar composition and thicknesses. The latter has a TEY of 2.7(2.75 keV). The shift in PE energy, at which the maximum TEY is measured, suggests that the corrugated membrane is thicker.

A TEY of 4 or higher was shown to be achievable. The TEY of individual TiN/MgO membranes in a square array was measured using the surface scan method. An averaged TEY of 4.6 ± 0.2(1.35 keV) was measured for a TiN/MgO tynode with membrane thicknesses of 2/5 nm, respectively. In this case, a planar collector assembly is used to investigate the effect of a strong electric field near the emission surface. The electric field is in the same order of magnitude as the electric field between tynodes in a stack in TiPC. When the bias voltage increases from -50 V to -100 V, the averaged TEY improves from 4.6 ± 0.2 to 5.0 ± 0.3. An outlier of 5.5 has been measured on one of the window. If we limit to a PE energy of 1 keV, the MgO square-array still has an averaged TEY of 3.7. The variance in TEY between the membranes in the array might be attributed to the fabrication process in which the TiN layer is sputtered near the end of the process. The topographical features on the tynode affect the deposition uniformity, which leads to a variation in membrane thicknesses.

Major steps have been taken to achieve the main objective: the development of TiPC. It is feasible to fabricate ultra-thin membranes by means of MEMS technology. In addition, an important tool was developed to inspect and measure the electron emission properties of these membranes. In the next section, recommendations will be given on how to further, improve the tynode design, increase the TEY of the tynodes and proceed with building a prototype TiPC with a tynode stack.

6

OUTLOOK & RECOMMENDATIONS

In this chapter, we will first give recommendations on how to improve the design of the corrugated membranes. Then we will give recommendations on how to improve the (total) transmission electron yield (TEY) of ultra-thin membranes in general. Lastly, we will give an outlook on how to assemble a prototype Timed Photon Counter (TiPC).

6.1. IMPROVING THE CORRUGATED METAMATERIAL TYNODES

- **ALD magnesium oxide (MgO) as secondary electron emission (SEE) material.** ALD MgO should be applied as the SEE layer for the corrugated membrane as well, since MgO has a better TEY as is demonstrated. The fabrication process would require some small adaptations; the ALD Al_2O_3 steps can be replaced with ALD MgO.

- **Optimizing the film thickness.** For the corrugated membranes, layer thicknesses of 10/5/15 nm was used for Al_2O_3/titanium nitride (TiN)/Al_2O_3, respectively, which is suboptimal from a TEY perspective. Reducing the film thickness can improve its performance as a transmission dynode (tynode), i.e. a higher TEY at lower primary electron (PE) energies. The overall film thickness should be reduced to the optimal thicknesses that we have found for ALD Al_2O_3 or ALD MgO. Although, reducing the film thickness would reduce the mechanical strength of the corrugated membrane. As a concession, the size of the membrane should be reduced. A coverage of 32×32 pixels for a corrugated membrane with a reduced thickness should be possible. Using support beams, multiple corrugated membranes can be placed next to each other to cover the entire surface of a TimePix chip. However, the support beams would introduce some inactive surfaces on a tynode.

- **Improving the design** The design of the corrugated membrane can be altered, so that the collection efficiency of a tynode stack increases. For instance, the ribs can be made more rounded, which can improve focusing. A 'stray' (photo)electron that strikes the walls of a rib with a U- or V-shape will emit its transmission secondary electrons (TSEs) towards the center of the octagonal cup on the tynode below.

- **Increasing the surface coverage of tynodes.** A TimePix-1 chip has 256 × 256 pixels and a surface area of about 1.96 cm^2. The largest square-array that has been manufactured has a size of 128 × 128 [1], which only covers a quarter of a TimePix-1 chip. The current iteration, TimePix-4, has 448 × 512 pixels and a surface of about 6.94 cm^2. To cover such a large surface, it is inevitable to include support beams, which are relatively thick in the order of the substrate thickness of about 300 µm. The square-arrays can then be suspended to the support beams in a big raster. For instance, the square-arrays could cover 62 × 62 pixels, sacrificing a row of 4 pixels on each side to accommodate the support beams in the design. Similarly, the corrugated membranes can be suspended in such a raster with support beams.

6.2. IMPROVING THE TRANSMISSION ELECTRON YIELD

- **Chemical treatment.** Chemical treatment of the SEE film might improve the TEY of tynodes. The effect of chemicals on reflection SEE was studied using thin-film-on-silicon samples [2]. These samples were subjected to the same fabrication processes as in tynode fabrication. ALD MgO was deposited on a silicon wafer and diced into smaller dies. Some of the dies were covered with an oxide layer to mimic the protection layer that is used in the fabrication process of tynodes. Bare and covered thin-film samples were then exposed to hydrofluoric (HF) vapor. In both cases, the (total) reflection electron yield (REY) improved in comparison with an as-deposited thin-film sample. The film material might have been altered as X-ray photoelectron spectroscopy (XPS) data showed some fluorine content; Oxygen might have been substituted for fluorine resulting in a MgOF compound. It is worthwhile to investigate this effect more extensively; the exposure to HF vapor is unavoidable but the duration can be controlled to optimize its TEY.

- **Thermal treatment.** Applying a thermal treatment to the tynodes might improve their TEY. The effect of thermal treatments on reflection SEE was studied using thin-film-on-silicon samples [2]. The REY of these samples improved after a thermal treatment. The surface morphology changed as well, which is an indication that the material properties, such as crystallinity, have changed after exposure to heat. A thermal treatment might be beneficial to the TEY of the ultra-thin membrane, but the structural properties might be affected as well. Applying a thermal treatment during the fabrication process or as a post-process might result in thermal stresses that can break the membranes. A bake-out is also a thermal treatment, but at a relatively lower temperature. Bake-outs are more commonly used in ultra-high vacuum (UHV) systems to remove hydrocarbons. The effect of a bake-out on the TEY of ultra-thin films/membranes in UHV needs to be investigated as well.

- **Surface termination**. Surface termination is a more complex procedure, since a UHV setup is required in which surface termination with hydrogen (H) or cesium (Cs) can be applied in-situ. However, the effect of surface termination is profound in the case of diamond. Yater [3] reported a REY of 3, 60 and 132 for a bare, H-terminated and Cs-terminated diamond, respectively in the PE energy range of 0 - 2900 eV. This is attributed to the negative electron affinity (NEA) on the surface.

Density Functional Theory (DFT) calculations have shown that such terminations on silicon nitride also result in a NEA surface. The same might apply to Al_2O_3 and MgO and DFT calculations can provide the answer.

- **Alternative materials.** Other cleanroom materials have been investigated, such as polycrystalline silicon, silicon nitride, silicon carbide and aluminum nitride [1]. These material have a lower REY compared to ALD MgO and are not expected to perform better as a tynode.

- **Diamond.** Diamond can have an extraordinary high REY due to its wide band gap, which allows internal secondary electrons (SEs) to travel a great distance and escape due to a NEA on its surface [3]. An ultra-nanocrystalline diamond (UNCD) single-membrane with a thickness of 130 nm have been fabricated [1]. The REY and TEY are 3.2 and 1.8(4.95 keV), respectively. The REY is similar to the reported yield of bare diamond [3]. However, it is not possible to apply a surface termination in our setup. The question remains whether a surface termination would improve the TEY in a similar fashion as in the case for REY and will an early onset of transmission SEE at low PE energy be observed. In the case of a single-crystal diamond, the escape depth of internal SEs is in the order of a few µm. If a single-crystal diamond membrane with a NEA can be manufactured, then a prediction would be that internal SEs generated on one side of the membrane can traverse the entirety of the film and escape from the other side. In our case, UNCD have many grain boundary that might prevent this from happening. The growth of ultra-thin diamond is much more complicated in comparison with ALD of Al_2O_3 or MgO as diamond needs seeds as nucleation sites for growth. Another question is whether reducing the film thickness of UNCD to a few tens of nm, such that the required PE energy shifts to a lower value, would results in a better performance in comparison with ALD MgO. For ultra-thin films, the transport characteristics of internal SEs play a lesser role.
  However, single-crystal diamond would be a perfect candidate as an electron emission membrane. A (thick) membrane of diamond can be used to detect minimum ionizing particles (MIPs). A MIP that penetrates such a membrane can excite internal SEs along its track. A large interaction volume is required to generate sufficient internal SEs. In most materials, the internal SEs generated deep within the membrane are reabsorbed and only internal SEs near the exit surface have a chance to escape. In single-crystal diamond with a NEA, all internal SEs would have a chance to escape.

6.3. TIPC PROTOTYPE

The tynode test setup (Tytest) was built to investigate the performance of a TimePix-1 chip combined with a tynode in an UHV environment [4–6]. The setup consists of an electron gun as the source for PEs, a tynode(stack) holder and a TimePix-1 chip as readout in a vacuum enclosure. On the enclosure, there are High Voltage (HV) feed-throughs that can be used to apply an incrementally larger bias voltage on each tynode in a stack. So far, Tytest has been used to determine the TEY of a corrugated membrane, which was in agreement with the results in chapter 4. Here recommendations will be given on how

to upgrade this setup, so that it can accommodate a tynode stack for electron multiplication.

- **Retrofitting the setup with a new electron source.** The current electron gun in the setup has an operation range of 1 eV to 2 keV, which is sufficient for testing a single tynode. However, in a stack with multiple tynodes, the voltage would be decreased step-wisely with 1 kV. The TimePix chip is kept at ground potential, so the first tynode would be at −6 kV in a stack of 5. To test a tynode stack, the range of operation should be in the 0.1 to 10 keV-range to provide PEs with sufficient energy. An alternative is to use a photocathode that is negatively biased with respect to the first tynode in the stack. An external laser can then be used to generate photoelectrons. The advantage of using a laser is that it can generate ultrafast test-pulses, which allow us to investigate the timing response of a combined tynode stack and a TimePix chip.

- **Stacking and aligning tynodes.** The best performing tynodes are the square-arrays with ALD MgO membranes. The individual circular membranes need to be aligned in neat columns. A shift in the position of the tynodes can reduce the collection efficiency of TiPC. To achieve a good alignment, alignment grooves have been added to both side of the silicon substrate [1]. The placement of the grooves is determined by the lithography process and is very accurate. The tynodes are stacked by placing glass rods as spacers inside the grooves, which self-aligns the grooves. The glass rods also serve as an electrical insulator. Furthermore, dome-shaped membranes have been proposed, which would have a focusing effect on the TSEs, so that they remain in neat columns above the pixel pads. The alignment of the corrugated metamaterial tynodes is less stringent and the proposed measures are not needed for these type of tynodes. However, their TEY needs to be improved first before they can be used.

- **Investigating the behaviour of transmitted electrons in a tynode stack.** Transmitted electrons can cause (unwanted) electron emission within a tynode stack. The behavior of fast electrons in a tynode stack can be simulated with a computer model. In chapter 2, it was shown in figure 2.13 that when the maximum TSEY was achieved, the transmitted fraction is 0.4-0.5, i.e. 40-50% of the PEs are able to penetrate the ultra-thin membranes. Transmitted electrons carry an energy of 30 to 40% of their initial PE energy [7].

- **HV connections to the tynodes.** HV connections to the tynodes are required in a stack. A practical challenge is to attach HV connectors to the individual tynodes in the stack without triggering electrical arcing. A solution is to dice the tynodes in rectangles with an off-centered square-array. The extra silicon would stick out from the stack. By placing each tynode at an angle of 90 degrees, the connection points for each tynode would be on a different side. This would reduce the chance of arcing.

- **Micro-HV supply** TiPC requires a HV supply that can reach up to 6000 V, but with low power/current requirements. The goal is to integrate the HV supply in the

same package as TiPC. For this, plans have been made to downscale a Cockcroft-Walton (CW) HV generator[8, 9] into a portable component. A CW generator converts a low-voltage alternating current (AC) into a HV direct current (DC) by only using capacitors and diodes. A ladder of capacitors are charged alternately by an AC. The diode configuration allows each capacitor on the ladder to reach a voltage that is a multiple of the input voltage. If a wall outlet with 220 V at 50 Hz is used, then TiPC would require a CW multiplier with 28 capacitors. Recently, a novel hybrid Cockcroft-Walton/Dickson multiplier has been proposed [10]. In a tabletop-sized prototype, a voltage of 3.9 kV was reached in 113 s using a 100 V at 60 Hz input. The challenge is to scale down the size of this or a similar multiplier. For this, MEMS technology might provide solutions.

REFERENCES

[1] V. Prodanović, "Ultra-thin MEMS fabricated tynodes for electron multiplication," Ph.D. dissertation, EEMCS, TU Delft, The Netherlands, 2019.

[2] V. Prodanović, H. W. Chan, A. U. Mane, J. W. Elam, M. M. Minjauw, C. Detavernier *et al.*, "Effect of thermal annealing and chemical treatments on secondary electron emission properties of atomic layer deposited MgO," *Journal of Vacuum Science & Technology A: Vacuum, Surfaces, and Films*, vol. 36, p. 06A102, 11 2018.

[3] J. E. Yater, "Secondary electron emission and vacuum electronics," *Journal of Applied Physics*, vol. 133, 2 2023.

[4] W. de Landgraaf, "Development of the TyTest setup - as system to probe to probe the transmission secondary electron yield of ultra-thin membranes," M.S. thesis, Applied Sciences, TU Delft, the Netherlands, 2017.

[5] B. Looman, "Measuring the transmission yield of ultra-thin membranes," M.S. thesis, Applied Sciences, TU Delft, the Netherlands, 2020.

[6] T. van der Reep, B. Looman, H. Chan, C. Hagen, and H. van der Graaf, "Measurement of the transmission secondary electron yield of nanometer-thick films in a prototype Timed Photon Counter," *Journal of Instrumentation*, vol. 15, pp. P10 022–P10 022, 10 2020.

[7] H.-J. Fitting, "Six laws of low-energy electron scattering in solids," *Journal of Electron Spectroscopy and Related Phenomena*, vol. 136, pp. 265–272, 6 2004.

[8] J. D. Cockcroft, "Experiments with high velocity positive ions.—(i) further developments in the method of obtaining high velocity positive ions," *Proceedings of the Royal Society of London. Series A, Containing Papers of a Mathematical and Physical Character*, vol. 136, pp. 619–630, 6 1932.

[9] J. D. Cockcroft, "Experiments with high velocity positive ions. ii. -the disintegration of elements by high velocity protons," *Proceedings of the Royal Society of London. Series A, Containing Papers of a Mathematical and Physical Character*, vol. 137, pp. 229–242, 7 1932.

[10] K. Eguchi, D. Nakashima, T. Ishibashi, and F. Asadi, "A high voltage multiplier using stacked hybrid cockcroft– walton/dickson multipliers," *Journal of Physics: Conference Series*, vol. 2022, p. 012019, 9 2021.

ACKNOWLEDGEMENTS

Every PhD candidate will reflect differently on their journey. For some, it would have felt like climbing a mountain, hiking through the wilderness or swimming in the ocean. For me, it felt like *running a marathon*. A marathon is a race with a distance of 42.195 km in which thousands of runners participate; each running at their own pace and with their own goal in mind. The goal is not to beat each other's time, but rather to best your own personal record or, for first-timers, to make it to the finish line. It requires months of training in which you slowly ramp up your weekly mileage; the furthest distance in your training will be about 30 km. Despite the time and effort you put into your preparation, race day will be unpredictable. The race beyond the 30K mark will be uncharted territory for first-timers. At this stage, fatigue and doubt will creep in. Did I run too fast? Should I slow down? Will I make it to the finish line? Whose brilliant idea was it to run a marathon? It will be as much a physical as a mental challenge at this point. Though, it is in these moments that you will dive within and discover strength and perseverance. In my PhD journey there were similar moments of struggle and self-doubt, but I am glad to have made it to the finish line. I would not have been able to do so without the help of my coaches, fellow runners and the people cheering me on along the way.

My deepest gratitude to my running coaches: Prof. Harry van der Graaf, Prof. Lina Sarro and Dr. Kees Hagen. I am grateful for your support, patience and guidance. Harry and Lina encouraged me to run my metaphorical marathon after finishing my MSc. project. During this project, I was introduced into the world of particle detectors and MEMS technology in which they have taught me how to apply my learned skills, knowledge and creativity. After graduation, I was offered to continue on the project as a PhD student. I am grateful for the opportunity in which I could further grow as a researcher. I would like to thank Harry for his trust in me. The worst feeling for a runner to slow down or stop in a race. There were times that I could not take another step, but you always kept the believe that I could make it to the finish line. I would also like to thank Kees who helped me to get back on track when I struggled. You reminded me to take one step at a time and to focus on improving my technique. My deep appreciation for the time and effort you put into reading, correcting and improving my papers and thesis. Small improvements save energy, which will cumulate in the long run (pun intended). I am grateful for the great advices of my coaches that I have received in these years. If I had adapted them from the very beginning, my marathon would have been so much easier.

I would also like to express my gratitude to Prof. Kees Wapenaar, Prof. Bernd Rieger, Prof. Tristan du Pree, Prof. Klaus Desch and Ir. Gert Nutzel for being part of the doctoral defense committee. Thank you for your time and effort in the assessment of my dissertation.

I would also like to show my sincere appreciation for all the great runners that I had the pleasure to run with. After the hectic start of a marathon, you will be surrounded by groups of runners running at about the same pace as you. Despite the personal pursuit of each runner, running in a group can be beneficial; they help you to maintain a steady pace and provide shelter from the wind. More importantly, you will meet and get to know many great runners, which makes the journey more pleasant and the endeavor more bearable. As a PhD student, I was welcomed into different groups who have helped me tremendously through these years.

I am grateful to all members of the MEMBrane group. It was my pleasure to work with Annemarie, Bram, Conny, Daan, John Smedley, John Sinnsheimer, Shuxia, Tom, Thijs and Wouter. Violeta, I had a great time working with you on the project. Thank you for being a good friend with whom I could embark on adventures to escape work. Hassan, I appreciate the hard work you put into the measurement setup. My sincere gratitude to the charged particle optics group at ImPhys for hosting our group and supporting us with the experiments with the scanning electron microscope. Carel, thank you for teaching me how to operate the SEM and your help with my measurement setup. Also many thanks to Han, Joost, Marijke, Sangeetha and Gaudhaman for their help.

I would like to express my gratitude to the MEMS group at the ECTM department. I think MEMS is one of the research fields where you need to apply an equal amount of skills, knowledge and creativity. This is reflected in the work showcased by the many posters in the hallway; I was marveled by the ingenious flow charts and designs. I have not spend nearly as much time in the cleanroom as I would have liked to, but I always felt welcome whenever I was around. I would like to thank everyone at the ECTM department with whom I had the pleasure to work alongside in the cleanroom: Fabio, Amir, Elina, Thomas, Gianpaolo, Bruno, Sten, Maryam, Giuseppe, Rene, Miki, Pengfei, Thu Hang, Niko, William, Xueming, Juan, Marta, Joost, Milica, Shinnosuke, Jian, Dong, Hande and many others. Cinzia, thank you for organizing the unofficial program of the MEMS conference in Las Vegas. Aleksandar, I had a fun time on the roadtrip; it was great to share the amazing sceneries with you. I will get my driver's license soon, so hopefully one day I can return the favor of being the driver. A big thanks to Marian, who helped me to finding my way around in the ECTM department when I first started.

My sincere gratitude to everyone working at EKL. Without your help, I wouldn't be able to manufacture the tynodes. I would like to thank Cassan and Sylvana for their processing courses. Thanks to you, I have found confidence to run processes on my own. I am grateful to Henk and Gregory with whom I could discuss my flow charts and designs. Many thanks to Mario, Wim, Hugo, Alex and others for their help with the equipment and trainings.

I am profoundly grateful to the detector R&D group at NIKHEF for their help, support and hospitality. A lot of thanks to Niels, Fred, Martin Fransen, Martin van Beuzekom, Rolf, Yevgen, Wilco, Joris, Panos, Matteo and others. Whenever I was in Amsterdam, I was always welcomed by you to join for coffee and lunch. I am thankful to Oscar van Petten for manufacturing parts of the measurement setup.

The last ingredient for a memorable marathon is the crowd; there will be people cheering, bands playing music, and people handing out fruit and drinks. Receiving high fives

from strangers will give you small speed boosts. However, seeing familiar faces along the course will truly lift your spirit. My gratitude to my friends and family who have supported me through all these years. Your support and encouragement were invaluable along the way.

I am blessed with my paranymphs: Astrid and Rosa. When I ran an actual marathon, they were standing along the course with signs to cheer me on: 'Hong, stay strong'. With newfound energy, I was able to get through the tough part of the race and finish the marathon. I have kept that sign on my wall as a daily motivator to keep running on my metaphorical marathon. Thank you for being there for me through the difficult times. I could always count on you whenever I needed someone to talk to. I wouldn't have regained my confidence without your help and I am honored to have you by my side on the day of my defense. Lots of love to you, Coen, Tim and Maura.

I would like to express my appreciation for my friends from high school and their lovely partners: David & Willemijn, Edward & Victoria, Eelke & Anne, Erik & Nicky, Guido & Marian and Wilbert & Charlotte. Thank you for all your support through these years; I know that you would have dragged me across the finish line if you could have. I wonder who has won the bet. I also cherish the friendships that I have formed in Delft: Chimin & Yuki, Stefano & Lioba and Bahman & Maria. Thank you for the hundreds of hours of playing settlers of Catan together. We have empirically proven that it is a skill-based game rather than a statistical one (despite the game mechanism of using two dices).

I would like to thank my many (former) roommates: Inge, Taco, Olmo, Sarah, Jasmin, Romy, Kimberley, Alex, Sam, Macy, Quincy and Beth. Thank you for being there for me, whether just for a small talk, fashion tips or discussing the meaning of life. Olmo, I really enjoyed the coffee breaks in the morning. I would also like to show some appreciation to my sport buddies. Sifrah, I had I had lots of fun running the vuurtorentrail with you. Mark, thanks for all the bouldering sessions.

Lastly, I am extremely grateful to my family who have always encouraged and supported me on my academic journey. They allowed me to finish my PhD at my own pace. My sincere thanks to my brother & Julie. I hope one day I can help and support Noah in his academic pursuit. I am truly thankful to my sister & Karlun. I am forever indebted to you, both literally ;-) and figuratively. I am eternally grateful to my mom and dad, who have worked so hard to provide for us and allowing us to pursuit our dreams and goals. I love you for all that you have done for us.

This work was supported by the ERC-Advanced Grant 2012 MEMBrane 320764.

CURRICULUM VITÆ

Hong Wah CHAN

24-10-1983	Born in Utrecht, the Netherlands.

EDUCATION

1997–2002	Pre-university education (Voorbereidend Wetenschappelijk Onderwijs) Niels Stensen College, Utrecht
2002–2011	Bachelor of Science in Applied Physics Delft University of Technology
2011–2014	Master of Science in Applied Physics Delft University of Technology
2024	PhD Delft University of Technology *Thesis:* The Realization & Characterization of Transmission Dynodes *Promotor:* prof. dr. P.M. Sarro *Promotor:* prof. dr. ir. H. van der Graaf *Promotor:* dr. C.W. Hagen

LIST OF PUBLICATIONS

10. **H. W. Chan**, V. Prodanović, A. Theulings, S. Tao, J. Smedley, C. Hagen, P. Sarro, and H. van der Graaf, *The construction and characterization of MgO transmission dynodes*, Journal of Instrumentation **18**, P06028 (2023).

9. **H. W. Chan**, V. Prodanović, A. Theulings, T. ten Bruggencate, C. Hagen, P. Sarro ,and H. van der Graaf, *Ultra-thin corrugated metamaterial film as large-area transmission dynode*, Journal of Instrumentation **17**, P09027 (2022).

8. **H. W. Chan**, V. Prodanović, A. Theulings, C. Hagen, P. Sarro, and H. van der Graaf, *Secondary electron emission from multi-layered TiN/Al_2O_3 transmission dynodes*, Journal of Instrumentation **16**, P07024 (2021).

7. T. van der Reep, B. Looman, **H. W. Chan**, C. Hagen, and H. van der Graaf, *Measurement of the transmission secondary electron yield of nanometer-thick films in a prototype Timed Photon Counter*, Journal of Instrumentation, **15** P1022 (2020).

6. V. Prodanović, **H. W. Chan**, A. U. Mane, J. W. Elam, M. M. Minjauw, C. Detavernier, H. van der Graaf, and P. M. Sarro, *Effect of thermal annealing and chemical treatments on secondary electron emission properties of atomic layer deposited MgO*, Journal of Vacuum Science & Technology, **36** p. 06A102 (2018).

5. V. Prodanović, **H. W. Chan**, H. van der Graaf, and P. M. Sarro, *Ultra-thin alumina and silicon nitride MEMS fabricated membranes for the electron multiplication*, Nanotechnology, **29** p.155703 (2018).

4. V. Prodanović, **H. W. Chan**, A. U. Mane, J. W. Elam, H. van der Graaf, and P. M. Sarro, *Ultra-thin ALD MgO membranes as MEMS transmission dynodes in a timed photon counter*, presented at the 30th IEEE International Conference on Micro Electro Mechanical Systems (MEMS), 740-743 (2017).

3. H. van der Graaf, H. Akhtar, N. Budko, **H. W. Chan**, C. W. Hagen, C. C. Hansson, G. Nützel, S. D. Pinto, V. Prodanović, B. Raftari, P. M. Sarro, J. Sinsheimer, J. Smedley, S. Tao, A. M. Theulings, and K. Vuik, *The tynode: A new vacuum electron multiplier*, Nuclear Instruments and Methods in Physics Research Section A: Accelerators, Spectrometers, Detectors and Associated Equipment **847**, pp 148-161 (2017).

2. S. Tao, **H. W. Chan**, and H. van der Graaf, *Secondary electron emission materials for transmission dynodes in novel photomultipliers: A review*, Materials **9**, p. 1017 (2016).

1. Y. Bilevych, S. Brunner, **H. W. Chan**, E. Charbon, H. van der Graaf, C. Hagen, G. Nützel, S. Pinto, V. Prodanović, D. Rotman, F. Santagata, P. Sarro, D. Schaart, J. Sinsheimer, J. Smedley, S. Tao, A. Theulings, *Potential applications of electron emission membranes in medicine*, Nuclear Instruments and Methods in Physics Research Section A: Accelerators, Spectrometers, Detectors and Associated Equipment **809** p. 171-174 (2016).